DEGREE PROJECT IN ENGINEERING PHYSICS,
SECOND CYCLE, 30 CREDITS
STOCKHOLM, SWEDEN 2018

Performance studies of Low-Gain Avalanche Diodes for the ATLAS High-Granularity Timing Detector

ANTEK SZADAJ

KTH ROYAL INSTITUTE OF TECHNOLOGY
SCHOOL OF ENGINEERING SCIENCES

Master Thesis in Physics

Performance studies of Low-Gain Avalanche Diodes for the ATLAS High-Granularity Timing Detector

Author:

Antek Szadaj

antek@kth.se

Department of Physics

KTH Royal Institute of Technology

Supervisor:

Christian Ohm

December 4, 2018

TRITA-SCI-GRU 2018:413

Abstract

The aim of particle physics to describe the fundamental particles and their interactions. The Standard Model which describes and predicts processes from particle collisions with a high precision, is one of the most successful theories in science. Despite its success, it has several shortcomings and to study those further and look for solutions to them, particle collisions are made in the Large Hadron Collider (LHC) at CERN. ATLAS is one of the experiments that study the collisions at the LHC. To improve the sensitivity for measuring rare processes and finding physics beyond the Standard Model, an upgrade of the LHC is underway. The High-Luminosity LHC (HL-LHC) will dramatically increase the collision rate and the ATLAS detector needs to be upgraded in order to cope with the higher rate. A part of the upgrade of the ATLAS experiment is the High-Granularity Timing Detector (HGTD) which helps to associate produced particles with the correct interactions. To do so, the HGTD uses sensors with high timing precision called Low-Gain Avalanche Diodes (LGADs) which are suited to the high-radiation environment at the HL-LHC.

With the higher expected proton-proton collision rate at the HL-LHC, more tracks will mistakenly be associated with the wrong collision. What HGTD does to correctly assign these tracks to the correct collisions, is to apply a separation in time of arrival with a timing resolution of 30 ps per track. If a charged particle hits two or three sensors, this requirement translates to 42 or 52 ps per hit in the sensors. This thesis investigates both the timing resolution and the detector response as a function of position on the surface of the sensors. It can be shown that most of the prototype sensors fulfill the requirement of having less than 42 ps per hit with a uniform response over the surface.

Sammanfattning

Målet med partikelfysik är att förklara de fundamentala partiklarna och dess interaktioner. Standardmodellen som beskriver och förutspår processer från partikelkollisioner med en hög noggrannhet, är en av de mest framgångsrika teorierna inom naturvetenskapen. Trots dess framgång har den flera brister och för att studera dem vidare och söka deras lösningar, genomförs partikelkollisioner i Large Hadron Collider (LHC) vid CERN. ATLAS är ett av experimenten som studerar dessa kollisioner i LHC. För att öka känsligheten för mätningar av sällsynta processer och söka efter fysik bortom Standardmodellen är en uppgradering av LHC planerad. High-Luminosity LHC (HL-LHC) kommer att dramatiskt öka kollisionsfrekvensen och i samband med det kommer ATLAS detektorn att behövas uppgraderas för att klara av att mäta kollisionerna. High-Granularity Timing Detector (HGTD) är en del av uppgraderingen av ATLAS-detektorn och kommer att hjälpa till att associera producerade partiklar med rätt kollisioner. För att uppnå det använder HGTD sensorer av typen Low-Gain Avalanche Diodes (LGADs) som är anpassade för strålningsmiljön vid HL-LHC.

Den förväntade högre frekvensen av proton-proton-kollisioner i HL-LHC kommer att leda till att fler spår blir felaktigt associerade till de individuella kollisionerna. Det som HGTD gör för att korrekt associera dessa spår med rätt kollisioner är att tillämpa en separation i ankomsttid med en tidsupplösning på 30 ps. Om spåret passerar två eller tre sensorer översätts detta krav till 42 eller 52 ps per träff. Denna uppsats undersöker både tidsupplösningen och responsen över ytan på sensorerna. Studien visar att flertalet av de prototypsensorer som har testats uppfyller kravet på att ha en tidsupplösning mindre än 42 ps per träff med en uniform signalrespons över ytan.

Contents

Chapter 1

Introduction

Particle physics aims to explain the fundamental particles in nature and their interactions. As the understanding of particle physics has progressed, with the latest discovery of the Higgs boson in 2012, there are still unanswered questions. The Standard Model (SM) is one of the most successful theories in science and explains the behavior of the known fundamental particles. The SM has several shortcomings, for example it does not describe gravity or the masses of the neutrinos. Another problem of the SM is that it accounts for only about 15% of the matter in the universe where the rest consists of dark matter. Furthermore, looking into the energy content of the universe, the SM explains roughly 4% with the rest being dark matter (24%) and dark energy (72%) [1]. To test the SM further and look for solutions to its flaws, the ATLAS experiment [2] at CERN, the European Organization for Nuclear Research, looks for new physics. In order to make the experiments more sensitive, upgrades are made. The High Granularity Timing Detector (HGTD) [3] is a proposed sub-detector system planned to be installed inside ATLAS before the start of the High Luminosity LHC (HL-LHC) [4] in 2026, which will increase the number of proton-proton collisions per time unit by a factor of $5-7$. As part of the preparations of its design, an analysis of proposed sensors for the HGTD is made.

1.1 Aim of the thesis

In order to build the HGTD, careful selection and characterization of its sensors are needed. To do so, test beam measurements are performed, where different sensors are tested in an environment which is similar to where particles collide in the ATLAS detector. By alternating conditions for the sensors under test, one can deduce the different behaviors and choose the most suitable one to be installed in the HGTD. This thesis analyzes various sensors measured in September 2017 with the main focus on the timing resolution and the spatial efficiency of these sensors.

1.2 Outline

In Chapter 2 the CERN accelerator complex together with the ATLAS experiment is introduced and explained with the overall design of the High-Granularity Timing Detector. In Chapter 3, the experimental setup of the test beam is described, together with a summary of how the data were collected. In Chapter 4 the methods of extracting the sensor properties is described with the results of these in Chapter 5. A discussion of the achieved results and conclusions are mentioned in Chapter 6 before a concluding outlook in Chapter 7.

1.3 Author's contribution

The author has been collaborating with the members of the HGTD Test Beam group and analyzed data collected in the measurement. A software package has been created by the author to analyze the collected data with the analysis and results discussed together with the HGTD Test Beam group. The author has been giving presentations at CERN for the same group discussing the timing resolution results as well the methods used. Additionally the author have been taking shifts during a test beam measurement. Results presented in this thesis are produced from the software which the author is solely responsible for.

Chapter 2

Background

2.1 Brief overview of particle physics

The Standard Model (SM) describes the smallest fundamental particles which are known and the interactions between them. The SM contains particles grouped into fermions those associated with matter and bosons which are the quanta of the fields mediating the interactions between particles. Fermions have half-integer spin and are subdivided into quarks and leptons, where the quarks are the up, down, charm, strange, top and bottom and the leptons are the electron, muon, tau and three corresponding neutrinos. Bosons have integer spin and are the photon, gluon, W-boson, Z-boson and the Higgs boson. All fermions and the W-boson have their antiparticle which have opposite-sign charge. In Figure 2.1 a table of the SM particles is shown. A hadron contains two or three quarks. The quarks are denoted with q and the antiquarks with $\bar{q}$. Baryons are ones which have three quarks, qqq and mesons have a quark and an antiquark, $q\bar{q}$. A common baryon is the proton with the quark content uud. The pion is a meson with possible quark combinations $u\bar{u}$, $d\bar{d}$, $u\bar{d}$ or $d\bar{u}$.

Despite the success of the SM, such as the discovery of the Higgs boson in 2012, there are phenomena which cannot be fully explained by the SM. For example the masses of the neutrinos and the existence of dark matter and dark energy. There are theories proposing an explanation of the dark matter, for example Supersymmetry (SUSY) which proposes a supersymmetric companion particle for each of the particles in the SM. Therefore, the aim is to understand the missing pieces in particle physics by searching for rare processes by colliding particles with high energy. Trying to answer the open questions within particle physics, the CERN organization searches for the answers using the Large Hadron Collider (LHC) [5].

2.2 The Large Hadron Collider

The flagship of the CERN accelerator complex is the Large Hadron Collider (LHC) which is a 27 km long circular accelerator, placed 100 m below the French-Swiss border outside Geneva, Switzerland. The LHC accelerates protons or either heavy ions which are then collided inside the four detectors, namely ALICE (A Large Ion Collider Experiment) [6], ATLAS (A Toroidal LHC Apparatus) [2], CMS (Compact Muon Solenoid) [7] and LHCb (LHC-beauty) [8].

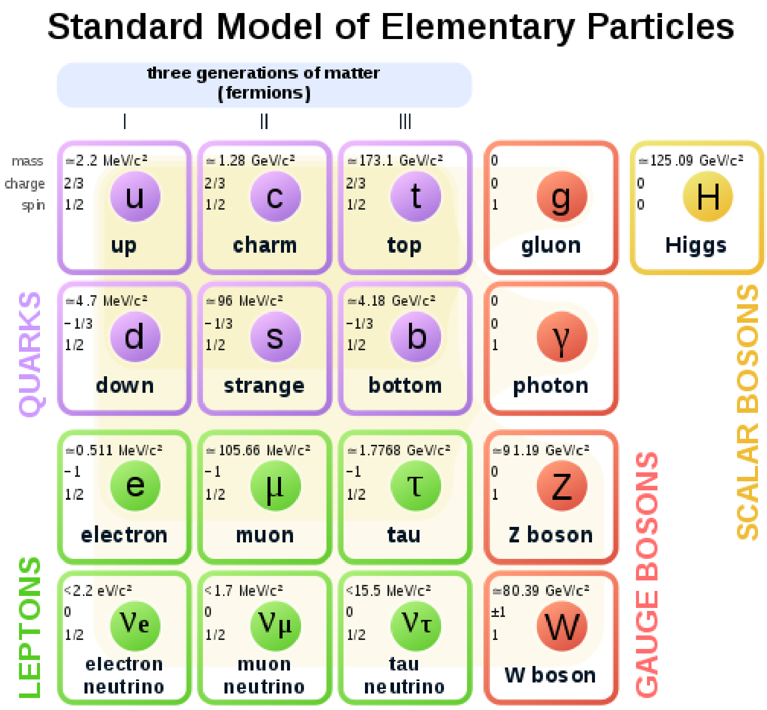

Figure 2.1: Particles of the Standard Model. Image credit: Wikipedia user MissMJ, distributed under a CC-BY 3.0 license.

Before the particles are injected in the LHC, they undergo a sequence of staged accelerations in the Linear Accelerator (Linac2), the Proton Synchrotron Booster (PSB), the Proton Synchrotron (PS) and the Super Proton Synchrotron (SPS). The protons originate from hydrogen gas which first passes through a source which heats the gas up creating a plasma. Under an applied electrical field, the electrons are stripped off from the plasma which leaves only the protons to continue within the pipe. Subsequently, these protons enters a chain of conductors which are charged positively or negatively along the pipe, causing them to accelerate by pushing them with an electric field. The chambers which cause protons to accelerate are the radiofrequency cavities. This makes the protons leave the Linac2 with an energy of 50 MeV which enters the next circular accelerator, the PSB. Inside it there are four superimposed synchrotron rings which causes the particles to gain a new energy of 1.4 GeV. These protons enter the PS, with a circumference of 628 m, where the electrical field accelerate them, and magnets keep the protons in orbit leading to an increased energy of 25 GeV. When the protons reach that energy, they continue to another larger accelerator, the SPS, with a circumference of 7 km. Inside the SPS, the protons accelerate until they have an energy of 450 GeV. Finally, when the protons reach this energy, they enter the LHC where they are injected into two pipes forming beams with opposite directions. Inside the LHC there are four crossing points, where each of the major detector systems are located. When they enter the LHC, the protons are grouped into bunches with 1.1×10^{11} protons, with a time separation of 25 ns and after ramping up the energy they reach 6.5 TeV. This leads to a collision energy of $\sqrt{s} = 13\,\mathrm{TeV}$[1] [5].

[1] The s denotes the Mandelstam variable, which is the square of the sum of four-momenta for incoming particles, $s = \sqrt{p_1^2 + p_2^2}$, where $p = (E/c, \mathbf{p})$.

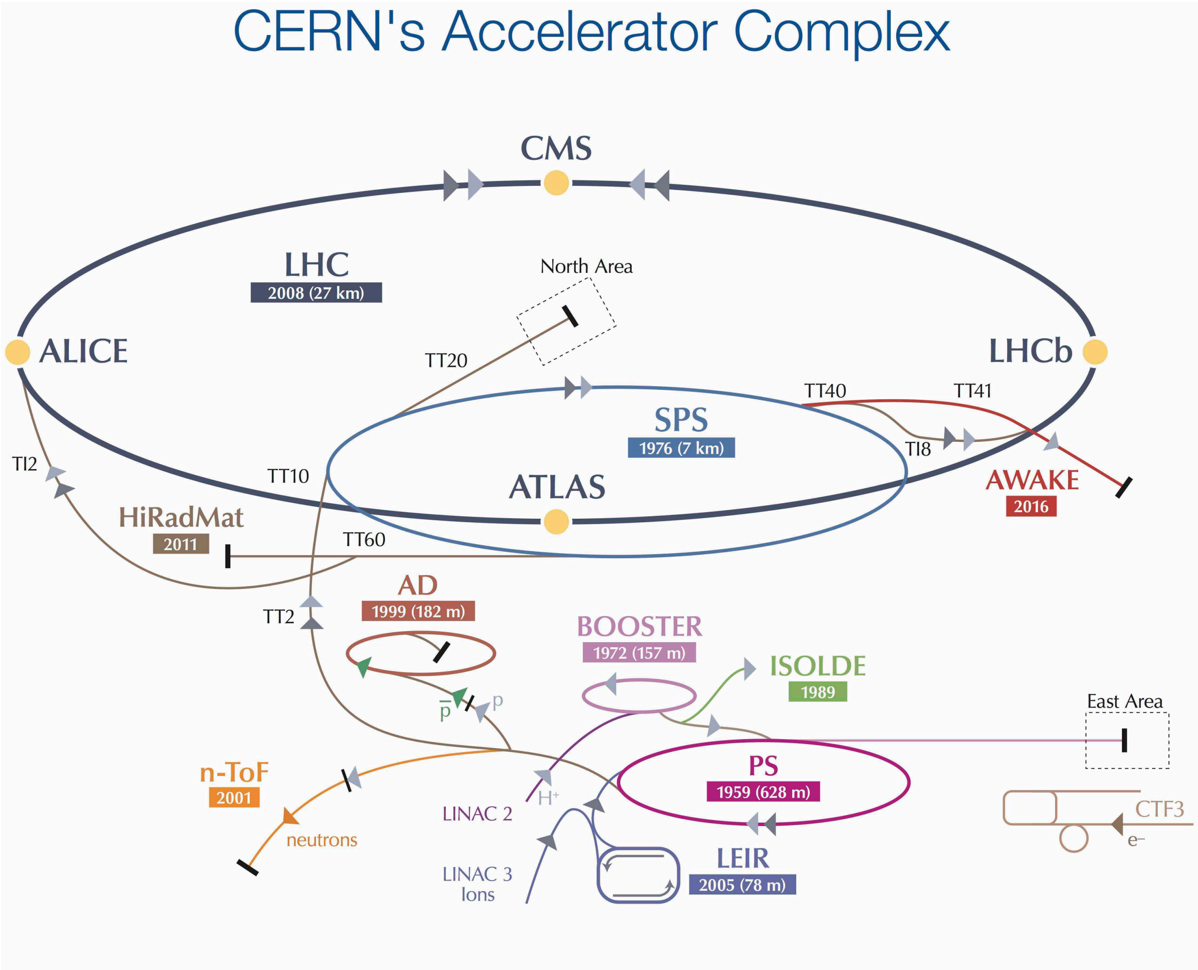

Figure 2.2: CERN's accelerator complex. Courtesy of CERN.

During the first period of data taking in 2010 − 2013 named Run 1, the collision energy was $\sqrt{s} = 7\,\text{TeV}$ in 2011 and $\sqrt{s} = 8\,\text{TeV}$ in 2012 for proton-proton collisions. The total integrated luminosity recorded by ATLAS was $\int \mathcal{L}dt = 5.08\,\text{fb}^{-1}$ [2] for 2011 and $\int \mathcal{L}dt = 21.3\,\text{fb}^{-1}$ in 2012 [9], where $\mathcal{L}$ is the instantaneous luminosity. The current Run 2, operating from 2015 with the center-of-mass collision energy of $\sqrt{s} = 13\,\text{TeV}$, has recorded up until November 2018 $\int \mathcal{L}dt = 149\,\text{fb}^{-1}$ [10]. The total integrated luminosity recorded by ATLAS is closely the same recorded by CMS [11]. A schematic view of the CERN accelerator complex is shown in Figure 2.2. The collision of protons causes creation of new particles which are registered by large complex detectors, for example the ATLAS detector.

2.3 The ATLAS detector

A brief description of the ATLAS detector is presented here, for a more complete description see for example [2]. The detector measures 25 m in height, 44 m in length and weighs around 7000 tonnes. It has a cylindrical shape around the collision point, and

[2] $1\,\text{barn} = 1\,\text{b} = 10^{-28}\,\text{m}^2$, which is a unit for cross section, that is the probability for processes to happen.

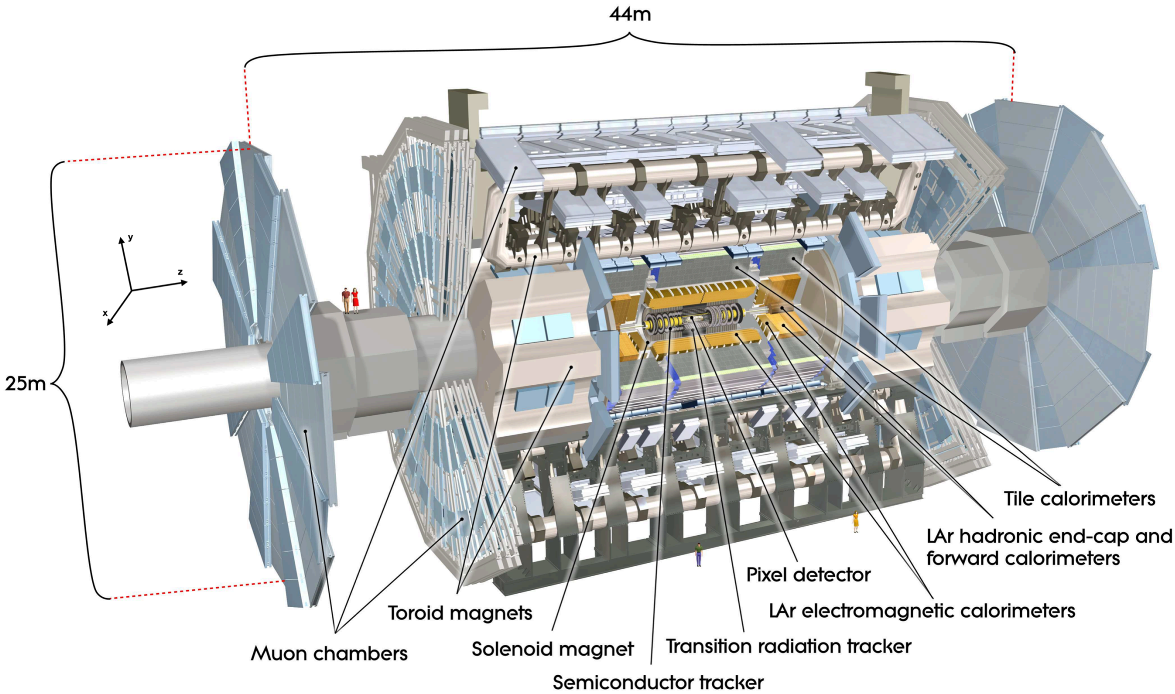

Figure 2.3: The ATLAS detector [2].

different layers of sensors are installed to identify and measure the produced particles. These so-called sub-detector systems can be grouped into three main parts: the inner detector, the calorimeters and the muon spectrometer. A view of the detector can be seen in Figure 2.3. In ATLAS a right-handed coordinate system is used with origin at the collision point. The x-axis points towards the center of the LHC ring and the y-axis points upward with the z-axis along the beam line. Using the polar angle θ, which is defined as the angle from the positive z-axis, the pseudorapidity is defined as

$$\eta = -\ln\left(\tan\frac{\theta}{2}\right). \tag{2.1}$$

The ATLAS detector can be subdivided into two main geometric regions, the barrel at $|\eta| \lesssim 1.5$, and the end-caps at $|\eta| \gtrsim 1.5$. The barrel is primarily made of cylindrical volumes covering the central part around the collision point, where the end-caps are disk-shaped layers positioned perpendicular to the beam line, further away from the interaction point. A cross sectional view of the ATLAS detector in the plane perpendicular to the beam line, together with illustrations of how particles produced in the collisions interact in the detector, is shown in Figure 2.4.

2.3.1 Inner detector

The Inner Detector (ID) is situated closest to the collision point with the main objective to observe tracks of charged particles and measure their momenta. It consists of three sub-detector systems, namely the Pixel detector, the Semiconductor Tracker (SCT) and the Transition Radiation Tracker (TRT). The ID measures 6.2 m in length and 2.1 m in diameter and covers the area of $|\eta| < 2.5$. The ID is surrounded by a solenoid mag-

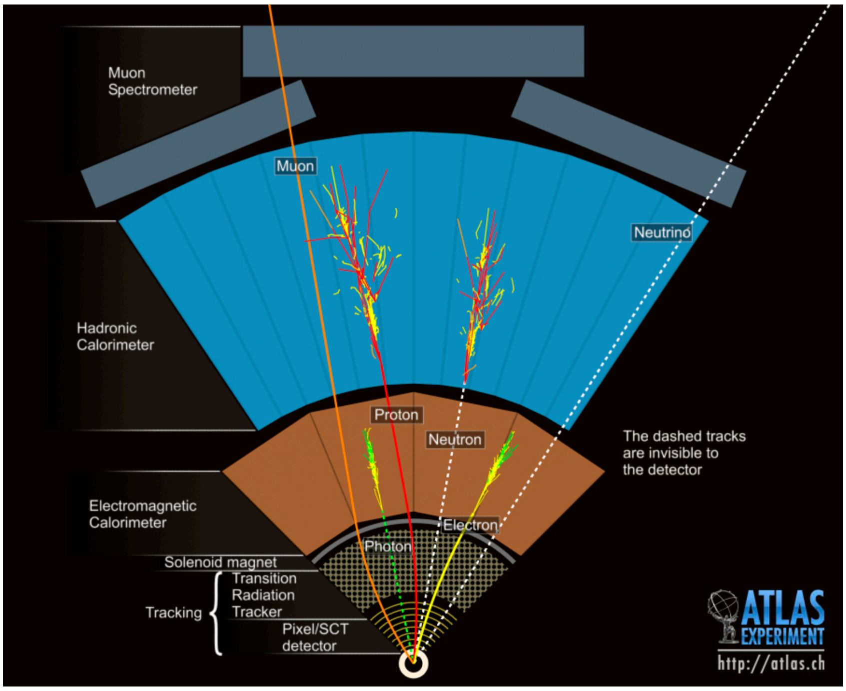

Figure 2.4: ATLAS sub-detectors and visualizations of detector signatures of commonly produced particles [12].

net which generates a field of 2 T causing charged particles to bend their trajectory. A schematic overview can be seen in Figure 2.5.

Pixel detector

Closest to the collision point, the flux of newly created particles is highest. To ensure that tracks of these particles are registered, a highly granular pixel system is installed. It consists of four cylindrical pixel layers where the innermost one was installed for Run 2 of the LHC, namely the Insertable B-layer (IBL) [13]. The layers are installed at innermost radius of $R = 35\,\mathrm{mm}$ and the outermost at $R = 122\,\mathrm{mm}$. The technology is based on n-type silicon sensors, where the passing particles produce electron-hole pairs creating a current. In total there are 2024 silicon pixel modules, where in the IBL the pixel size is $50\,\mu\mathrm{m} \times 250\,\mu\mathrm{m}$ while the other three layers have a pixel size of $50\,\mu\mathrm{m} \times 400\,\mu\mathrm{m}$ giving a total of 92 million readout channels.

Semiconductor Tracker

Moving radially away from the collision point one finds the SCT, which can be seen in Figure 2.5. The single-sided sensors measure $640\,\mathrm{mm} \times 636\,\mathrm{mm}$ with a strip pitch of $80\,\mu\mathrm{m}$. There are four double layers surrounding the pixel detector in the barrel region placed parallel to the beam and nine disks in each end-cap region where the sensors are placed perpendicular to the beam line.

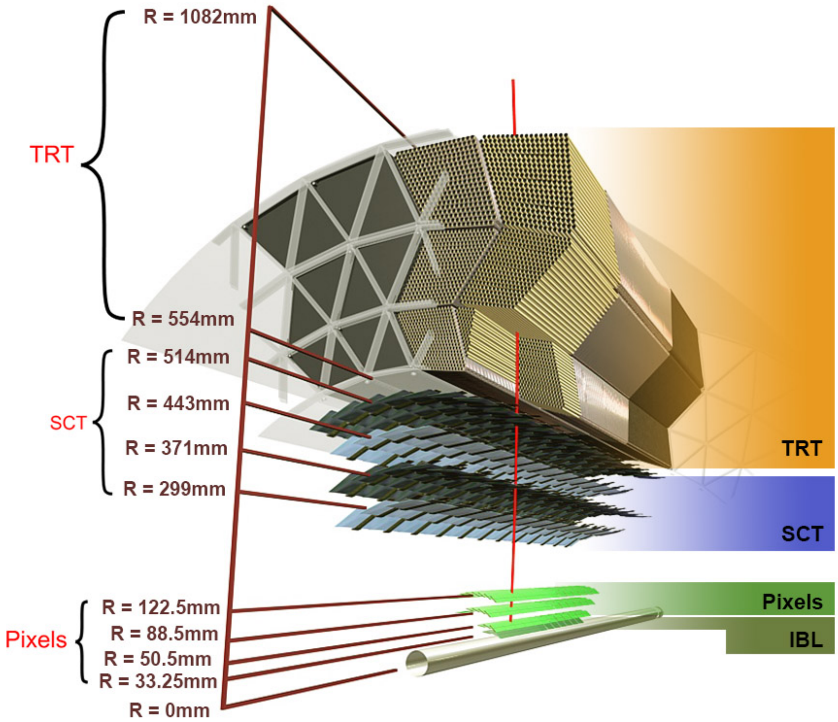

Figure 2.5: Cross-sectional view of the Inner Detector [13].

Transition Radiation Tracker

The outermost detector subsystem of the ID is the TRT. It has a trapezoidal structure where each segment consists of multiple gas-filled tubes at 554 mm $< R <$ 1082 mm. In total there are 351 000 straws filled with xenon gas and a gold wire in the center. When a charged particle traverses the straw tube, the gas inside gets ionized which leads to free electrons. These freed electrons are subjected to a voltage in the straw tube, causing them to accelerate which causes additional ionization. They lead to the wire at the center of the straw, creating an electronic readout from the straws. The straw tubes have a layer of plastic to create transition radiation which originates from a traversing particle. This transition radiation comes from the different dielectric constants between the gas and the plastic with a certain probability to emit radiation. The amount of radiation is proportional to the Lorentz boost factor ($\gamma = E/mc^2$) and helps to distinguish between electrons and hadrons, which are a lot more massive.

2.3.2 Calorimeters

The calorimeters are responsible for measuring the energy of particles. The two main parts are the electromagnetic calorimeter and the hadronic one. The calorimeters cause a particle shower from the incoming high-energy particle, which stops when the threshold energy of creating new subsequent showers is reached. Electromagnetic particles (electrons, positrons and photons) are absorbed in the EM calorimeter whereas the hadrons (for example protons) continue to the hadronic calorimeter where they leave most of their energy. The placement of the calorimeters inside ATLAS is shown in Figure 2.6.

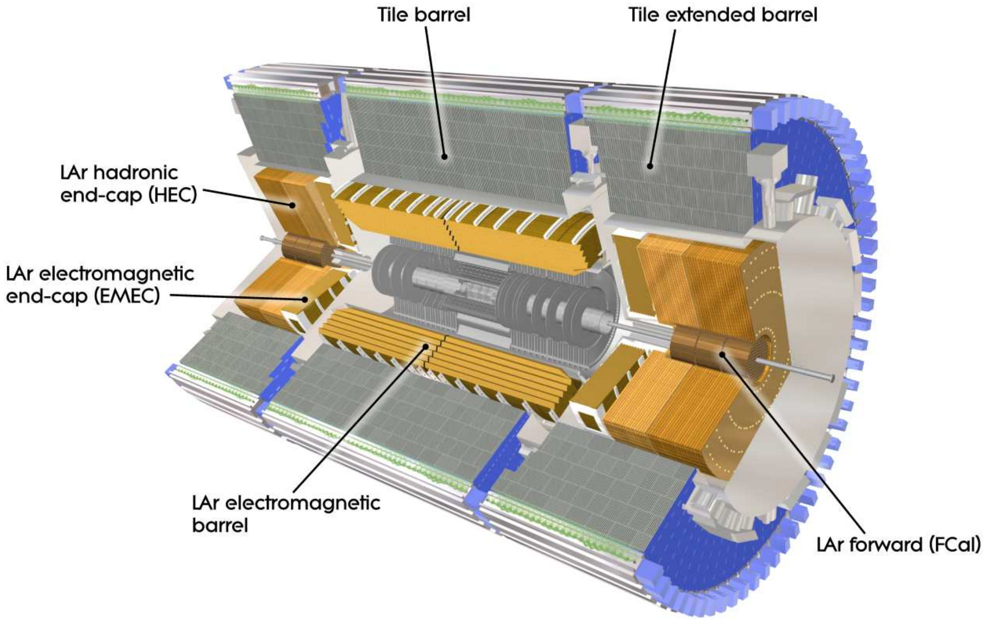

Figure 2.6: View of the calorimeters [2].

Electromagnetic calorimeter

The active material in the EM calorimeter is liquid argon (LAr) and the absorption material is lead. The barrel part is placed at $|\eta| < 1.475$ and the end-caps at $1.375 < |\eta| < 3.2$. The end-caps have two co-axial wheels and at $2.5 < |\eta| < 3.2$ a higher granularity. The shower inside the calorimeter is created by an ionization of the liquid from an incoming photon or an electron, which creates electron-positron pairs that also react with the absorber material. The freed electrons will drift towards an anode under an applied electric field creating an amplified signal.

Hadronic calorimeter

Outside the EM calorimeters one finds the hadronic calorimeter, the Tile barrel at $|\eta| < 1.7$, and end-caps at $1.5 < |\eta| < 3.2$. The Tile calorimeter uses plastic scintillators as active material with iron as absorption material. The energy is read out from light emitted from the scintillators. The hadronic calorimeter in the end-caps uses LAr as active material with copper as absorber material. This calorimeter works in a similar manner as the EM one, causing a shower of hadrons. The hadronic showers have a different development from the EM ones, where several processes contribute to production of new hadrons inside the calorimeter.

Forward calorimeter

The Forward Calorimeter (FCAL) extends the EM and the hadronic calorimeter to $3.2 < |\eta| < 4.9$. The EM calorimeter which is closer to the beam line has copper as the absorber material and LAr as active material. Further away is the hadronic calorimeter with LAr as the active material and tungsten as the absorber material. It is constructed to be sufficiently dense to absorb the high flux of incoming particles.

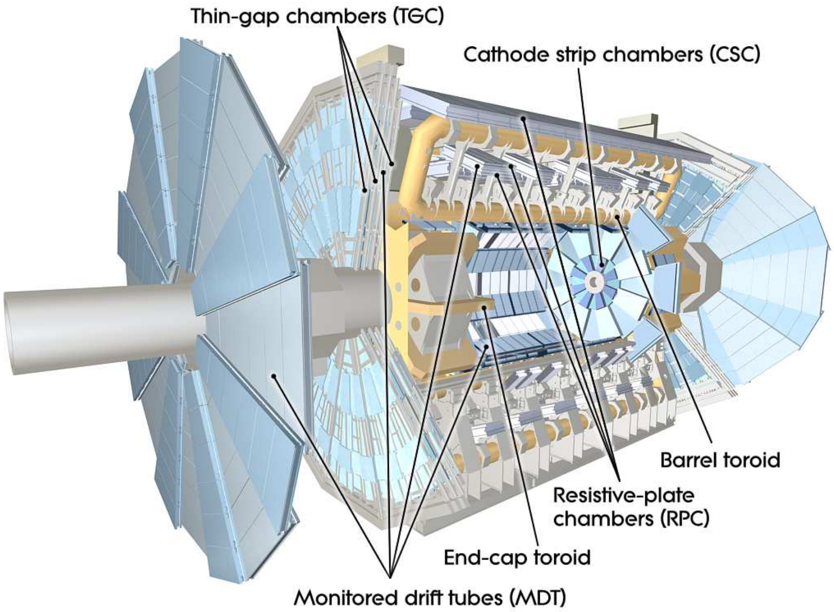

Figure 2.7: The muon system and its main parts in ATLAS [2].

2.3.3 Muon spectrometer

The outermost main part of the ATLAS detector is the muon system. Its main purpose is to detect muons which are rarely stopped by the calorimeters. The spectrometer contains three so-called stations which each can reconstruct track segments from a passing particle. Both in the barrel and end-cap parts, there is a toroidal magnet system, with eight coils in the barrel and eight in each end-cap. These enable a momentum measurement by bending the trajectory of a traversing muon. For $|\eta| < 2.0$, Monitored Drift Tubes (MDT) are used. They consist of an Ar-based gas, which gets ionized when the muon traverses it. Under an applied electrical field, electrons get freed and accelerates to the center of the tube towards a thin anode wire which generates a signal. For $2.0 < |\eta| < 2.7$, Cathode Strip Chambers (CSC) are installed instead of MDTs, due to the larger particle flux. These are based on the same gas with a multi-wire configuration.

Furthermore, detectors used to trigger the recording of data are installed. In the barrel region, the Resistive-Plate Chambers (RPCs) are located at $|\eta| < 1.05$, and in end-caps at $1.05 < |\eta| < 2.4$ the Thin Gap Chambers (TGCs). The RPCs use a gaseous system which gets ionized by the traversing muon, whereas the TGCs use a multi-wire technology which is adapted for the high flux for the high $\eta-$range.

2.4 High-Luminosity LHC

To improve the sensitivity of searches for physics beyond the SM and higher-precision measurements of for example the Higgs boson, an upgrade program of High-Luminosity LHC is introduced (HL-LHC) [4]. The current highest levels of instantaneous luminosity is $\mathcal{L} = 2 \cdot 10^{34}\,\mathrm{cm}^{-2}\,\mathrm{s}^{-1}$ with a total recorded integrated luminosity by ATLAS for Run 1 and Run 2 of $\int \mathcal{L}dt = 175.4\,\mathrm{fb}^{-1}$ [9, 10]. With the upgrade the instantaneous luminosity will reach up to $\mathcal{L} = 7.5 \cdot 10^{34}\,\mathrm{cm}^{-2}\,\mathrm{s}^{-1}$ and a total recorded integrated luminosity of $\int \mathcal{L}dt = 3000\,\mathrm{fb}^{-1}$ during a time period of over a decade [3]. A road-map of the HL-LHC program can be seen in Appendix A where the start is scheduled to be in 2026.

The protons in the LHC come in bunches of approximately 10^{11} protons, and they collide with each other with a number of proton-proton collisions μ. For multiple bunch crossings, an averaged value of the number of collisions $\langle\mu\rangle$ is commonly used. Under typical Run 2 conditions the value is $\langle\mu\rangle = 30$ while at the HL-LHC this number is increased up to $\langle\mu\rangle = 200$. Typically one collision is of interest, where the others are referred as pileup. The increase of $\langle\mu\rangle$, is one of the challenges for detectors to cope with. At that increased collision rate it becomes challenging to separate the many close-by interactions and correctly associate the tracks to the right vertices.

2.5 High-Granularity Timing Detector

In each bunch crossing, the collisions occur at slightly different times with an expected spread of 175 ps [3]. The majority of the particle flux from the collisions are directed in the forward region. With the expected rate at the HL-LHC, it becomes increasingly difficult to associate tracks to the right vertices even if the spatial resolution is high. With collisions being close to each other, the tracks which are close to the beam line could mistakenly be recognized from the same vertex, causing a detection of multiple different collisions. A proposed solution to distinguish those tracks is by a good time resolution which separates those tracks and vertices in time. A part of the upgrade of ATLAS detector proposed to do exactly this is the *High-Granularity Timing Detector* (HGTD) [3].

The HGTD consists of two circular disks placed in between the ID and the end-cap of the calorimeter at $z = \pm 3.5$ m with an active area at $120\,\text{mm} < R < 640\,\text{mm}$, corresponding to $2.4 < |\eta| < 4.0$. It has a thickness of 75 mm and Figure 2.8 shows the view of the HGTD with the active area. Inside the main vessel of each end-cap there are two cooling disks. On each side of the cooling disks, narrow rectangular staves are placed with sensor modules. The disks with the staves are structured along R to measure traversing particles with on average three hits at $R < 320$ mm and two at $R > 320$ mm. This is achieved by placing the modules with overlap between the front and the back of each cooling disk. Figure 2.9 shows the cooling disks with the rectangular staves and their relative orientation, and Figure 2.10 shows the module placement and overlaps near $R = 320$ mm.

The HGTD is designed to measure tracks from minimum-ionizing particles (MIPs) with a timing resolution of 30 ps, which helps to reduce the effects from pileup with a factor of $175/30 \approx 6$. For a track hitting two or three sensors, this corresponds to a timing resolution for a sensor of 42 or 52 ps per hit, respectively. The choice of sensor technology which fulfills the timing resolution and spatial requirements in the HGTD are the Low-Gain Avalanche Diodes. These have been developed by, among others, the RD50 collaboration [14] together with industrial partners. A technical proposal [3] for the HGTD has been accepted by the LHCC (LHC Experiments Committee) as a part of the Phase-2 upgrade of the ATLAS experiment.

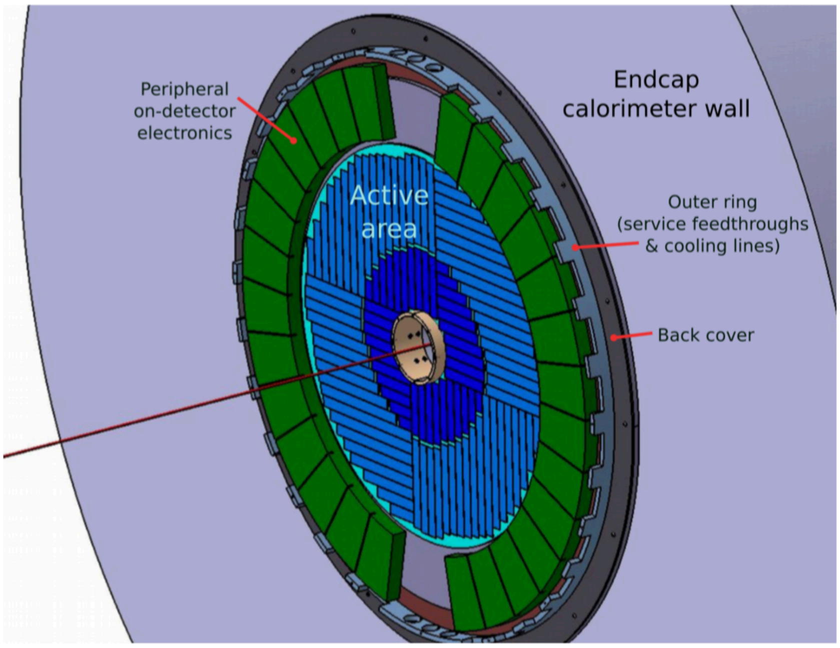

Figure 2.8: Overview of the HGTD. The active area has two sensor placement densities, the larger one closer to the beam. The green part shows the placement of peripheral on-detector electronics [3].

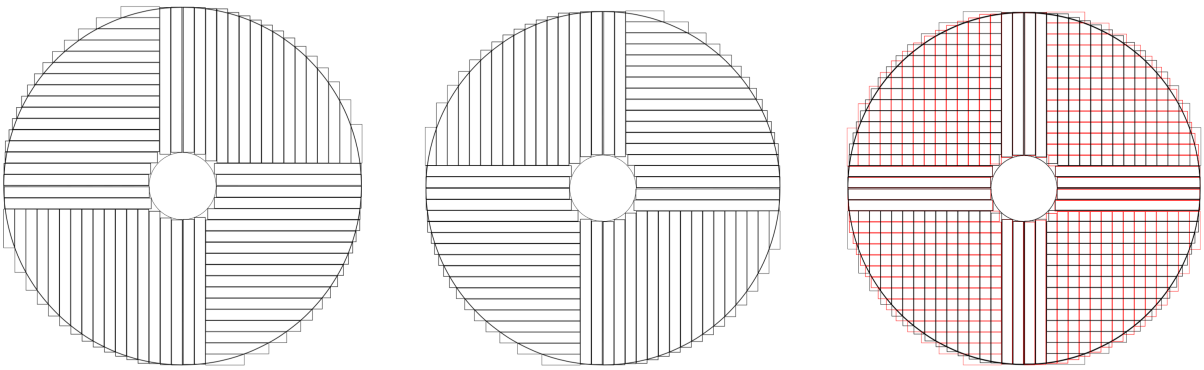

(a) First cooling disk. **(b)** Second cooling disk. **(c)** Overlay.

Figure 2.9: First and second cooling disks of the HGTD with staves and the overlay of both. The view is seen from the interaction point [3].

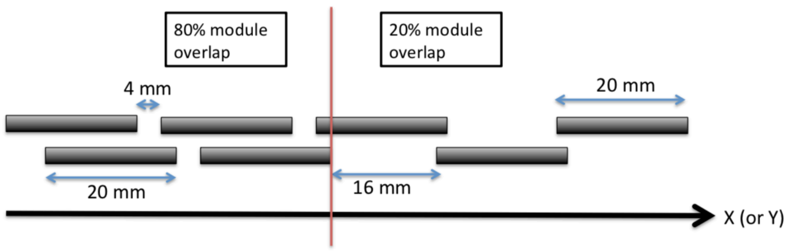

Figure 2.10: Illustration showing how the modules overlap between the back and the front of a cooling disk in the HGTD. The vertical line marks the transition region between large and small overlap at $R = 320\,\mathrm{mm}$ [3].

2.5.1 Low-Gain Avalanche Diodes

Low-Gain Avalanche Diode (LGAD) [15,16] is a n-on-p type silicon detector adapted for high-energy physics applications. A schematic figure of a LGAD can be seen in Figure 2.11. It is an avalanche-diode detector where a high applied electrical field causes a multiplication of the created electron/hole pairs, in this sense creating an avalanche. This enables a fast readout of the signals, which is one of the purposes of using this type of sensors. They are designed to be resilient to the high radiation doses expected at the HL-LHC [17]. The structure of it has a n-p-type doping with an additional highly doped thin p-layer which is the gain layer. This extra layer causes a multiplication of the charge collection, namely the gain. Typically in standard n-on-p-type sensors, the gain can reach up to approximately 1000. This has a disadvantage causing the noise to be increased which affects the signal [15]. Therefore a lower gain and a good signal-to-noise ratio is preferable for noise-sensitive applications. The LGAD is designed to have a gain of around 20.

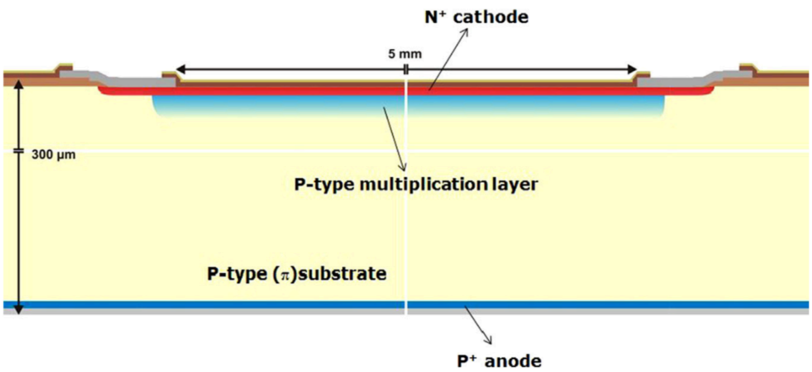

Figure 2.11: Cross-sectional view of a LGAD. The extra p-type layer is the gain layer aimed to increase the readout signal [16].

Chapter 3

Test beam measurement

This section describes the setup used to measure sensors which have been chosen as candidates for the HGTD. Along with the experimental setup, the section mentions the sensors used for the September 2017 test beam measurement, and a description of how the data was collected.

3.1 Experimental setup

The setup for analyzing the sensors can be divided into two parts, one in which the sensors are located, and a beam telescope which is in front of and behind the sensors. Figure 3.1 shows the setup of the test beam measurement. Through the setup a beam of pions with an energy of 120 GeV traverses, which originates from the SPS at CERN. In the middle part of the setup, there are up to eight different sensors installed, each with a readout board through which the bias voltage U_b over the sensor can be altered, and the signals read out with an oscilloscope. Among these sensors there are two types, one which is used for timing reference measurements, the Silicon Photo Multiplier (SiPM), and several Devices Under Test (DUT) which are of interest to measure, in this context the LGAD sensors. The sensor platform, where the DUTs are located, is inside a cooling box for which the temperature can be changed during the measurement. The second part of the setup, the telescope, consists of six plates of silicon pixel sensors which are called MIMOSAs, a FE-I4 unit, which is a fast readout pixel sensor, and a scintillator. The MIMOSA planes' purpose is to reconstruct a track from the pion by combining hits in all of the planes. The FE-I4 sensor is together with the scintillator responsible for the trigger to record data. The FE-I4 with a pixel size of $50\,\mu m \times 250\,\mu m$ have a so-called masking area, which is selected to match the size of the DUTs and the SiPM to trigger for tracks passing the area. The data from the MIMOSAs are recorded to a National Instrument (NI) crate. Additionally there is a Trigger Logic Unit (TLU) which gives the signal for when to record the data for the oscilloscopes and the NI crate. The telescope used for this test beam setup is an EUDET-type beam telescope where a setup called AIDA is used [18].

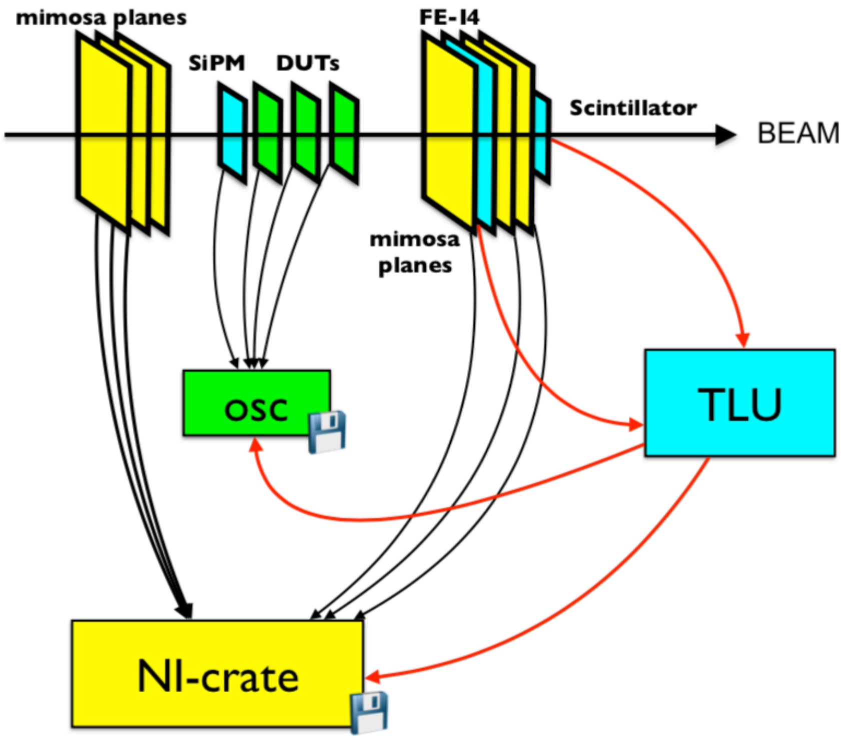

Figure 3.1: The test beam setup. In the middle of the setup are the DUTs which are of interest. The figure also show the signals used to trigger readout of the data [19].

3.2 Tested sensors

Among the DUTs there are three different types of sensors, those with a circular pad, a single square pad, and an array of square pads, used for the September 2017 test beam measurement. For the array-pad sensors, each pad is connected to either the same or different oscilloscopes, since an array sensor has up to four channels. The sensors have an effective readout area of $1\,\mathrm{mm}^2$ with the exception of the circular one which has $0.8\,\mathrm{mm}^2$. They have a thickness of $50\,\mu\mathrm{m}$ for the active layer and a resistance of $4.7\,\mathrm{k}\Omega$ in the transimpedance amplifier for the readout board. The sensors are listed in Table 3.1 with type of sensor, bias voltage used, and the type of doping on the additional gain layer. The W4-RD01 sensor does not have the information about the resistance, which is assumed to be the same as for the other sensors. Additionally each sensor's gain-layer doping dose is given in Table 3.1. The W4-S204 is a neutron-irradiated array-pad sensor with a fluence of $6 \times 10^{14}\,\mathrm{n_{eq}/cm^2}$. The reference sensor SiPM, has a rectangular area of $9\,\mathrm{mm}^2$ and overlaps with the DUTs along the beam line.

Sensor	Pad Type	$T = 22\,°C$ Range of U_b [V]	$T = -30\,°C$ Range of U_b [V]	$T = -40\,°C$ Range of U_b [V]	Gain doping layer dose [atoms/cm^2]
50D-GBGR2	Circular	$220 - 320$	–	–	D (Boron) [20]
W4-LG12	Single	$80 - 125$	–	–	2×10^{13} (Boron) [21]
W4-RD01	Array 2 channels	$80 - 120$	$40 - 60$	–	2×10^{13} (Boron) [21]
W4-S1022	Single	$80 - 110$	$40 - 90$	$30 - 90$	2×10^{13} (Boron) [21]
W4-S1061	Single	$80 - 150$	$40 - 90$	$30 - 80$	2×10^{13} (Boron) [21]
W4-S203	Array 1 channel	$80 - 120$	$45 - 70$	$20 - 60$	2×10^{13} (Boron) [21]
W4-S204	Array 3 channels	–	$200 - 300$	$200 - 270$	2×10^{13} (Boron) [21]
W4-S215	Array 4 channels	$80 - 125$	$35 - 80$	$40 - 65$	2×10^{13} (Boron) [21]
W9-LGA35	Single	$180 - 250$	–	–	1×10^{15} (Gallium) [22]

Table 3.1: List of tested sensors during the September 2017 test beam measurement. For array-pad sensors, the number of connected channels are listed. Missing information means that the sensor has not been tested for given temperatures. The gain-layer doping dose for 50D-GRGR2 is missing with reference ”D” which is highest one compared to other ones from the same producer.

3.3 Data taking

When a pion traverses the test beam setup as shown in Figure 3.1, a coincidence between signals in the FE-I4 and the scintillator triggers readout. This enables to record the data in an *event*, which is a time window for triggered readout data. The oscilloscope records the data from all connected LGADs and the SiPM, and the telescope saves the location of the hits on the MIMOSAs event-wise. During the test beam measurement a set of *runs* have been taken, which each comprise approximately 200 000 events. Typically each run is part of a *batch* which characterizes a consistent setup in terms of bias voltage of the sensors and the temperature of the cooling box where the LGADs are contained. A batch typically contains multiple runs. The complete list of runs, batches, bias voltages of the sensors connected to the oscilloscopes, and temperatures, are listed in Appendix B in Tables B.1 and B.2.

3.4 Sensor data

The oscilloscopes used in the test beam measurement are two Agilent Infiniium DSO9254A with a sampling rate of 10 GSamples/s per channel [19]. The data from sensors are read out with the oscilloscopes, and each event contains 1002 samples. The signal is the voltage with negative values which has been inverted to positive values. The time distance between points corresponds to 0.1 ns which gives a readout window of 100.1 ns. An example readout waveform from a LGAD is shown in Figure 3.2.

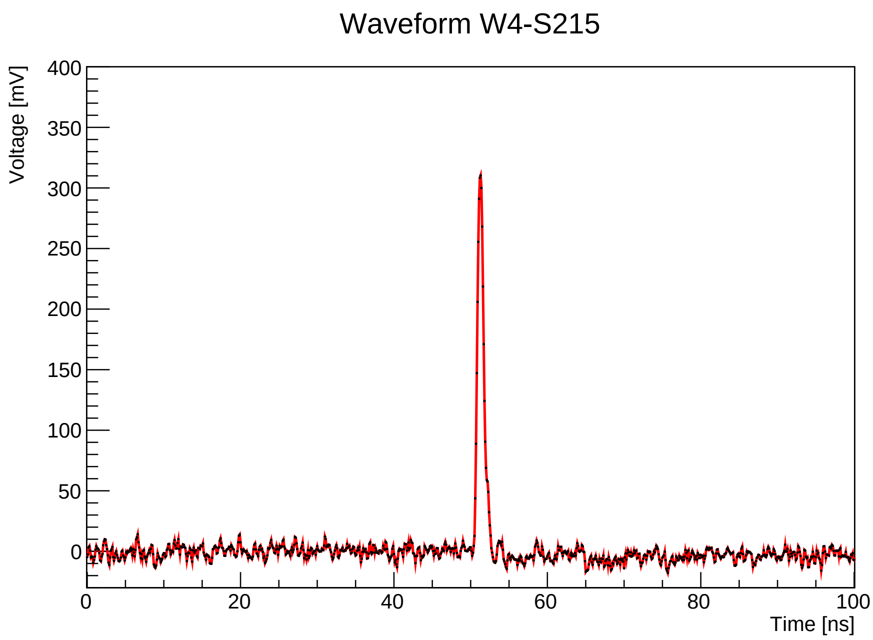

Figure 3.2: Example of a waveform for the array-pad sensor W4-S215. The figure represents a typical event, which has a time span of 100.1 ns with 1002 samples.

3.5 Telescope data

The TLU also triggers the NI crate to collect data which records the hits in the MIMOSA sensors. For each event, data are saved describing the location on the MIMOSAs where the particles from the beam has hit. The MIMOSA sensors have a pixel size of 18.4 µm × 18.4 µm with a total size of 10.6 mm × 21.1 mm [18]. The data from the MIMOSAs are used to reconstruct tracks which can be used to extract the location where the particle passed through on the DUTs themselves. For this thesis, the data analyzed was recorded before the author has started working on the project, and tracking and sensor alignment had been performed. More information on how this is done can be found in [23]. The tracking data is used to analyze the points of passage on the DUTs.

Chapter 4

Analysis methods

In this chapter methods for extracting signal characteristics from the LGADs are presented together with methods for combining track-based information from the MIMOSAs with the signals from the LGADs. Section 4.1 explains how sensor data are treated, starting with the determination of noise and pedestal. It also presents methods to extract characteristics of a signal from a passing particle, that is pulse amplitude, rise time, gain, and time location of a signal. Additionally, the way of calculating the timing resolution of the sensor is explained. Section 4.2 describes how the track-based data is used to examine spatially dependent signal properties. Also, the efficiency for each pixel of the sensor to measure a passing particle is explained.

4.1 LGAD signal analysis

This section explains the reconstruction of the data from the sensors. Here, the methods are applied to each signal from an event.

4.1.1 Noise characteristics

To understand the noise characteristics, one studies how the sensor behaves without a signal. To do this, a threshold of 20 mV is used, which tells us that the data point exceeding it is considered as a signal. The chosen value of 20 mV is based on multiple events from all of the sensors. The sample for calculating noise characteristics is chosen to be a range from the beginning of the waveform, up until the data sample exceeding the threshold, with an additional subtraction of three data samples to avoid signal contamination. All data samples are selected if the threshold is not exceeded. Based on the selected range, the average value and the standard deviation of the selection is calculated, which here are referred to as *pedestal* U_P, and *noise* σ_{noise}. The pedestal is a value which needs to be subtracted from the read out values, to maintain the correct value of the pulse amplitude. The noise on the other hand is the fluctuations in the absence of signal. These two values are therefore needed to understand how the signal is observed.

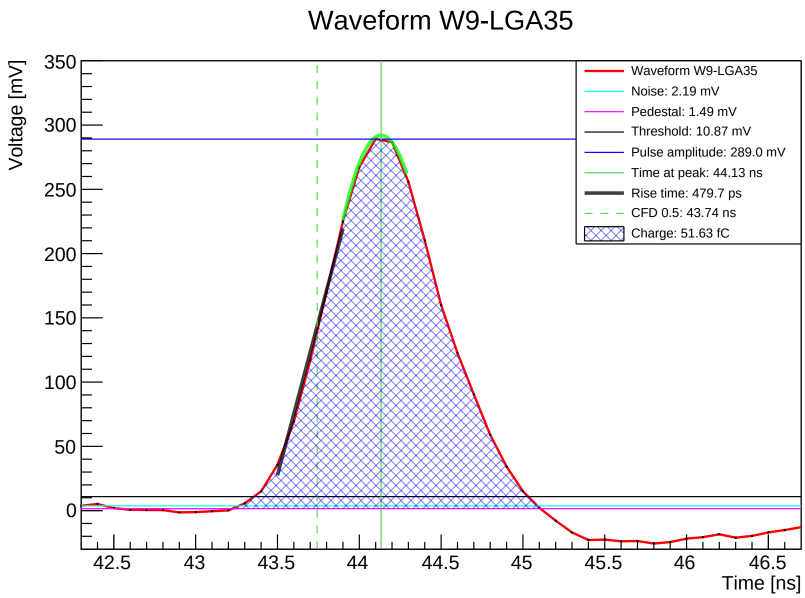

Figure 4.1: This plot shows the waveform of a signal with the fits to find the pulse amplitude and rise time, lines marking the time locations at peak of the pulse and 50% of the rising edge and the area for the collected charge.

4.1.2 Signal characteristics

This section presents the methods for finding a signal, determining the pulse amplitude, rise time, time locations and how the gain is calculated. The different characteristics can be seen in Figure 4.1.

Defining criteria for a signal

When the noise levels have been determined, one can begin selecting the signal. To do so, a new threshold (different from the one mentioned in Section 4.1.1) U_S is introduced based on noise and pedestal,

$$U_S = N \cdot \sigma_{\text{noise}} + U_P \tag{4.1}$$

where N is a constant exceeding the noise. The choice of N is based on the assumption that the noise follows a normal distribution, so-called Gaussian noise. N is chosen to not exceed a true pulse and not to select noise, assuming the data sample follows a normal distribution. Taking an example of a 3σ level, the probability of one data sample exceeding that level is $P_1 = P(z \geq 3) = 0.135\%$, where z is the variable of the cumulative probability distribution function of a standard normal distribution. The probability for 1 in 1000 data samples exceeding the same level is $P_{1000,3\sigma} = 1 - (1 - P_1)^{1000} = 1 - P_{\text{all below}} = 72.77\%$. The condition set is to require that this probability $< 1\%$, which leads to $N = 4.27$.

An additional constraint on the number of samples above the threshold, N_{samples} is used. This helps to remove pulses which passes the threshold but do not have the duration expected for a signal. The selection is based on a two-dimensional distribution of the number of samples, and one of the maximum sample value above threshold U_S. By studying the two quantities for each event, one can see which N_{samples} can be chosen to reject pulses which are noise. This is done for lowest bias voltage to get the smallest distance between the area with majority of events and origin in Figure 4.2c. The sensor W4-S203 is used as an example here at $U_b = 80\,\mathrm{V}$ and averaged noise value of 2.4 mV. The number of samples above the threshold U_S is shown in Figure 4.2a and maximum sample value above U_S in Figure 4.2b with the plot showing the correlation between both quantities in Figure 4.2c. From the last plot, $N_{\mathrm{samples}} > 14$ gives signals from pions, while for $N_{\mathrm{samples}} < 5$ is noise. To avoid these signals, a number of $N_{\mathrm{samples}} = 8$ is set in between the majority of signals and signals which are treated as noise for W4-S203. The same type of argument is used for the other sensors which are shown in Appendix C. The choices of N_{samples} for each sensor are shown in Table 4.1. W4-RD01 has higher N_{samples} than for other DUTs, since the sensor has slower signals with larger pulse amplitudes.

Sensor	N_{samples}
50D-GBGR2	5
SiPM	36
W4-LG12	8
W4-RD01	32
W4-S1022	7
W4-S1061	8
W4-S203	8
W4-S204	3
W4-S215	8
W9-LGA35	5

Table 4.1: Limit of number of samples above U_S for each sensor. Signals which have number of samples fewer than N_{samples} are rejected.

Pulse amplitude and time location at maximum value

When a pulse has been found, the pulse amplitude and the time location of the pulse can be determined. Using a second degree fit on five samples centered around the peak, one can extract the maximum value and the time location of it. The obtained pulse amplitude is then pedestal-corrected.

Rise time and time location at 50% of the crossing edge

The rise time is a measure of the steepness of the signal. It is calculated by selecting samples between 10% and 90% of the maximum sample value of the rising edge. A linear fit is made for which the rise time is calculated with respect to the pedestal corrected maximum sample value. An alternative time location at the rising edge with respect to the pedestal corrected maximum sample value, also called the Constant Fraction Discriminator (CFD), is determined. The CFD method is used to evaluate the time location at 50% of the maximum sample value.

Gain

Lastly, measuring the amplification factor of the deposited charge from the additional gain layer is of interest. To calculate the factor, the deposited charge within a sensor is

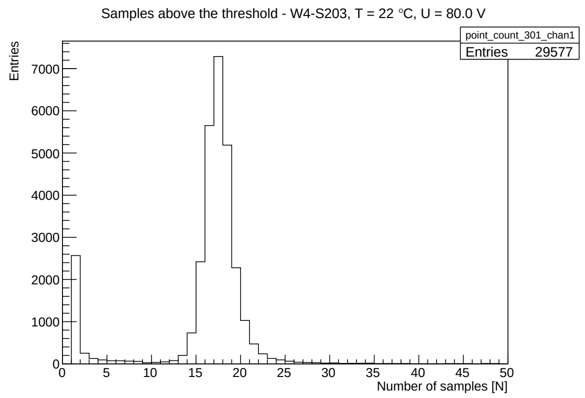

(a) Number of samples above U_S.

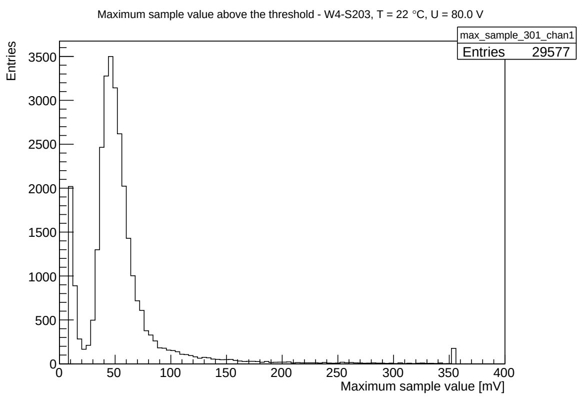

(b) Maximum sample value above U_S.

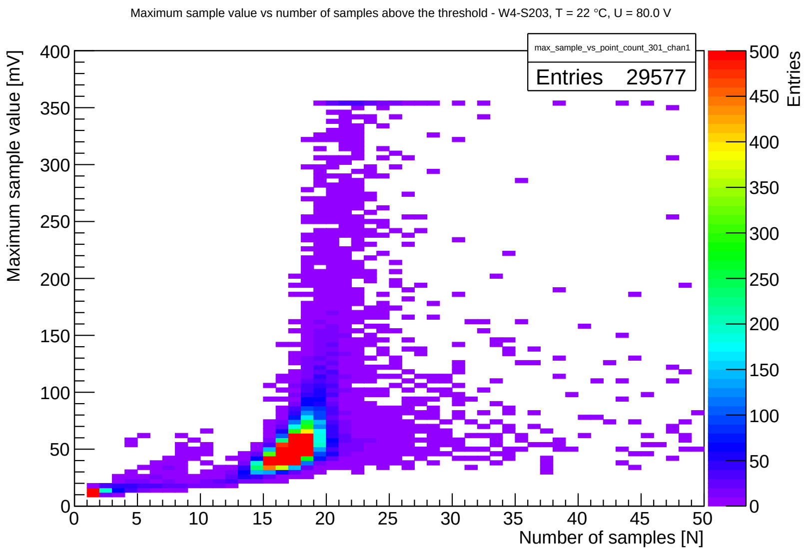

(c) Maximum sample value versus number of samples above U_S.

Figure 4.2: Distributions of the number of samples and maximum sample value above U_S with a plot showing the correlation between both quantities. Here the choice of $N_{\text{samples}} = 8$ is set for W4-S203 which is in between the area of the majority of the signals and noise. The averaged noise value at $U_b = 80\,\text{V}$ for W4-S203 is $2.4\,\text{mV}$.

needed. The total charge is obtained by calculating the integral of the pulse above the pedestal, divided by the resistance from the transimpedance amplifier. The gain is then obtained by dividing with the deposited charge within a sensor with same thickness for a minimum ionizing particle, which is $Q_{\mathrm{MIP}} = 0.46\,\mathrm{fC}$ [19].

4.1.3 Timing resolution

With the time location of the pulses, the timing resolution for a sensor can be calculated. This is done by taking the time difference for a signal from a LGAD and the SiPM within the same event. Collecting the time differences, a distribution is formed where the width is calculated. A cross-check method is used to calculate the timing resolution using a system of equations. Both methods are evaluated using the time location at the peak of the pulse, and with the CFD method.

Time difference between DUT and SiPM

The main method used to calculate the timing resolution is to take the time difference between a DUT and the SiPM, which is the reference sensor. From it, the total width σ_{Total} is obtained where the timing resolution of the DUT is expressed as

$$\sigma_{\mathrm{DUT}} = \sqrt{\sigma^2_{\mathrm{Total}} - \sigma^2_{\mathrm{SiPM}}}\,. \tag{4.2}$$

The value of σ_{SiPM} is taken from reference [24], where $\sigma_{\mathrm{SiPM}} \approx 18.4\,\mathrm{ps}$ for $T > 0\,°\mathrm{C}$ and $\sigma_{\mathrm{SiPM}} \approx 9.6\,\mathrm{ps}$ for $T < 0\,°\mathrm{C}$ at $U_b = 29\,\mathrm{V}$. During the test beam measurement in September 2017, the SiPM operates at $U_b = 26.5\,\mathrm{V}$, and it is assumed that this slight change in U_b does not significantly affect σ_{SiPM}. The timing resolution of the SiPM is much better than that of the DUTs, so a small change in σ_{SiPM} does not primarily affect the extracted value for σ_{DUT}.

System of equations

A cross-check to calculate the timing resolution by solving a system of equations is used. This is done by forming a time difference for the same event, between a combination of four connected sensors within the same oscilloscope. This gives six time differences, with six calculated widths, related to timing resolutions of LGADs i and j as $\sigma^2_{ij} = \sigma^2_i + \sigma^2_j$. A possible way to solve for σ_i and σ_j, is to introduce a system of equations by using one of 12 invertible matrices A_{ij},

$$\boldsymbol{\sigma}^2_{ij} = A_{ij} \cdot \boldsymbol{\sigma}^2, \tag{4.3}$$

where $\boldsymbol{\sigma}^2_{ij}$ is a four-dimensional vector with squared widths between sensor i and j, and $\boldsymbol{\sigma}^2$ is a vector with squared timing resolutions for the four sensors. Among the 12 matrices A_{ij} which solve (4.3), the one which give the solution with the largest sum of the timing resolutions is selected. The second oscilloscope is connected to array-pad sensors, where $\ll 1\%$ of all events have more than one signal from each pad. Because of this, the method is used only for the first oscilloscope, which have sufficient events with signals from all connected sensors.

4.2 Track-based analysis

Combining the sensor and tracking data, one can study the spatial dependence of measured signals in the DUTs. The tracking data for each sensor give relative position on the MIMOSA plane, which is centered to be at origin for each sensor. Additionally, the sensors are rotationally aligned around the beam line with a precision of $\pm 0.1\,°$. The bin size is set to be the same as for the MIMOSA pixel size, that is $18.4\,\mu m \times 18.4\,\mu m$. To extract a result from a bin, at least five entries are required. Bins showing the highest (red) or lowest (purple) value, means that the extracted bin value is higher or lower than given value on the color axis. An example of a 2D plot showing the sensor signal efficiency is presented in Figure 4.3a.

4.2.1 Uniformity over sensor area

For each type of the LGAD signal characteristics, a uniformity plot over the sensor area is made. For pulse amplitude, rise time and gain, each bin is filled and averaged. To show the timing resolution, each bin is filled with a time difference between the DUT and the SiPM with a bin size twice the MIMOSA pixel size. To extract a timing resolution value from a bin, at least 50 entries are required. The timing resolution is then calculated with (4.2). This is done using both the time location at the peak and with the CFD method.

4.2.2 Sensor efficiency

Using the information about a track from the MIMOSAs and a hit or no hit from the DUTs, the spatial efficiency of the sensor can be determined. Within each bin, the efficiency is defined as the ratio of the number of registered signals from the DUT N_{DUT} to the number of hits from the MIMOSA N_{MIMOSA},

$$N_{\text{efficiency}} = \frac{N_{\text{DUT}}}{N_{\text{MIMOSA}}}. \tag{4.4}$$

The N_{DUT} depends on a determined track from the MIMOSA. With the filled bins, an averaged value of the efficiency for a bulk area is determined with the standard deviation as the error. A bulk area is defined with ranges of $\pm 350\,\mu m$ in x and y with respect to the center of the sensor.

Projection on x- and y-axis

Using the 2D efficiency plots, projections on the x and y axes are made to find the efficiency steepness at the edges of the DUTs. The selection is $|y, x| \leq 350\,\mu m$ for the projection along the x and y axes, respectively. The selection areas can be seen in Figure 4.3a and Figure 4.3b. The projection along each axis is averaged over each dimension and a 1D histogram is formed. With this, two sigmoid-functions are fitted along the left and right edges,

$$S(u)_{\text{left}} = \frac{1}{1 + \exp{(u_{\text{left}} - u)/\sigma_{\text{left}}}}, \quad S(u)_{\text{right}} = \frac{1}{1 + \exp{(u - u_{\text{right}})/\sigma_{\text{right}}}}, \tag{4.5}$$

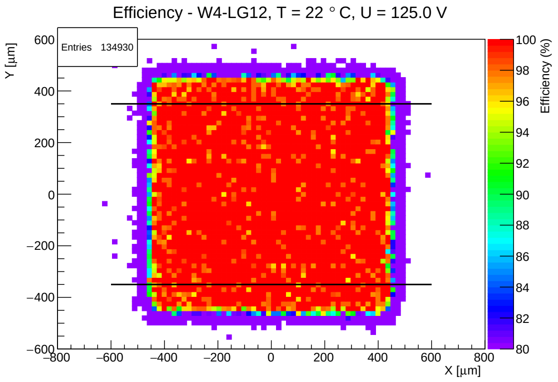

(a) Selection lines for projection on x-axis.

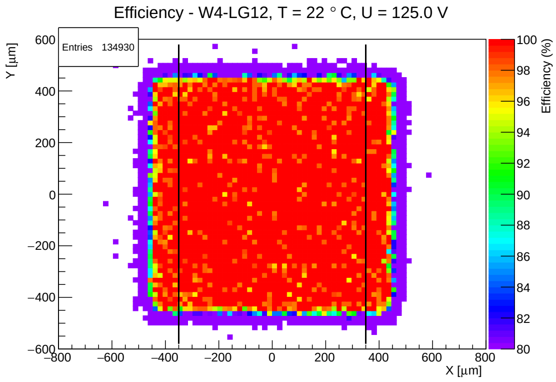

(b) Selection lines for projection on y-axis.

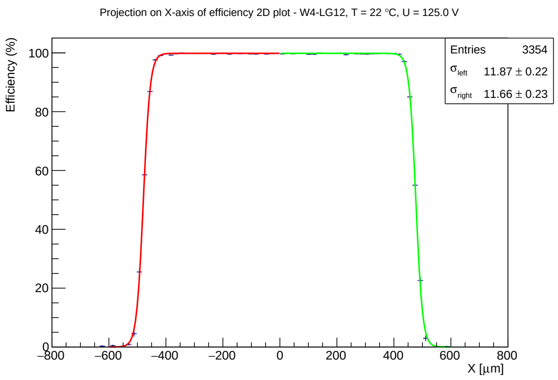

(c) Projection on x-axis with fit.

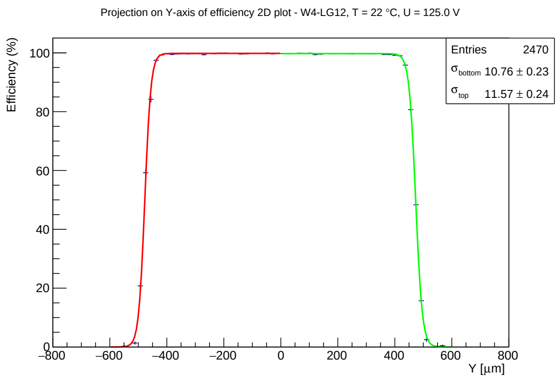

(d) Projection on y-axis with fit.

Figure 4.3: Selection lines and fit functions for projections on x and y axes. From this $\sigma_{\text{left, right}}$ and $\sigma_{\text{top, bottom}}$ are obtained for each side from the fit functions, corresponding to the steepness.

where u is the distance from the center of the sensor, u_{left} and u_{right} are the positions of the edges and $\sigma_{\text{left, right}}$ and $\sigma_{\text{top, bottom}}$, represent the steepnesses of the edges, measured in units of µm. This method of obtaining the steepness applies to sensors with square shape. Examples of histograms with fitted sigmoid-functions for both x- and y-projections can be seen in Figures 4.3c and 4.3d.

Chapter 5

Results

In this chapter the results extracted using the methods described in Chapter 4 are presented. First an overview of the results are shown and the selection is explained. In the sections after the methods of obtaining and choosing data are explained in more detail.

5.1 Overview of the results

Table 5.1 shows the timing resolution, the rise time, signal-to-noise (S/N) ratio and gain. The S/N ratio is defined as the pulse amplitude divided by the noise. For the array-pad sensors the pads selected for W4-RD01 and W4-S204 reflects the best achieved timing resolution and the selected pad for W4-S215 is the one which is measured for all temperatures. The selected pads are shown in Figures D.3, D.14 and D.16, respectively. The missing results for the timing resolution from the system of equations is because the pad was connected to the second oscilloscope. The bias voltage selected is maximum for each sensor and temperature to reflect the results which have the lowest timing resolution values. For the gain the lowest voltage is selected to show the lowest gain values, for which data were possible to obtain. In Table 5.2 the efficiency for the bulk area together with the steepness of the edges for both x- and y-projections is shown. The missing results for the steepness of the edges for the sensor 50D-GBGR2 is because the method applies only to square sensors. The batches of runs which have most data are chosen.

5.2 LGAD signal results

The noise and pedestal together with pulse characteristics are all collected into a histogram for each batch of runs. The data are fitted with a chosen function mentioned in the sections below, and the resulting parameters are listed with associated errors which are based on χ^2 method. When several batches exists with the same applied voltage and temperature, the one with the smallest error is chosen.

5.2.1 Noise and pulse characteristics

The noise values are fitted with a Gaussian function to obtain the mean value parameter. The error is $< 0.01\,\text{mV}$ for all values. The results depending on bias voltage and temperature are shown in Figure 5.3a.

Sensor	T [°C]	U_b [V]	$\sigma_{\text{CFD, SiPM}}$ [ps]	$\sigma_{\text{peak, SiPM}}$ [ps]	$\sigma_{\text{CFD, sys}}$ [ps]	$\sigma_{\text{peak, sys}}$ [ps]	t_{rise} [ps]	S/N	U_b [V]	Gain
50D-GBGR2	22	320	28.8 ± 0.3	35.8 ± 0.3	33.5 ± 0.6	37.3 ± 0.8	427 ± 0.3	47	220	14 ± 0.002
W4-LG12	22	125	24.9 ± 0.2	37.9 ± 0.4	31.7 ± 0.6	41.4 ± 0.8	543 ± 0.3	52	80	25 ± 0.04
W4-RD01	22	120	31.4 ± 0.1	68.7 ± 0.2	–	–	843 ± 0.1	71	80	204 ± 0.4
	−30	75	46.5 ± 0.3	127.1 ± 1.1	–	–	1088 ± 0.3	83	40	243 ± 0.4
W4-S1022	22	110	40.5 ± 0.9	51.5 ± 1.0	–	–	551 ± 0.6	20	80	18 ± 0.04
	−30	90	29.7 ± 0.3	39.2 ± 0.5	30.8 ± 0.4	41.5 ± 0.6	522 ± 0.2	50	50	25 ± 0.04
	−40	80	32.0 ± 0.2	43.0 ± 0.4	32.6 ± 0.6	43.3 ± 0.6	543 ± 0.1	48	50	29 ± 0.07
W4-S1061	22	150	24.0 ± 0.3	32.2 ± 0.5	–	–	494 ± 0.3	57	80	19 ± 0.04
	−30	90	32.0 ± 0.1	39.6 ± 0.2	32.1 ± 0.3	40.8 ± 0.8	534 ± 0.1	52	50	26 ± 0.04
	−40	80	33.7 ± 0.3	43.8 ± 0.4	33.4 ± 0.5	42.3 ± 0.6	553 ± 0.2	49	50	31 ± 0.07
W4-S203	22	120	27.2 ± 0.1	35.8 ± 0.5	–	–	525 ± 0.1	45	80	24 ± 0.04
	−30	70	39.0 ± 0.2	51.5 ± 0.3	41.4 ± 0.5	53.8 ± 0.5	623 ± 0.2	39	45	37 ± 0.04
	−40	60	46.0 ± 0.6	75.0 ± 0.6	48.2 ± 0.5	75.7 ± 0.6	696 ± 0.5	34	50	45 ± 0.07
W4-S204	−30	300	40.0 ± 0.3	50.0 ± 0.4	–	–	343 ± 1.5	10[a]	200	11 ± 0.02
	−40	270	39.1 ± 0.2	48.8 ± 0.3	–	–	338 ± 0.7	10	200	11 ± 0.03
W4-S215	22	125	31.5 ± 0.4	37.6 ± 0.5	–	–	505 ± 0.4	48	80	53 ± 0.1
	−30	80	35.5 ± 0.1	47.5 ± 0.3	35.5 ± 0.2	46.7 ± 0.4	546 ± 0.2	28	50	91 ± 0.2
	−40	65	47.7 ± 0.6	69.2 ± 0.5	48.0 ± 0.5	70.7 ± 1.1	657 ± 0.7	57	45	103 ± 0.2
W9-LGA35	22	250	24.3 ± 0.2	31.3 ± 0.3	32.2 ± 0.6	36.8 ± 0.8	417 ± 0.2	48	180	16 ± 0.03

Table 5.1: Results for timing resolution, rise time, S/N ratio and gain. The highest bias voltage U_b is selected for all results, except the last two columns, that is for gain where the lowest U_b is used for which data were possible to obtain. The relative error on all S/N values is less than 1%. The missing results showing the timing resolution using the system of equations is when the sensor is connected to a different oscilloscope than the SiPM.

[a]Pulse amplitude value is approximated where the fit on the histogram fails.

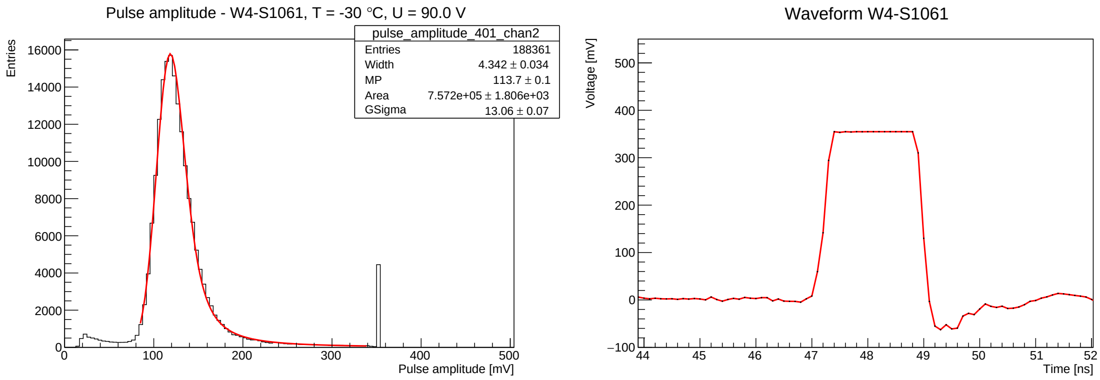

(a) Pulse amplitude distribution.

(b) Waveform with signal limit.

Figure 5.1: Pulse amplitude distribution for W4-S1061 at $T = -30\,°\mathrm{C}$ and $U_b = 90\,\mathrm{V}$. The distribution shows a peak for saturated signals and a waveform exhibiting this behavior.

The pulse amplitude and gain histograms are fitted with a convoluted Landau and Gauss function. This is because the deposited charge follows a Landau distribution and the noise a Gaussian one. From the fitted function, the most probable value is extracted. It was observed that for some sensors a fraction of the signals were saturated, since the oscilloscope had an upper voltage limit of recording signals. Figure 5.1 shows a pulse amplitude distribution with a fraction of events with saturated signals and a waveform exhibiting this behavior. The pulse amplitude values have an error which is $< 0.1\,\mathrm{mV}$. Using the noise results, the S/N ratio is obtained and shown in Table 5.1. Results which depend on other bias voltages and temperatures for pulse amplitude and gain values are in Figures 5.3b and 5.4a.

Rise time values are fitted with a Gaussian function, where the mean value parameter is extracted. The values with errors are shown in Table 5.1. The rise time results which depend on bias voltage and temperature are shown in Figure 5.4b.

5.2.2 Timing resolution

The results showing the timing resolution are presented in Table 5.1. Events with saturated signals are omitted when filling the histogram. For the time difference between the DUT and the SiPM placed in different oscilloscopes, the histogram changes as a second peak appear. An example of this can be seen in Figure 5.2. When the SiPM is in a different oscilloscope than the DUT, the fit function is modified with an added Gaussian term with mean value $\mu \to \mu + 100\,\mathrm{ps}$ using the same width parameter for both Gaussians. The reason for adding 100 ps is discussed in Section 6.2. The ranges for the fit on the histogram is set to be for the bins with number of entries greater than 20% of the maximum number of entries.

Figure 5.6 shows results for timing resolution as a function of gain for values $\sigma < 100\,\mathrm{ps}$ and with gain < 100. The aim with the plot is to see which sensor for a given temperature gives the lowest timing resolution and gain values.

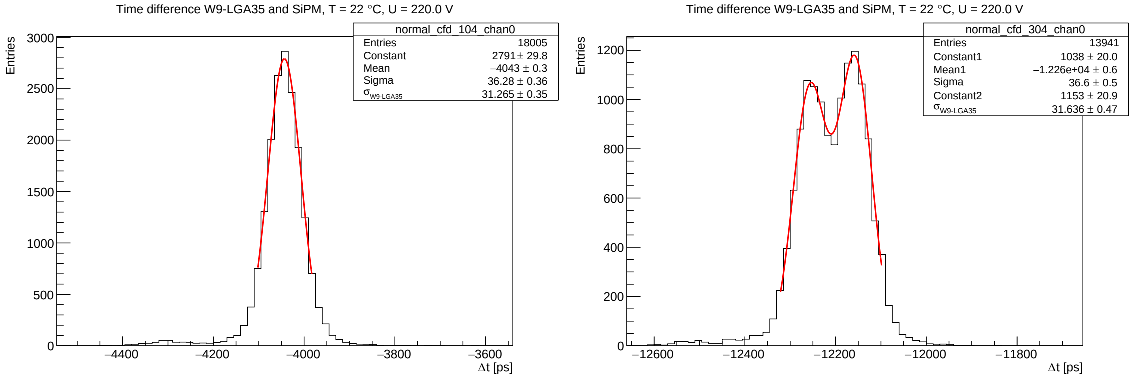

(a) Same oscilloscope.

(b) Different oscilloscopes.

Figure 5.2: Time difference distributions for W9-LGA35 sensor with 22 °C and $U_b = 220\,\text{V}$ when the DUT and the SiPM is in the same and different oscilloscopes. The correction has been made to include a second Gaussian with the mean value parameter increased with 100 ps.

5.3 Track-based results

The results showing efficiency of the bulk area with steepnesses of the edges of are presented in Table 5.2. The track-based plots showing the timing resolution are not shown for some sensors. The reason for this is because of a missing implementation in the software which fits the time difference distribution with a double-peak in each bin. This applies to sensors and pads being in a different oscilloscope than the SiPM. The sensors which have missing plots showing the timing resolution are W4-S1022, W4-S1061, W4-S203 and lower left pad for W4-S215. Plots with temperatures at $T = -40\,°\text{C}$ have bin size increased with 50% due to less available tracking data. Sensors with track-based plots showing the pulse amplitude, gain, rise time and timing resolution for different temperatures, are shown in Appendix D and the track-based plots for W9-LGA35 measured at $T = 22\,°\text{C}$ and $U_b = 230\,\text{V}$ are shown in Figure 5.7.

Sensor	T [°C]	U_b [V]	Efficiency [%]	$\sigma_{x,\text{ left}}$ [µm]	$\sigma_{x,\text{ right}}$ [µm]	$\sigma_{y,\text{ bottom}}$ [µm]	$\sigma_{y,\text{ top}}$ [µm]
50D-GBGR2	22	310	99.7 ± 0.8	–	–	–	–
W4-LG12	22	125	99.7 ± 0.8	11.9 ± 0.2	11.7 ± 0.2	10.8 ± 0.2	11.6 ± 0.2
W4-RD01	22	120	99.7 ± 0.8	10.7 ± 0.2	10.8 ± 0.2	10.3 ± 0.2	10.5 ± 0.2
	-30	60	99.1 ± 0.9	13.0 ± 0.2	13.5 ± 0.2	13.1 ± 0.2	12.4 ± 0.2
W4-S1022	22	90	99.5 ± 1.5	12.0 ± 0.3	12.4 ± 0.3	11.4 ± 0.3	12.0 ± 0.2
	-30	90	99.8 ± 1.1	11.9 ± 0.4	12.7 ± 0.4	10.3 ± 0.4	12.3 ± 0.4
	-40	80	99.8 ± 0.9	11.8 ± 0.6	13.0 ± 0.7	12.1 ± 0.6	12.3 ± 0.4
W4-S1061	22	140	99.8 ± 0.8	13.2 ± 0.3	11.9 ± 0.2	11.4 ± 0.2	13.4 ± 0.3
	-30	85	99.8 ± 0.9	12.2 ± 0.4	13.3 ± 0.4	11.0 ± 0.5	12.9 ± 0.4
	-40	80	99.8 ± 0.8	11.6 ± 0.5	12.5 ± 0.5	12.7 ± 0.7	13.8 ± 0.6
W4-S203	22	120	99.7 ± 0.7	16.7 ± 0.3	16.4 ± 0.2	13.8 ± 0.2	15.5 ± 0.3
	-30	60	99.6 ± 1.4	16.0 ± 0.5	14.8 ± 0.4	12.8 ± 0.4	15.5 ± 0.5
	-40	55	99.4 ± 1.5	15.3 ± 0.7	16.7 ± 0.7	15.0 ± 0.6	15.1 ± 0.5
W4-S204	-30	250	99.1 ± 1.8	12.7 ± 0.4	14.4 ± 0.5	9.8 ± 0.4	14.7 ± 0.4
	-40	250	99.5 ± 1.3	14.4 ± 0.7	13.8 ± 0.7	15.7 ± 0.5	14.7 ± 0.5
W4-S215	22	120	99.7 ± 0.8	12.7 ± 0.2	13.4 ± 0.2	11.8 ± 0.2	12.4 ± 0.3
	-30	80	99.8 ± 1.1	14.2 ± 0.3	14.3 ± 0.4	12.5 ± 0.4	13.8 ± 0.4
	-40	60	99.7 ± 1.0	14.9 ± 0.5	14.2 ± 0.6	13.7 ± 0.6	15.8 ± 0.6
W9-LGA35	22	230	99.7 ± 0.7	16.4 ± 0.3	16.5 ± 0.3	14.3 ± 0.2	14.4 ± 0.2

Table 5.2: Results for efficiency studies. The batch which has the most data is chosen when there are several available. The efficiency is quoted for the bulk area, along with steepness $\sigma_{\text{left, right}}$ and $\sigma_{\text{bottom, top}}$. For the array-pad sensors the pads selected for W4-RD01 and W4-S204 reflects the lowest timing resolution and the selected pad for W4-S215 is the one which is measured for all temperatures. The missing results showing the efficiency steepness over the edges is because of the circular shape of the sensor, for which the method does not apply.

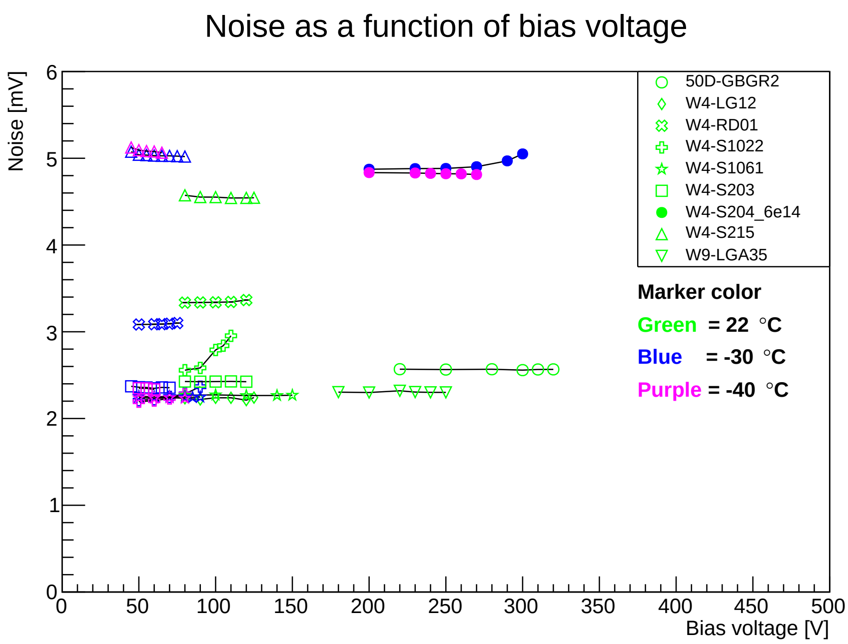

(a) Noise.

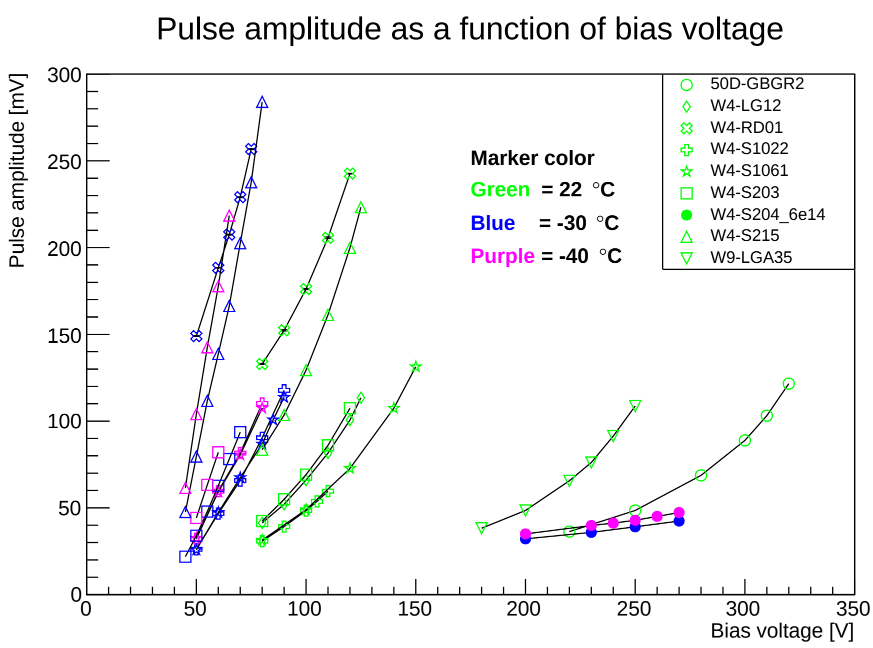

(b) Pulse amplitude.

Figure 5.3: Results for noise and pulse amplitude as a function of bias voltage.

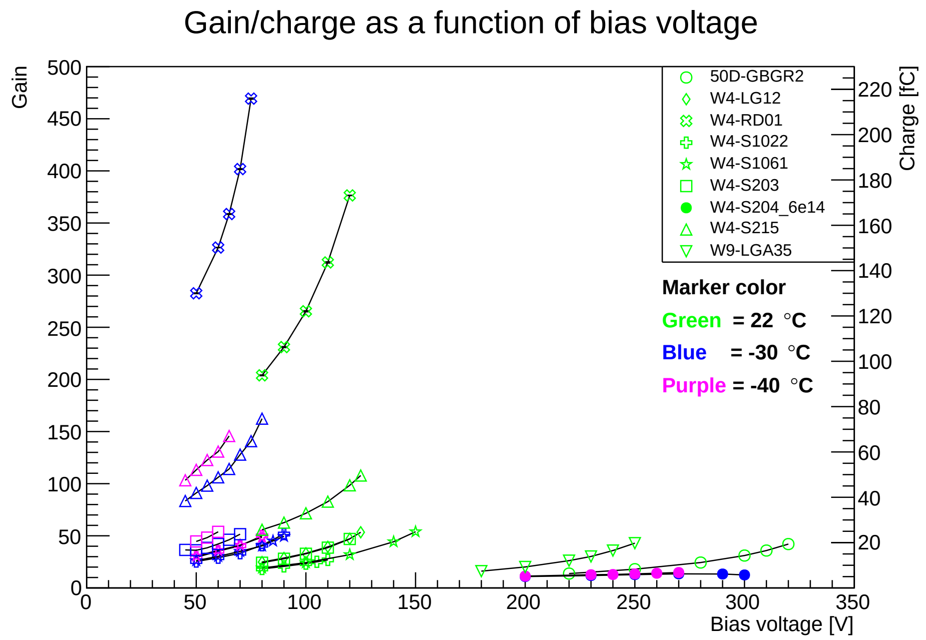

(a) Gain/charge results.

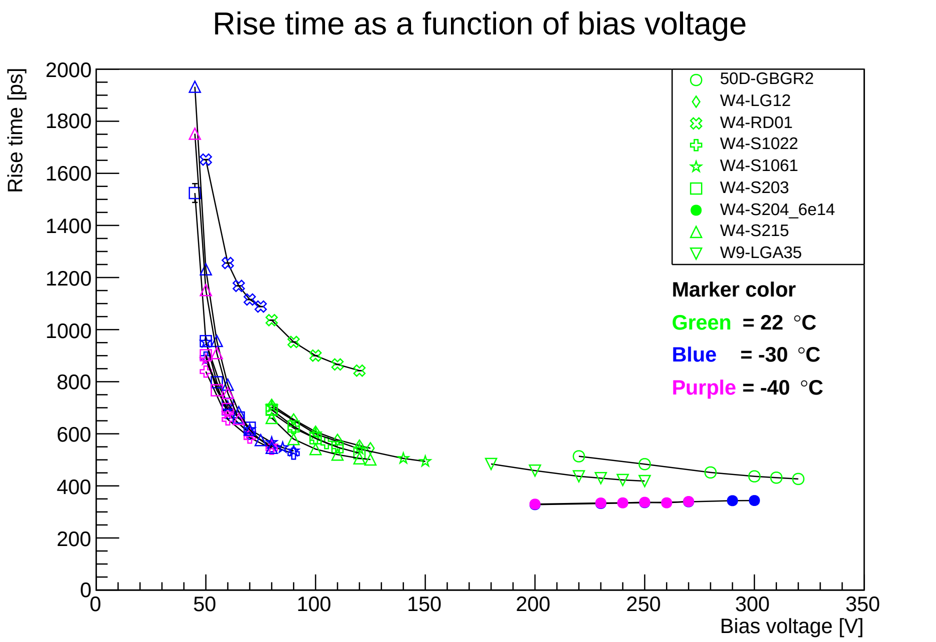

(b) Rise time results.

Figure 5.4: Results for rise time and gain/charge as a function of bias voltage.

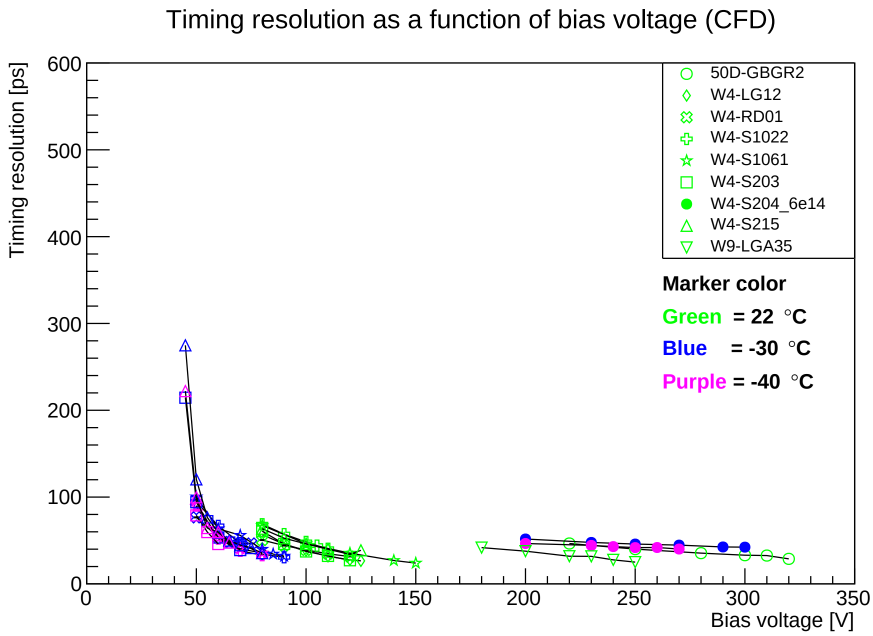

(a) Using CFD method.

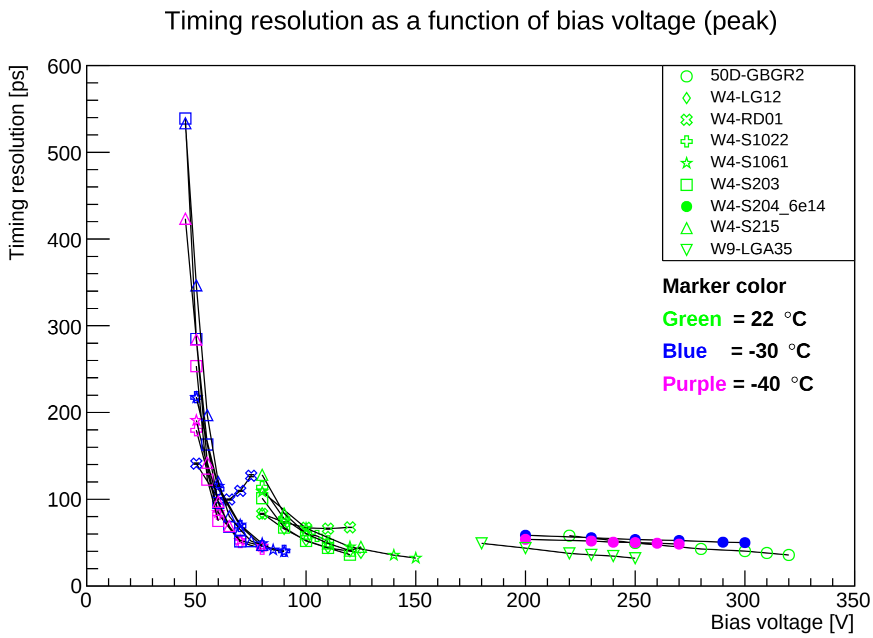

(b) Using location at the peak of pulse.

Figure 5.5: Results for timing resolution as a function of bias voltage and temperature using CFD method and location at peak of the pulse.

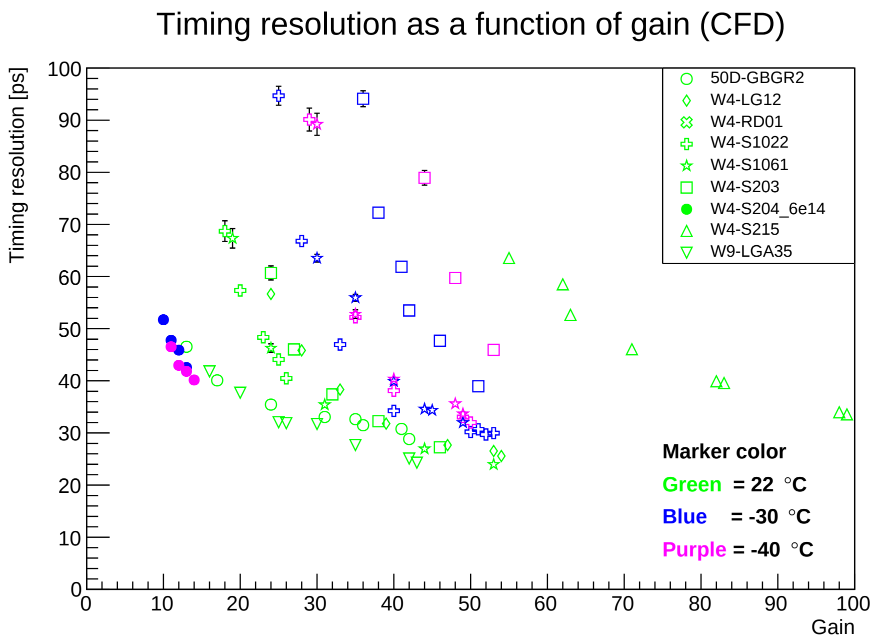

(a) Using the CFD method.

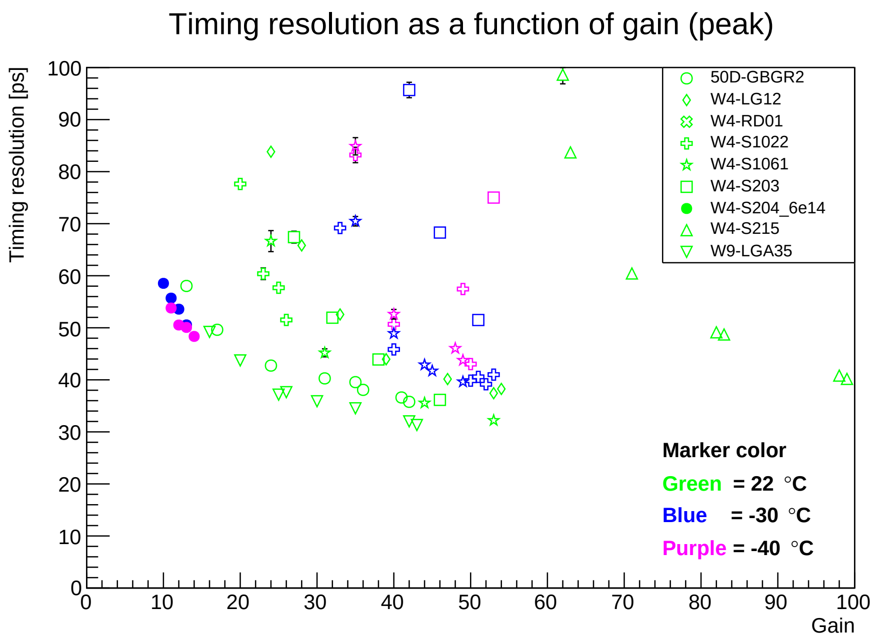

(b) Using location at peak of the pulse.

Figure 5.6: Results for timing resolution as a function of gain using CFD method and location at the peak of the pulse.

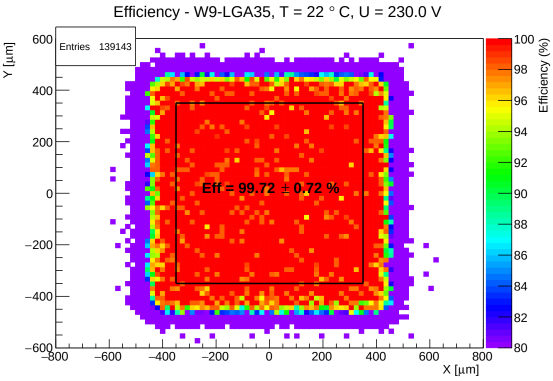

(a) Efficiency.

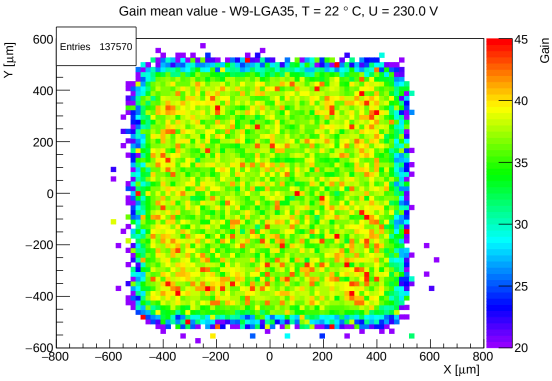

(b) Gain.

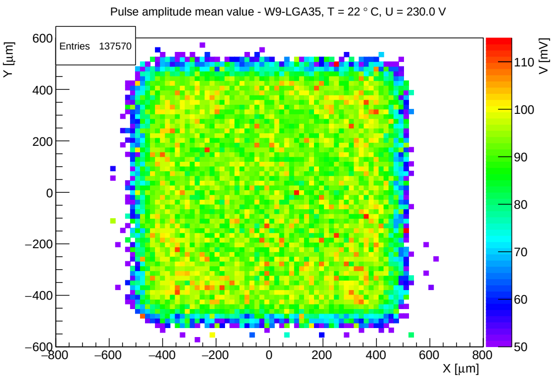

(c) Pulse amplitude.

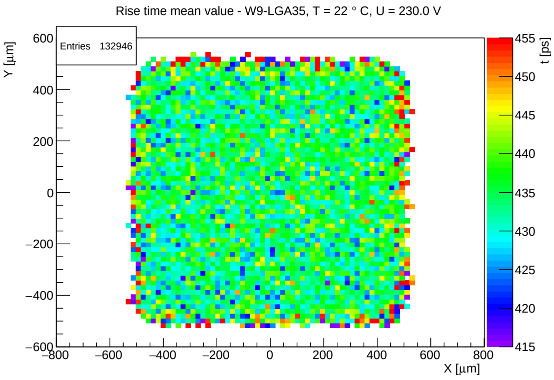

(d) Rise time.

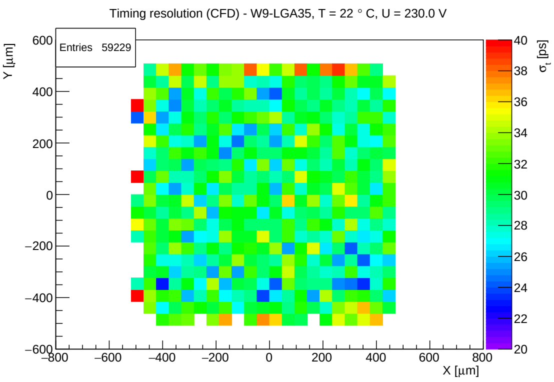

(e) Timing resolution - CFD method.

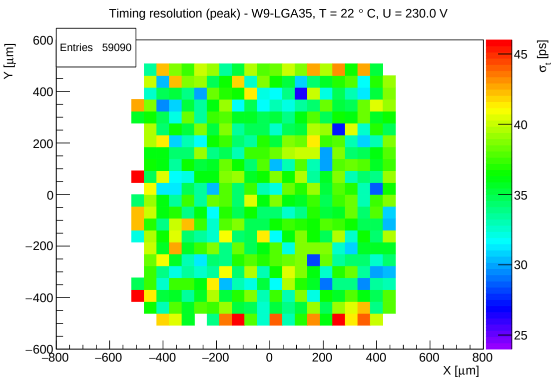

(f) Timing resolution - peak location method.

Figure 5.7: Track-based plots for W9-LGA35 at $T = 22\,°\mathrm{C}$.

Chapter 6

Discussion and conclusions

6.1 Signal characteristics

The noise tends to be independent of bias voltage and temperature with the exception of W4-S1061 and W4-S204. An increase of 0.5 mV for W4-S1061 and 0.1 mV for W4-S204 with increasing bias voltage is noticed in Figure 5.3a. This increase is small and does not affect the measurement of other signal characteristics. The noise of other sensors tends not to vary with bias voltage and is around 2 mV for the single-pad sensors and 5 mV for the array-pad ones, independent of temperature.

For all sensors a higher bias voltage leads to a larger pulse amplitude, which can be seen in Figure 5.3b. It can be seen that the increase is smaller for the irradiated sensor W4-S204. There are two missing pulse amplitude values for the irradiated sensor at $-30\,°\mathrm{C}$ with $U_b = 290\,\mathrm{V}$ and $U_b = 300\,\mathrm{V}$ for which the fit to the histogram fails. For these measurements, there are more events which are noise than true signals, which is related to the choice of N_{samples} which is lower than for other sensors. The same sensor has $S/N = 10$, where the others have ratio of $30 - 80$ with the highest for W4-RD01. The lower S/N ratio for W4-S204 is one reason where selection of a true signal is more difficult than for other sensors. The temperature dependence can be noticed, for W4-S215 at $T = -30\,°\mathrm{C}$ and $T = -40\,°\mathrm{C}$ for same bias voltages. One can notice an increase of 20% for the pulse amplitude compared to the lower temperature for W4-S215.

The gain results depending on bias voltage and temperature can be seen in Figure 5.4a. From it, one can observe the gain values for the W4-RD01 reach 500 with the smallest ones around 200. A possible reason could be that the resistance of the transimpedance amplifier in the readout board used is assumed to be the same as for other sensors, which may be incorrect. The gain values for other sensors are around $12 - 100$, seen in Table 5.1. The temperature dependence can be noticed for the sensor W4-S215 measured at $T = -30\,°\mathrm{C}$ and $T = -40\,°\mathrm{C}$, which follows approximately a 25% increase.

It can be seen from Figure 5.4b that the rise time decreases with bias voltage having lowest results around 500 ps except for the sensor W4-S204 which gives close to 350 ps. The same sensor gives a slight increase of rise time with increasing bias voltage. A possible cause for this, is the fewer number of samples for a signal compared to other sensors. Regarding temperature dependence, the rise time values for W4-RD01 tend to be independent of temperature. The curves for $T = -40\,°\mathrm{C}$ and $T = -30\,°\mathrm{C}$ seem to be connected and if the applied bias voltage would be the same, the curve could follow the same behavior. This can also be seen for sensors with $T = 22\,°\mathrm{C}$ for $80\,\mathrm{V} < U_b < 120\,\mathrm{V}$

where the values lies within the same region. On the other hand, the rise time results for W4-S215 at $U_b = 80\,\text{V}$ decreases for $T < 0\,^{\circ}\text{C}$.

6.2 Timing resolution

The timing resolution results in Table 5.1 show that the CFD method provides lower values which can also be noted by comparing Figures 5.5a and 5.5b. A cause of this is due to a typical pulse shape of a signal where the position of the rising edge is more stable than the of the peak of the pulse. Looking at multiple waveforms with the pulses super-positioned, the position of the rising edge is more stable when compared to the position at the peak of the pulse. An example showing different pulse shapes can be seen in Figure 6.1. The time location will deviate more when locating the peak of the pulse, leading to higher time difference values. For example, the sensor W4-RD01 for $T = -30\,^{\circ}\text{C}$ with $U_b = 60\,\text{V}$ give a timing resolution value of about 130 ps using location at the peak of the pulse, compared to around 47 ps using the CFD method. This is a consequence of the pulse shape deviating significantly. With this, the CFD method is more suitable to calculate the timing resolution compared to the location at the peak of the pulse. In this study, the CFD method uses a fraction of 0.5 of the pulse amplitude, where other fractions could be used. Based on Figure 6.1 choosing a fraction 0.2 could also be of interest to determine the timing resolution, with the location being more stable for 0.5.

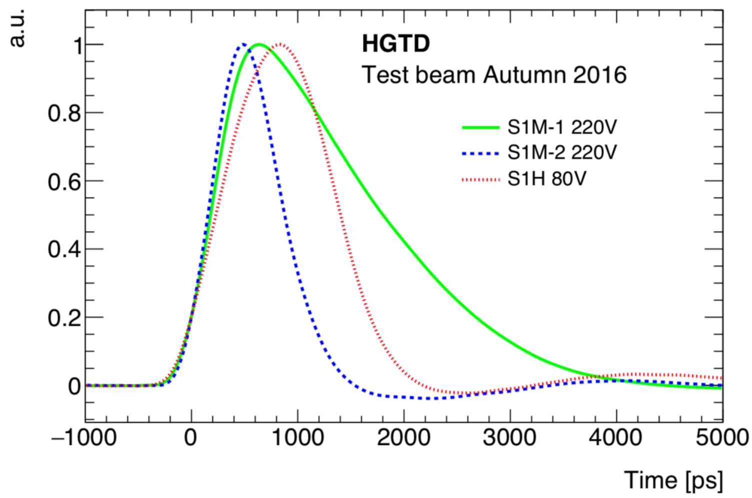

Figure 6.1: Pulse shape examples. Super-positioned pulse shapes for three sensors from the test beam measurement done in October/November 2016 [19].

In Figure 5.2 another behavior was noted where the time difference distribution has a double-peak structure. It can be seen that the time difference between those have a separation of 100 ps which can be observed clearly for some batches. For other batches the second peak is significantly smaller but still notable. This behavior is caused by shift with one data sample from one of the oscilloscopes. When these record samples from a triggered event, one of the oscilloscopes delays with one data sample compared to the other one. When comparing the same event from two different oscilloscopes, the time difference is shifted with $0.1\,\text{ns} = 100\,\text{ps}$ causing a second peak in the distribution.

The aim of using the system of equations method is to have a cross-check values to determine the credibility using the main method of calculating the timing resolution. Comparing the results using the CFD method, it can be seen that the values are generally larger. The largest difference seen is for W9-LGA35 with 7.9 ps.

To see which sensors have both low gain and good enough timing resolution, Figure 5.6 is shown. Comparing the two methods used to obtain the timing resolution, that is the CFD method and the location at the peak, it can be seen here as well that the values are lower using the CFD method. Additionally, one can be observe that the sensors W9-LGA35 and 50D-GBGR2 measured at $T = 22\,°\mathrm{C}$ have the lowest gain and timing resolution values. The temperature dependence can be noted, as the ones with lower temperatures give worse timing resolution and higher gain values, with the exception of the irradiated sensor W4-S204.

6.3 Track-based results

The track-based results show how the signal characteristics vary over the surface of the sensor. One of the aspects is the efficiency of the sensor, and from Table 5.2 it can be seen that it reaches $> 99\%$ in the bulk, independent of temperature, which can be seen in Figure 5.7a. The efficiency steepness of the edges shown in Table 5.2, show that the values are in the range $9 - 17\,\mu\mathrm{m}$ with the exception of 50D-GBGR2 which is round and cannot be compared to other sensors with square shape. For W4-S203 one can observe a small area with lower efficiency, for example in Figure 6.2a. A possible explanation for it could be a faulty area on the sensor giving an overall lower efficiency. For some of the sensors there is an observed line with unfilled bins, seen in Figure 6.2b. The reason for this that one of the MIMOSA planes were broken, which caused a distinct line with missing data from the telescope.

The track-based plots showing the gain and pulse amplitude in Figures 5.7b and 5.7c tend to be uniform for all sensors, with the exception at the edges. It can be seen for some sensors, that plots showing the rise time are not uniform. Most of the sensors look like the one for W9-LGA35, shown in Figure 5.7d. Sensors W4-LG12 and W4-RD01 show deviating features which can be seen in Figures 6.2d and 6.2c. It can be noted that an area has lower rise time values compared to the rest of the sensor. The area is significantly larger for the upper pad of W4-RD01 compared to W4-LG12. The track-based timing resolution plots show that the values are fairly uniform. The view for other sensors looks like the one for W9-LGA35, shown in Figures 5.7e and 5.7f.

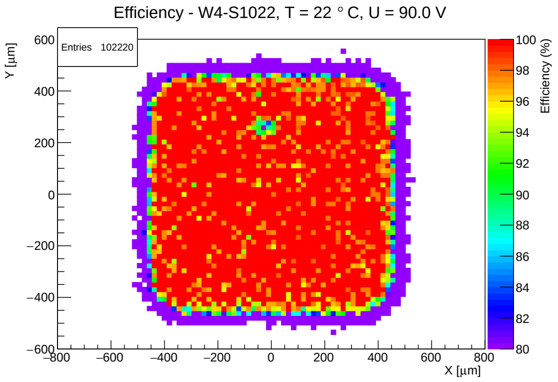

(a) Dot with lower efficiency - W4-S1022.

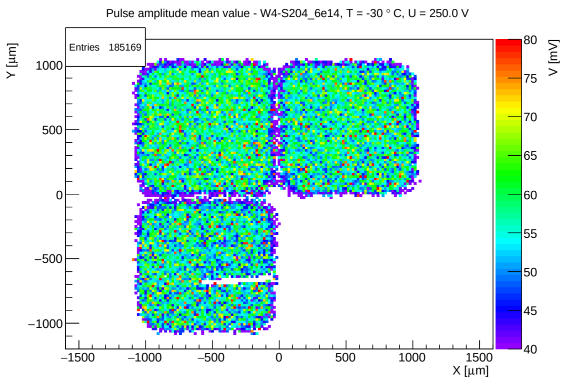

(b) Line with missing data.

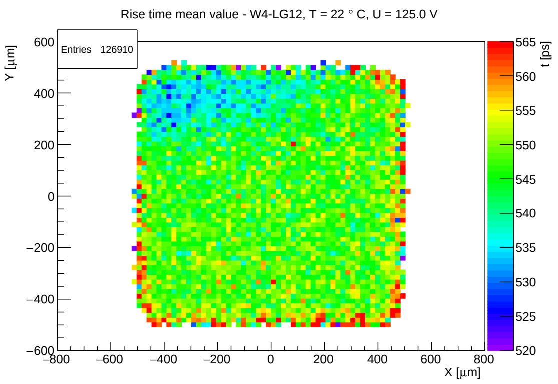

(c) Non-uniform rise time view - W4-LG12.

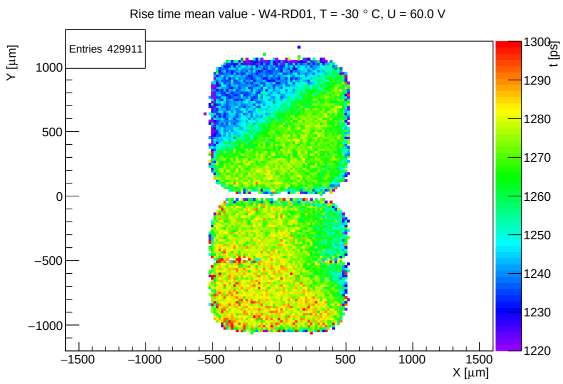

(d) Non-uniform rise time view - W4-RD01.

Figure 6.2: Track-based plots with interesting features. The first plot has a dot with lower efficiency for W4-S1022, the second one shows a line with missing data for W4-S204, and the last two show non-uniform behavior of the rise time values for W4-LG12 and W4-RD01.

6.4 Conclusions

The sensors which fulfill the requirements with a timing resolution of ≤ 42 ps/hit and gain < 30 with a square structure are: **W4-LG12, W4-S1022, W4-S1061** and **W9-LGA35**. The circular pad sensor **50D-GBGR2** also fulfills the requirements. The W4-RD01 sensor is the slowest one with rise times reaching > 800 ps with rise time values having a non-uniform view over the sensor. W4-S203 fulfill the requirements for $T > -40\,°\text{C}$. The irradiated sensor W4-S204 has the lowest S/N ratio with lower rise time than other sensors due to fewer data samples over the threshold U_S. The array-pad sensor W4-S215 have a higher gain and higher noise, compared to single-pad sensors. The temperature dependence is seen giving better timing resolution and gain values for $T > 0\,°\text{C}$. The efficiency in the bulk and the efficiency steepness are temperature independent. The preferred method of obtaining the location of the pulse is the CFD method. Calculating the timing resolution with the SiPM connected to a different oscilloscope gives similar results to the ones within the same one. A suggestion is to use one SiPM in each oscilloscope to avoid the problem of desynchronized readout. All pads have an efficiency of $> 99\%$ and all square pad sensors have an edge steepness $< 17\,\mu\text{m}$.

Chapter 7

Outlook

This test beam measurement together with others done in April, June, September and October in 2018 allow more sensors to be evaluated. The test beam measurement done in September 2017 had only one irradiated sensor which is fewer than at previous measurement campaigns. Test beam campaigns already conducted included more irradiated sensors to understand how those perform in the HGTD after years of operation. Therefore a broader comparison of irradiated with non-irradiated sensors is underway.

Different sensor types are considered to be measured. Proposed ones with a thickness of 35 µm have been shown to give a better timing resolution and less radiation damage. Additionally, different gain doping dose layers are considered to optimize the gain value.

Since the timing resolution of the sensors is of primary interest, an aim is to have a comparison of different methods to obtain a value with low uncertainty. One should evaluate alternative ways to obtain the time location. In this study, the CFD fraction 0.5 has been used only, but this should be optimized. There are other options, such as the zero-crossing discriminator, which is the location when the waveform passes a set threshold.

The R&D of prototype sensors for the HGTD is planned to continue until the end of 2020 with production during 2022-2023. Furthermore the electronics in the HGTD which connects the sensors, need to be designed in such way to maintain the timing resolution requirements of a measured track. The plan is to produce the electronics during 2023, install the HGTD along with auxiliary systems of the detector in ATLAS during 2025-2026. With the HGTD together with the other sub-detector systems in ATLAS there will be a better foundation to search for rare processes and make better use of the proton-proton data. This helps to increase the precision measurements of the SM and improve the sensitivity of searches for physics beyond the SM.

Chapter 8

Acknowledgments

I would like to express my gratitude to my supervisor Christian Ohm, who have been guiding me through this project and continuously providing support for me during my hard times. Your ability to search for the most easy solution (not the most complicated I usually chose) helped me out with many of my problems. Your positive attitude and patience influenced me positively. Thanks for your useful feedback on the report which help be deepen my understanding of physics. Thank you, Dr. Ω!

I want to thank the ATLAS group at KTH for the opportunity to work with you. It was a pleasure to get an understanding of how it is to work with particle physics in an experimental way. Thank you for giving me an opportunity to visit CERN which gave me insights to an interesting world.

Big thanks to Alex Kastanas for giving me feedback on the thesis report as well as solving some issues with the software package. Your support and discussions with you have been uplifting for me!

It was a pleasure to be a part of the Particle and Astroparticle group at KTH and take part of interesting discussions.

I would also thank the SU physics department for allowing me having an office spot. Also, a thanks to the PhD students at SU for interesting discussions, I wish you all the best with your studies!

A special thanks to Karol Wojtulewicz for providing useful feedback on the report and helping me out with my struggles. Thanks mate!

Finally, I would like to thank my family and friends for giving me moral support throughout this project.

List of Figures

List of Tables

Appendix A

Road-map of the HL-LHC

The schedule of the HL-LHC is shown in Figure A.1. One can see the time line of Run 1-5 with the collision energy and the total recorded integrated luminosity. The figure also shows when the HL-LHC is scheduled to operate, that is after Long Shutdown 3 (LS3) which is planned to be during 2024-2026.

Figure A.1: Schedule overview of the HL-LHC. The figure shows the projected integrated luminosity [4].

Appendix B

Run log

The run log, shown in Tables B.1 and B.2, lists information for tested sensors during the measurement in September 2017 in the North Area at CERN. Each row shows information about the run which is part of a batch with events recorded, averaged rate of recording the data, temperature, DUT position (useful for array-pad sensors), applied bias voltages and measured currents. Columns in red and blue represent two different oscilloscopes, each with four channels connected to sensors. Each run has an oscilloscope file with voltage information, and a corresponding tracking file with positions of tracks on the sensor.

Yellow marked runs show a warning with the run, with a common reason being that some events are desynchronized between the oscilloscope and the telescope. Red marked runs mean that the files have been deleted due to problems with the measurement.

Batches 801-804 and 901-903 are omitted from the analysis in this thesis. Batches 801-804 contain low data statistics for the sensors W9-LGA44 and W4-S1030, and batches 901-903 is for a measurement of three SiPMs from another manufacturer than the one used for this thesis.

EUDAQ	Scope		#Events	Av.	T set	1-1				1-2				1-3				1-4				2-1				2-2				2-3				2-4			
RunNumber	Timestamp	Batch	This run	Rate [Hz]	T [C]	DUT Pos.	Sensor	V[V]	I [µA]	DUT Pos.	Sensor	V[V]	I [µA]	DUT Pos.	Sensor	V[V]	I [µA]	DUT Pos.	Sensor	V[V]	I [µA]	DUT Pos.	Sensor	V[V]	I [µA]	DUT Pos.	Sensor	V[V]	I [µA]	DUT Pos.	Sensor	V[V]	I [µA]	DUT Pos.	Sensor	V[V]	I [µA]
3656	1504818689	101	200262	285	22	1	W9-LGA35	250	0,005	4	50D-GBGR2	300	0,002	6	W4-LG12	120	0,003	SiPM-AFP	SiPM-AFP	26,5	35,5	3_0	W4-S215	125	0,007	3_1	W4-S215	125	0,007	3_2	W4-S215	125	0,007	3_3	W4-S215	125	0,007
3657	1504820576	101	279007	288	22	1	W9-LGA35	250	0,005	4	50D-GBGR2	300	0,002	6	W4-LG12	120	0,003	SiPM-AFP	SiPM-AFP	26,5	35,5	3_0	W4-S215	125	0,007	3_1	W4-S215	125	0,007	3_2	W4-S215	125	0,007	3_3	W4-S215	125	0,007
3658	1504821761	101	200288	288	22	1	W9-LGA35	250	0,005	4	50D-GBGR2	300	0,002	6	W4-LG12	120	0,003	SiPM-AFP	SiPM-AFP	26,5	35,5	3_0	W4-S215	125	0,007	3_1	W4-S215	125	0,007	3_2	W4-S215	125	0,007	3_3	W4-S215	125	0,007
3659	1504822722	101	200236	285	22	1	W9-LGA35	250	0,005	4	50D-GBGR2	300	0,002	6	W4-LG12	120	0,003	SiPM-AFP	SiPM-AFP	26,5	36	3_0	W4-S215	125	0,007	3_1	W4-S215	125	0,007	3_2	W4-S215	125	0,007	3_3	W4-S215	125	0,007
3660	1504823703	101	200291	290	22	1	W9-LGA35	250	0,005	4	50D-GBGR2	300	0,002	6	W4-LG12	120	0,003	SiPM-AFP	SiPM-AFP	26,5	36	3_0	W4-S215	125	0,007	3_1	W4-S215	125	0,007	3_2	W4-S215	125	0,007	3_3	W4-S215	125	0,007
3661	1504826378	102	200215	180	22	1	W9-LGA35	180	0,0034	4	50D-GBGR2	220	0,0017	6	W4-LG12	80	0,0025	SiPM-AFP	SiPM-AFP	26,5	36	3_0	W4-S215	80	0,005	3_1	W4-S215	80	0,005	3_2	W4-S215	80	0,005	3_3	W4-S215	80	0,005
3662	1504827818	103	207667	180	22	1	W9-LGA35	200	0,0035	4	50D-GBGR2	250	0,0017	6	W4-LG12	90	0,0025	SiPM-AFP	SiPM-AFP	26,5	36	3_0	W4-S215	90	0,005	3_1	W4-S215	90	0,005	3_2	W4-S215	90	0,005	3_3	W4-S215	90	0,005
3663	1504829144	104	200284	178	22	1	W9-LGA35	220	0,0036	4	50D-GBGR2	280	0,0018	6	W4-LG12	100	0,0026	SiPM-AFP	SiPM-AFP	26,5	36	3_0	W4-S215	100	0,005	3_1	W4-S215	100	0,005	3_2	W4-S215	100	0,005	3_3	W4-S215	100	0,005
3664	1504830539	105	200239	232	22	1	W9-LGA35	230	0,0037	4	50D-GBGR2	300	0,0019	6	W4-LG12	110	0,0026	SiPM-AFP	SiPM-AFP	26,5	37	3_0	W4-S215	110	0,006	3_1	W4-S215	110	0,006	3_2	W4-S215	110	0,006	3_3	W4-S215	110	0,006
3665	1504831602	106	210892	398	22	1	W9-LGA35	240	0,0039	4	50D-GBGR2	310	0,0019	6	W4-LG12	120	0,0028	SiPM-AFP	SiPM-AFP	26,5	37	3_0	W4-S215	120	0,006	3_1	W4-S215	120	0,006	3_2	W4-S215	120	0,006	3_3	W4-S215	120	0,006
3666	1504832421	107	207375	377	22	1	W9-LGA35	250	0,0044	4	50D-GBGR2	320	0,002	6	W4-LG12	125	0,0031	SiPM-AFP	SiPM-AFP	26,5	37	3_0	W4-S215	125	0,006	3_1	W4-S215	125	0,006	3_2	W4-S215	125	0,006	3_3	W4-S215	125	0,006
3667	1504833164	108	207418	404	22	1	W9-LGA35	230	0,0037	4	50D-GBGR2	310	0,0019	6	W4-LG12	125	0,0031	SiPM-AFP	SiPM-AFP	26,5	37	3_0	W4-S215	120	0,006	3_1	W4-S215	120	0,006	3_2	W4-S215	120	0,006	3_3	W4-S215	120	0,006
3668	1504833898	108	207352	405	22	1	W9-LGA35	230	0,0037	4	50D-GBGR2	310	0,0019	6	W4-LG12	125	0,0031	SiPM-AFP	SiPM-AFP	26,5	37	3_0	W4-S215	120	0,006	3_1	W4-S215	120	0,006	3_2	W4-S215	120	0,006	3_3	W4-S215	120	0,006
3669	1504834599	108	214579	403	22	1	W9-LGA35	230	0,0037	4	50D-GBGR2	310	0,0019	6	W4-LG12	125	0,0031	SiPM-AFP	SiPM-AFP	26,5	37	3_0	W4-S215	120	0,006	3_1	W4-S215	120	0,006	3_2	W4-S215	120	0,006	3_3	W4-S215	120	0,006
3670	1504835228	108	214495	406	22	1	W9-LGA35	230	0,0037	4	50D-GBGR2	310	0,0019	6	W4-LG12	125	0,0031	SiPM-AFP	SiPM-AFP	26,5	38	3_0	W4-S215	120	0,006	3_1	W4-S215	120	0,006	3_2	W4-S215	120	0,006	3_3	W4-S215	120	0,006
3671	1504836010	108	207362	389	22	1	W9-LGA35	230	0,0037	4	50D-GBGR2	310	0,0019	6	W4-LG12	125	0,0031	SiPM-AFP	SiPM-AFP	26,5	38	3_0	W4-S215	120	0,006	3_1	W4-S215	120	0,006	3_2	W4-S215	120	0,006	3_3	W4-S215	120	0,006
3691	1504853409	201	413477	378	22	1	W9-LGA35	180	0,003	4	50D-GBGR2	220	0,0016	6	W4-LG12	80	0,0024	3_0	W4-S215	80	0,004	SiPM-AFP	SiPM-AFP	26,5	38	3_1	W4-S215	80	0,004	3_2	W4-S215	80	0,004	3_3	W4-S215	80	0,004
3693	1504854923	202	203231	400	22	1	W9-LGA35	200	0,0032	4	50D-GBGR2	250	0,0017	6	W4-LG12	90	0,0025	3_0	W4-S215	90	0,005	SiPM-AFP	SiPM-AFP	26,5	38	3_1	W4-S215	90	0,005	3_2	W4-S215	90	0,005	3_3	W4-S215	90	0,005
3697	1504863572	203	100000	400	22	1	W9-LGA35	220	0,0035	4	50D-GBGR2	280	0,0018	6	W4-LG12	100	0,0026	3_0	W4-S215	100	0,005	SiPM-AFP	SiPM-AFP	26,5	38	3_1	W4-S215	100	0,005	3_2	W4-S215	100	0,005	3_3	W4-S215	100	0,005
3698	1504864077	203	60000	400	22	1	W9-LGA35	220	0,0035	4	50D-GBGR2	280	0,0018	6	W4-LG12	100	0,0026	3_0	W4-S215	100	0,005	SiPM-AFP	SiPM-AFP	26,5	38	3_1	W4-S215	100	0,005	3_2	W4-S215	100	0,005	3_3	W4-S215	100	0,005
3701	1504865427	203	80000	286	22	1	W9-LGA35	220	0,0035	4	50D-GBGR2	280	0,0018	6	W4-LG12	100	0,0026	3_0	W4-S215	100	0,005	SiPM-AFP	SiPM-AFP	26,5	38	3_1	W4-S215	100		3_2	W4-S215	100		3_3	W4-S215	100	
3738	1504884843	203	21503	102	22	1	W9-LGA35	220	0,0035	4	50D-GBGR2	280	0,0018	6	W4-LG12	100	0,0026	3_0	W4-S215	100	0,005	SiPM-AFP	SiPM-AFP	26,5	38	3_1	W4-S215	100		3_2	W4-S215	100		3_3	W4-S215	100	
3739	1504885418	203	200210	82	22	1	W9-LGA35	220	0,0035	4	50D-GBGR2	280	0,0018	6	W4-LG12	100	0,0026	3_0	W4-S215	100	0,005	SiPM-AFP	SiPM-AFP	26,5	38	3_1	W4-S215	100		3_2	W4-S215	100		3_3	W4-S215	100	
3740	1504888768	204	207463	177	22	1	W9-LGA35	230	0,0036	4	50D-GBGR2	300	0,002	6	W4-LG12	110	0,0027	3_0	W4-S215	110	0,006	SiPM-AFP	SiPM-AFP	26,5	41	3_1	W4-S215	110		3_2	W4-S215	110		3_3	W4-S215	110	
3741	1504890115	205	200299	250	22	1	W9-LGA35	240	0,0039	4	50D-GBGR2	310	0,0021	6	W4-LG12	120	0,003	3_0	W4-S215	120	0,007	SiPM-AFP	SiPM-AFP	26,5	41	3_1	W4-S215	120		3_2	W4-S215	120		3_3	W4-S215	120	
3742	1504891111	206	200500	290	22	1	W9-LGA35	250	0,0044	4	50D-GBGR2	320	0,0022	6	W4-LG12	125	0,0033	3_0	W4-S215	125	0,008	SiPM-AFP	SiPM-AFP	26,5	41,5	3_1	W4-S215	125		3_2	W4-S215	125		3_3	W4-S215	125	
3743	1504891913	207	312655	952	22	1	W9-LGA35	230	0,0037	4	50D-GBGR2	310	0,0021	6	W4-LG12	125	0,0032	3_0	W4-S215	120	0,007	SiPM-AFP	SiPM-AFP	26,5	41,4	3_1	W4-S215	120		3_2	W4-S215	120		3_3	W4-S215	120	
3745	1504893255	207	312570	284	22	1	W9-LGA35	230	0,0037	4	50D-GBGR2	310	0,0021	6	W4-LG12	125	0,0032	3_0	W4-S215	120	0,007	SiPM-AFP	SiPM-AFP	26,5	41,4	3_1	W4-S215	120		3_2	W4-S215	120		3_3	W4-S215	120	
3747	1504894541	207	250588	285	22	1	W9-LGA35	230	0,0037	4	50D-GBGR2	310	0,002	6	W4-LG12	125	0,0033	3_0	W4-S215	120	0,008	SiPM-AFP	SiPM-AFP	26,5	41,5	3_1	W4-S215	120		3_2	W4-S215	120		3_3	W4-S215	120	
3748	1504895590	207	200499	288	22	1	W9-LGA35	230	0,0037	4	50D-GBGR2	310	0,002	6	W4-LG12	125	0,0033	3_0	W4-S215	120	0,007	SiPM-AFP	SiPM-AFP	26,5	41,7	3_1	W4-S215	120		3_2	W4-S215	120		3_3	W4-S215	120	
3749	1504896394	207	208610	247	22	1	W9-LGA35	230	0,0037	4	50D-GBGR2	310	0,002	6	W4-LG12	125	0,0033	3_0	W4-S215	120	0,006	SiPM-AFP	SiPM-AFP	26,5	41,3	3_1	W4-S215	120		3_2	W4-S215	120		3_3	W4-S215	120	
3750	1504897360	207	214657	178	22	1	W9-LGA35	230	0,0037	4	50D-GBGR2	310	0,002	6	W4-LG12	125	0,0033	3_0	W4-S215	120	0,006	SiPM-AFP	SiPM-AFP	26,5	41,3	3_1	W4-S215	120		3_2	W4-S215	120		3_3	W4-S215	120	
3751	1504899897	207	200480	178	22	1	W9-LGA35	230	0,0037	4	50D-GBGR2	310	0,002	6	W4-LG12	125	0,0033	3_0	W4-S215	120	0,006	SiPM-AFP	SiPM-AFP	26,5	42	3_1	W4-S215	120		3_2	W4-S215	120		3_3	W4-S215	120	
3752	1504901141	207	221867	178	22	1	W9-LGA35	230	0,0038	4	50D-GBGR2	310	0,002	6	W4-LG12	125	0,0033	3_0	W4-S215	120	0,007	SiPM-AFP	SiPM-AFP	26,5	42,3	3_1	W4-S215	120		3_2	W4-S215	120		3_3	W4-S215	120	
3753	1504902956	207	200351	178	22	1	W9-LGA35	230	0,0038	4	50D-GBGR2	310	0,002	6	W4-LG12	125	0,0033	3_0	W4-S215	120	0,007	SiPM-AFP	SiPM-AFP	26,5	42	3_1	W4-S215	120		3_2	W4-S215	120		3_3	W4-S215	120	
3754	1504903764	207	200406	291	22	1	W9-LGA35	230	0,0038	4	50D-GBGR2	310	0,002	6	W4-LG12	125	0,0033	3_0	W4-S215	120	0,007	SiPM-AFP	SiPM-AFP	26,5	42	3_1	W4-S215	120		3_2	W4-S215	120		3_3	W4-S215	120	
3755	1504904519	207	200459	162	22	1	W9-LGA35	230	0,0038	4	50D-GBGR2	310	0,002	6	W4-LG12	125	0,0033	3_0	W4-S215	120	0,007	SiPM-AFP	SiPM-AFP	26,5	42	3_1	W4-S215	120		3_2	W4-S215	120		3_3	W4-S215	120	
3785	1504944107	301	100010	295	22	1	W9-LGA35	220	0,0035	2	W4-S203	80	0,004	5	W4-S1061	80	0,0025	6	W4-S1022	80	1,14	8_1	W4-RD01	80	0,0135	8_2	W4-RD01	80		x	x	x		SiPM-AFP	SiPM-AFP	26,5	42
3786	1504945362	301	206899	286	22	1	W9-LGA35	220	0,0035	2	W4-S203	80	0,004	5	W4-S1061	80	0,0025	6	W4-S1022	80	1,14	8_1	W4-RD01	80	0,0135	8_2	W4-RD01	80		x	x	x		SiPM-AFP	SiPM-AFP	26,5	42
3787	1504946329	302	207137	286	22	1	W9-LGA35	220	0,0035	2	W4-S203	90	0,004	5	W4-S1061	100	0,0028	6	W4-S1022	90	1,23	8_1	W4-RD01	90	0,0146	8_2	W4-RD01	90		x	x	x		SiPM-AFP	SiPM-AFP	26,5	42
3788	1504947269	303	206871	286	22	1	W9-LGA35	220	0,0035	2	W4-S203	100	0,005	5	W4-S1061	120	0,0034	6	W4-S1022	100	1,34	8_1	W4-RD01	100	0,0159	8_2	W4-RD01	100		x	x	x		SiPM-AFP	SiPM-AFP	26,5	42
3789	1504948123	304	214125	286	22	1	W9-LGA35	220	0,0035	2	W4-S203	110	0,005	5	W4-S1061	140	0,0048	6	W4-S1022	110	1,49	8_1	W4-RD01	110	0,018	8_2	W4-RD01	110		x	x	x		SiPM-AFP	SiPM-AFP	26,5	42
3790	1504949018	305	207003	289	22	1	W9-LGA35	220	0,0035	2	W4-S203	120	0,006	5	W4-S1061	150	0,0071	6	W4-S1022	105	1,37	8_1	W4-RD01	120	0,021	8_2	W4-RD01	120		x	x	x		SiPM-AFP	SiPM-AFP	26,5	42
3791	1504949898	306	207059	290	22	1	W9-LGA35	220	0,0035	2	W4-S203	120	0,006	5	W4-S1061	140	0,0048	6	W4-S1022	90	1,17	8_1	W4-RD01	120	0,021	8_2	W4-RD01	120		x	x	x		SiPM-AFP	SiPM-AFP	26,5	42
3792	1504950714	306	207094	290	22	1	W9-LGA35	220	0,0035	2	W4-S203	120	0,006	5	W4-S1061	140	0,0048	6	W4-S1022	90	1,17	8_1	W4-RD01	120	0,021	8_2	W4-RD01	120		x	x	x		SiPM-AFP	SiPM-AFP	26,5	41,5
3793	1504951486	306	207071	290	22	1	W9-LGA35	220	0,0035	2	W4-S203	120	0,006	5	W4-S1061	140	0,0048	6	W4-S1022	90	1,15	8_1	W4-RD01	120	0,021	8_2	W4-RD01	120		x	x	x		SiPM-AFP	SiPM-AFP	26,5	41,5
3794	1504952424	306	214219	289	22	1	W9-LGA35	220	0,0035	2	W4-S203	120	0,006	5	W4-S1061	140	0,0048	6	W4-S1022	90	1,15	8_1	W4-RD01	120	0,021	8_2	W4-RD01	120		x	x	x		SiPM-AFP	SiPM-AFP	26,5	42
3795	1504953251	306	207120	290	22	1	W9-LGA35	220	0,0035	2	W4-S203	120	0,006	5	W4-S1061	140	0,0048	6	W4-S1022	90	1,14	8_1	W4-RD01	120	0,021	8_2	W4-RD01	120		x	x	x		SiPM-AFP	SiPM-AFP	26,5	42
3796	1504954053	306	214458	230	22	1	W9-LGA35	220	0,0035	2	W4-S203	120	0,006	5	W4-S1061	140	0,0048	6	W4-S1022	90	1,14	8_1	W4-RD01	120	0,021	8_2	W4-RD01	120		x	x	x		SiPM-AFP	SiPM-AFP	26,5	42
3797	1504955229	306	214198	289	22	1	W9-LGA35	220	0,0035	2	W4-S203	120	0,006	5	W4-S1061	140	0,0048	6	W4-S1022	90	1,12	8_1	W4-RD01	120	0,021	8_2	W4-RD01	120		x	x	x		SiPM-AFP	SiPM-AFP	26,5	42
3798	1504956054	306	221311	286	22	1	W9-LGA35	220	0,0036	2	W4-S203	120	0,006	5	W4-S1061	140	0,0048	6	W4-S1022	90	1,11	8_1	W4-RD01	120	0,021	8_2	W4-RD01	120		x	x	x		SiPM-AFP	SiPM-AFP	26,5	42
3799	1504956907	306	257031	288	22	1	W9-LGA35	220	0,0036	2	W4-S203	120	0,006	5	W4-S1061	140	0,0048	6	W4-S1022	90	1,11	8_1	W4-RD01	120	0,021	8_2	W4-RD01	120		x	x	x		SiPM-AFP	SiPM-AFP	26,5	42
3800	1504957873	306	249930	288	22	1	W9-LGA35	220	0,0036	2	W4-S203	120	0,006	5	W4-S1061	140	0,0048	6	W4-S1022	90	1,1	8_1	W4-RD01	120	0,021	8_2	W4-RD01	120		x	x	x		SiPM-AFP	SiPM-AFP	26,5	42
3801	1504958794	306	249761	288	22	1	W9-LGA35	220	0,0036	2	W4-S203	120	0,006	5	W4-S1061	140	0,0048	6	W4-S1022	90	1,1	8_1	W4-RD01	120	0,021	8_2	W4-RD01	120		x	x	x		SiPM-AFP	SiPM-AFP	26,5	42
3802	1504959706	306	257040	281	22	1	W9-LGA35	220	0,0036	2	W4-S203	120	0,006	5	W4-S1061	140	0,0048	6	W4-S1022	90	1,1	8_1	W4-RD01	120	0,021	8_2	W4-RD01	120		x	x	x		SiPM-AFP	SiPM-AFP	26,5	42
3803	1504960732	306	256996	287	22	1	W9-LGA35	220	0,0036	2	W4-S203	120	0,006	5	W4-S1061	140	0,0048	6	W4-S1022	90	1,08	8_1	W4-RD01	120	0,021	8_2	W4-RD01	120		x	x	x		SiPM-AFP	SiPM-AFP	26,5	42
3844	1505001742	401	234374	122	-30	2	W4-S203	70	0,0014	3_2	W4-S215	60	0,002	5	W4-S1061	90	0,0015	6	W4-S1022	80	0,2028	SiPM-AFP	SiPM-AFP	26,5	45	3_0	W4-S215	60	0,002	3_1	W4-S215	60	0,002	3_3	W4-S215	60	0,002
3845	1505003975	401	205486	120	-30	2	W4-S203	70	0,0014	3_2	W4-S215	60	0,002	5	W4-S1061	90	0,0015	6	W4-S1022	80	0,1938	SiPM-AFP	SiPM-AFP	26,5	46	3_0	W4-S215	60	0,002	3_1	W4-S215	60	0,002	3_3	W4-S215	60	0,002
3846	1505005814	401	206239	200	-30	2	W4-S203	70	0,0014	3_2	W4-S215	60	0,002	5	W4-S1061	90	0,0015	6	W4-S1022	80	0,2015	SiPM-AFP	SiPM-AFP	26,5	46	3_0	W4-S215	60	0,002	3_1	W4-S215	60	0,002	3_3	W4-S215	60	0,002
3848	1505007024	401	206240	260	-30	2	W4-S203	70	0,0014	3_2	W4-S215	60	0,002	5	W4-S1061	90	0,0015	6	W4-S1022	80	0,2061	SiPM-AFP	SiPM-AFP	26,5	47	3_0	W4-S215	60	0,002	3_1	W4-S215	60	0,002	3_3	W4-S215	60	0,002
3849	1505008064	401	206180	230	-30	2	W4-S203	70	0,0014	3_2	W4-S215	60	0,002	5	W4-S1061	90	0,0015	6	W4-S1022	80	0,1983	SiPM-AFP	SiPM-AFP	26,5	47	3_0	W4-S215	60	0,002	3_1	W4-S215	60	0,002	3_3	W4-S215	60	0,002
3850	1505009123	402	199103	230	-30	2	W4-S203	65	0,0014	3_2	W4-S215	55	0,002	5	W4-S1061	80	0,0015	6	W4-S1022	70	0,1798	SiPM-AFP	SiPM-AFP	26,5	47	3_0	W4-S215	55	0,002	3_1	W4-S215	55	0,002	3_3	W4-S215	55	0,002
3851	1505010248	403	208695	230	-30	2	W4-S203	60	0,0014	3_2	W4-S215	50	0,002	5	W4-S1061	70	0,0014	6	W4-S1022	60	0,1621	SiPM-AFP	SiPM-AFP	26,5	47	3_0	W4-S215	50	0,002	3_1	W4-S215	50	0,002	3_3	W4-S215	50	0,002
3852	1505011342	404	201811	230	-30	2	W4-S203	55	0,0014	3_2	W4-S215	45	0,002	5	W4-S1061	60	0,0015	6	W4-S1022	50	0,1361	SiPM-AFP	SiPM-AFP	26,5	47	3_0	W4-S215	45	0,002	3_1	W4-S215	45	0,002	3_3	W4-S215	45	0,002
3853	1505012342	405	199222	220	-30	2	W4-S203	50	0,0014	3_2	W4-S215	40	0,002	5	W4-S1061	50	0,0015	6	W4-S1022	40	0,1257	SiPM-AFP	SiPM-AFP	26,5	48	3_0	W4-S215	40	0,002	3_1	W4-S215	40	0,002	3_3	W4-S215	40	0,002
3854	1505013532	406	206366	195	-30	2	W4-S203	45	0,0014	3_2	W4-S215	35	0,002	5	W4-S1061	40	0,0015	6	W4-S1022	90	0,239	SiPM-AFP	SiPM-AFP	26,5	48	3_0	W4-S215	35	0,002	3_1	W4-S215	35	0,002	3_3	W4-S215	35	0,002
3855	1505014681	402	206143	190	-30	2	W4-S203	65	0,0014	3_2	W4-S215	55	0,002	5	W4-S1061	80	0,0015	6	W4-S1022	70	0,1798	SiPM-AFP	SiPM-AFP	26,5	47	3_0	W4-S215	55	0,002	3_1	W4-S215	55	0,002	3_3	W4-S215	55	0,002
3863	1505035429	501	206931	389	-30	2	W4-S203	60	0,0014	3_2	W4-S215	80	0,003	5	W4-S1061	85	0,0015	6	W4-S1022	90	0,24	SiPM-AFP	SiPM-AFP	26,5	49	7_0	W4-S204_6e14	300	1,75	7_2	W4-S204_6e14	300		7_3	W4-S204_6e14	300	
3864	1505036154	502	207048	402	-30	2	W4-S203	60	0,0014	3_2	W4-S215	75	0,003	5	W4-S1061	85	0,0015	6	W4-S1022	90	0,24	SiPM-AFP	SiPM-AFP	26,5	49	7_0	W4-S204_6e14	290	1,56	7_2	W4-S204_6e14	290		7_3	W4-S204_6e14	290	
3865	1505036746	503	206887	403	-30	2	W4-S203	60	0,0014	3_2	W4-S215	70	0,003	5	W4-S1061	85	0,0015	6	W4-S1022	90	0,24	SiPM-AFP	SiPM-AFP	26,5	49	7_0	W4-S204_6e14	270	1,2	7_2	W4-S204_6e14	270		7_3	W4-S204_6e14	270	
3866	1505037456	504	206952	385	-30	2	W4-S203	60	0,0014	3_2	W4-S215	65	0,002	5	W4-S1061	85	0,0015	6	W4-S1022	90	0,24	SiPM-AFP	SiPM-AFP	26,5	49	7_0	W4-S204_6e14	250	1,28	7_2	W4-S204_6e14	250		7_3	W4-S204_6e14	250	
3867	1505038239	505	206984	288	-30	2	W4-S203	60	0,0014	3_2	W4-S215	60	0,001	5	W4-S1061	85	0,0015	6	W4-S1022	90	0,24	SiPM-AFP	SiPM-AFP	26,5	49	7_0	W4-S204_6e14	230	0,95	7_2	W4-S204_6e14	230		7_3	W4-S204_6e14	230	
3868	1505039099	506	206859	289	-30	2	W4-S203	60	0,0014	3_2	W4-S215	50	0,001	5	W4-S1061	85	0,0015	6	W4-S1022	90	0,24	SiPM-AFP	SiPM-AFP	26,5	49	7_0	W4-S204_6e14	200	0,78	7_2	W4-S204_6e14	200		7_3	W4-S204_6e14	200	
3869	1505040019	506	71325	296	-30	2	W4-S203	60	0,0014	3_2	W4-S215	50	0,001	5	W4-S1061	85	0,0015	6	W4-S1022	90	0,24	SiPM-AFP	SiPM-AFP	26,5	49	7_0	W4-S204_6e14	200	0,78	7_2	W4-S204_6e14	200		7_3	W4-S204_6e14	200	
3870	1505041059	507	206916	288	-30	2	W4-S203	60	0,0014	3_2	W4-S215	80	0,001	5	W4-S1061	85	0,0015	6	W4-S1022	90	0,24	SiPM-AFP	SiPM-AFP	26,5	49	7_0	W4-S204_6e14	250	1,28	7_2	W4-S204_6e14	250		7_3	W4-S204_6e14	250	
3871	1505041851	507	206834	283	-30	2	W4-S203	60	0,0014	3_2	W4-S215	80	0,001	5	W4-S1061	85	0,0015	6	W4-S1022	90	0,24	SiPM-AFP	SiPM-AFP	26,5	49	7_0	W4-S204_6e14	250	1,14	7_2	W4-S204_6e14	250		7_3	W4-S204_6e14	250	
3872	1505042699	507	206887	296	-30	2	W4-S203	60	0,0014	3_2	W4-S215	80	0,001	5	W4-S1061	85	0,0015	6	W4-S1022	90	0,24	SiPM-AFP	SiPM-AFP	26,5	49	7_0	W4-S204_6e14	250	1,28	7_2	W4-S204_6e14	250		7_3	W4-S204_6e14	250	
3873	1505043552	507	206892	295	-30	2	W4-S203	60	0,0014	3_2	W4-S215	80	0,001	5	W4-S1061	85	0,0015	6	W4-S1022	90	0,24	SiPM-AFP	SiPM-AFP	26,5	49,5	7_0	W4-S204_6e14	250	1,13	7_2	W4-S204_6e14	250		7_3	W4-S204_6e14	250	
3874	1505044586	507	206839	300	-30	2	W4-S203	60	0,0013	3_2	W4-S215	80	0,001	5	W4-S1061	85	0,0015	6	W4-S1022	90	0,23	SiPM-AFP	SiPM-AFP	26,5	49,2	7_0	W4-S204_6e14	250	1,21	7_2	W4-S204_6e14	250		7_3	W4-S204_6e14	250	
3875	1505045466	507	206954	287	-30	2	W4-S203	60	0,0013	3_2	W4-S215	80	0,001	5	W4-S1061	85	0,0015	6	W4-S1022	90	0,24	SiPM-AFP	SiPM-AFP	26,5	49	7_0	W4-S204_6e14	250	1,17	7_2	W4-S204_6e14	250		7_3	W4-S204_6e14	250	
3876	1505046356	507	240829	308	-30	2	W4-S203	60	0,0013	3_2	W4-S215	80	0,001	5	W4-S1061	85	0,0015	6	W4-S1022	90	0,24	SiPM-AFP	SiPM-AFP	26,5	49,5	7_0	W4-S204_6e14	250	1,1	7_2	W4-S204_6e14	250		7_3	W4-S204_6e14	250	
3877	1505047322	507	206930	310	-30	2	W4-S203	60	0,0013	3_2	W4-S215	80	0,001	5	W4-S1061	85	0,0015	6	W4-S1022	90	0,23	SiPM-AFP	SiPM-AFP	26,5	49,5	7_0	W4-S204_6e14	250	1,05	7_2	W4-S204_6e14	250		7_3	W4-S204_6e14	250	
3878	1505048114	507	207017	300	-30	2	W4-S203	60	0,0014	3_2	W4-S215	80	0,001	5	W4-S1061	85	0,0015	6	W4-S1022	90	0,24	SiPM-AFP	SiPM-AFP	26,5	49,5	7_0	W4-S204_6e14	250	1,03	7_2	W4-S204_6e14	250		7_3	W4-S204_6e14	250	
3879	1505048879	507	207074	290	-30	2	W4-S203	60	0,0013	3_2	W4-S215	80	0,001	5	W4-S1061	85	0,0015	6	W4-S1022	90	0,23	SiPM-AFP	SiPM-AFP	26,5	50	7_0	W4-S204_6e14	250	1	7_2	W4-S204_6e14	250		7_3	W4-S204_6e14	250	

Figure B.1: Run information for batches 101-507.

EUDAQ	Scope		#Events	Av.	T set	1-1				1-2				1-3				1-4			
RunNumber	Timestamp	Batch	This run	Rate [Hz]	T [C]	DUT Pos.	Sensor	V[V]	I [µA]	DUT Pos.	Sensor	V[V]	I [µA]	DUT Pos.	Sensor	V[V]	I [µA]	DUT Pos.	Sensor	V[V]	I [µA]
3889	1505056046	601	201079	174	-30	8_1	W4-RD01	60	0,003	8_2	W4-RD01	60	0,003	x	x	x	x	SiPM-AFP	SiPM-AFP	26,5	50
3890	1505057795	602	204374	179	-30	8_1	W4-RD01	75	0,003	8_2	W4-RD01	75	0,003	x	x	x	x	SiPM-AFP	SiPM-AFP	26,5	53
3891	1505059124	603	205321	164	-30	8_1	W4-RD01	70	0,003	8_2	W4-RD01	70	0,003	x	x	x	x	SiPM-AFP	SiPM-AFP	26,5	53,5
3892	1505060526	604	233869	171	-30	8_1	W4-RD01	65	0,003	8_2	W4-RD01	65	0,003	x	x	x	x	SiPM-AFP	SiPM-AFP	26,5	53,5
3893	1505062148	605	204448	172	-30	8_1	W4-RD01	50	0,003	8_2	W4-RD01	50	0,003	x	x	x	x	SiPM-AFP	SiPM-AFP	26,5	53
3894	1505063433	606	205304	172	-30	8_1	W4-RD01	40	0,003	8_2	W4-RD01	40	0,003	x	x	x	x	SiPM-AFP	SiPM-AFP	26,5	53
3895	1505064756	601	204161	178	-30	8_1	W4-RD01	60	0,003	8_2	W4-RD01	60	0,003	x	x	x	x	SiPM-AFP	SiPM-AFP	26,5	53,5
3896	1505065984	601	208061	146	-30	8_1	W4-RD01	60	0,003	8_2	W4-RD01	60	0,003	x	x	x	x	SiPM-AFP	SiPM-AFP	26,5	53
3897	1505067467	601	234052	165	-30	8_1	W4-RD01	60	0,003	8_2	W4-RD01	60	0,003	x	x	x	x	SiPM-AFP	SiPM-AFP	26,5	53,5
3898	1505068982	601	200803	172	-30	8_1	W4-RD01	60	0,003	8_2	W4-RD01	60	0,003	x	x	x	x	SiPM-AFP	SiPM-AFP	26,5	53,5
3899	1505070204	601	207099	177	-30	8_1	W4-RD01	60	0,003	8_2	W4-RD01	60	0,003	x	x	x	x	SiPM-AFP	SiPM-AFP	26,5	54
3900	1505071452	601	206252	173	-30	8_1	W4-RD01	60	0,003	8_2	W4-RD01	60	0,003	x	x	x	x	SiPM-AFP	SiPM-AFP	26,5	54
3901	1505072697	601	206579	151	-30	8_1	W4-RD01	60	0,003	8_2	W4-RD01	60	0,003	x	x	x	x	SiPM-AFP	SiPM-AFP	26,5	54
3902	1505074143	601	211450	158	-30	8_1	W4-RD01	60	0,003	8_2	W4-RD01	60	0,003	x	x	x	x	SiPM-AFP	SiPM-AFP	26,5	53,5
3903	1505075550	601	200572	155	-30	8_1	W4-RD01	60	0,003	8_2	W4-RD01	60	0,003	x	x	x	x	SiPM-AFP	SiPM-AFP	26,5	54
3908	1505120105	701v1	213562	201	-40	2	W4-S203	60	0,0014	3_2	W4-S215	65	0,003	5	W4-S1061	70	0,0015	6	W4-S1022	70	0,13
3909	1505121323	702v1	204242	240	-40	2	W4-S203	50	0,0014	3_2	W4-S215	55	0,003	5	W4-S1061	60	0,0015	6	W4-S1022	60	0,12
3910	1505122308	703v1	205711	240	-40	2	W4-S203	40	0,0014	3_2	W4-S215	50	0,003	5	W4-S1061	50	0,0015	6	W4-S1022	50	0,1
3911	1505123262	704v1	204232	230	-40	2	W4-S203	30	0,0014	3_2	W4-S215	45	0,003	5	W4-S1061	40	0,0015	6	W4-S1022	40	0,09
3912	1505124273	705v1	212427	230	-40	2	W4-S203	20	0,0014	3_2	W4-S215	40	0,003	5	W4-S1061	30	0,0015	6	W4-S1022	30	0,05
3913	STOPED because fixing some config problems																				
3914	STOPED because fixing scope settings																				
3915	1505125992	706v1																			
3916	1505126773	701	214097	400	-40	2	W4-S203	60	0,0014	3_2	W4-S215	65	0,003	5	W4-S1061	80	0,0015	6	W4-S1022	80	0,16
3917	1505127487	701	206823	380	-40	2	W4-S203	60	0,0014	3_2	W4-S215	65	0,003	5	W4-S1061	80	0,0015	6	W4-S1022	80	0,16
3918	1505128120	702	206831	380	-40	2	W4-S203	55	0,0014	3_2	W4-S215	60	0,003	5	W4-S1061	70	0,0015	6	W4-S1022	70	0,14
3919	1505128716	703	206925	380	-40	2	W4-S203	50	0,0014	3_2	W4-S215	55	0,003	5	W4-S1061	60	0,0015	6	W4-S1022	60	0,11
3920	1505129353	704	206861	390	-40	2	W4-S203	40	0,0014	3_2	W4-S215	50	0,003	5	W4-S1061	50	0,0015	6	W4-S1022	50	0,1
3921	1505129953	705	206865	246	-40	2	W4-S203	30	0,0013	3_2	W4-S215	45	0,003	5	W4-S1061	40	0,0015	6	W4-S1022	40	0,09
3922	1505130597	706	206841	390	-40	2	W4-S203	20	0,0013	3_2	W4-S215	40	0,003	5	W4-S1061	30	0,0015	6	W4-S1022	30	0,04
3924	1505131328	707	206874	336	-40	2	W4-S203	55	0,0014	3_2	W4-S215	60	0,003	5	W4-S1061	80	0,0015	6	W4-S1022	80	0,15
3925	1505132028	707	206958	285	-40	2	W4-S203	55	0,0014	3_2	W4-S215	60	0,003	5	W4-S1061	80	0,0015	6	W4-S1022	80	0,15
3928	1505132972	707	204785	330	-40	2	W4-S203	55	0,0014	3_2	W4-S215	60	0,003	5	W4-S1061	80	0,0015	6	W4-S1022	80	0,16
3929	1505133643	707	185331	350	-40	2	W4-S203	55	0,0014	3_2	W4-S215	60	0,003	5	W4-S1061	80	0,0015	6	W4-S1022	80	0,16
3930	1505134377	707	164138	400	-40	2	W4-S203	55	0,0014	3_2	W4-S215	60	0,003	5	W4-S1061	80	0,0015	6	W4-S1022	80	0,16
3978	1505232503	801	103850	89	20	1	W9-LGA44	160	0,002	2	W4-S1030	60	0,002	3	W4-LG12	60	0,002	SiPM-AFP	SiPM-AFP	26,5	55
3979	1505233734	802	103476	90	20	1	W9-LGA44	180	0,004	2	W4-S1030	70	0,002	3	W4-LG12	70	0,002	SiPM-AFP	SiPM-AFP	26,5	55
3980	1505234974	803	103023	90	20	1	W9-LGA44	200	0,004	2	W4-S1030	80	0,002	3	W4-LG12	80	0,002	SiPM-AFP	SiPM-AFP	26,5	55
3981	1505236230	804	102572	80	20	1	W9-LGA44	210	0,004	2	W4-S1030	100	0,002	3	W4-LG12	100	0,002	SiPM-AFP	SiPM-AFP	26,5	55
3982	1505237657	805	102531	75	20	1	W9-LGA44	220	0,004	2	W4-S1030	110	0,002	3	W4-LG12	110	0,002	SiPM-AFP	SiPM-AFP	26,5	56
3983	1505239044	806	105244	164	20	1	W9-LGA44	230	0,005	2	W4-S1030	120	0,002	3	W4-LG12	115	0,002	SiPM-AFP	SiPM-AFP	26,5	56
3999	1505246053	901	135265	400	20	1	SiPM-LAL	-53,4	13,7	2	SiPM-AFP	26,5	59	3	SiPM-UCSC 6	27	20,7	4	SiPM-UCSC 3	26	13
4000	1505246642	902	106706	420	20	1	SiPM-LAL	-53,7	18,7	2	SiPM-AFP	26	30	3	SiPM-UCSC 6	26,5	11,6	4	SiPM-UCSC 3	26	13
4001	1505247000	903	107009	420	20	1	SiPM-LAL	-53	8,5	2	SiPM-AFP	25,5	12	3	SiPM-UCSC 6	26	6	4	SiPM-UCSC 3	26	13

EUDAQ	2-1				2-2				2-3				2-4			
RunNumber	DUT Pos.	Sensor	V[V]	I [µA]	DUT Pos.	Sensor	V[V]	I [µA]	DUT Pos.	Sensor	V[V]	I [µA]	DUT Pos.	Sensor	V[V]	I [µA]
3889	x	x	x	x	x	x	x	x	x	x			x	x		
3890	x	x	x	x	x	x	x	x	x	x			x	x		
3891	x	x	x	x	x	x	x	x	x	x			x	x		
3892	x	x	x	x	x	x	x	x	x	x			x	x		
3893	x	x	x	x	x	x	x	x	x	x			x	x		
3894	x	x	x	x	x	x	x	x	x	x			x	x		
3895	x	x	x	x	x	x	x	x	x	x			x	x		
3896	x	x	x	x	x	x	x	x	x	x			x	x		
3897	x	x	x	x	x	x	x	x	x	x			x	x		
3898	x	x	x	x	x	x	x	x	x	x			x	x		
3899	x	x	x	x	x	x	x	x	x	x			x	x		
3900	x	x	x	x	x	x	x	x	x	x			x	x		
3901	x	x	x	x	x	x	x	x	x	x			x	x		
3902	x	x	x	x	x	x	x	x	x	x			x	x		
3903	x	x	x	x	x	x	x	x	x	x			x	x		
3908	SiPM-AFP	SiPM-AFP	26,5	53	7_0	W4-S204_6e14	270	0,43	7_2	W4-S204_6e14	270	0,43	7_3	W4-S204_6e14	270	0,43
3909	SiPM-AFP	SiPM-AFP	26,5	53	7_0	W4-S204_6e14	260	0,5	7_2	W4-S204_6e14	260	0,5	7_3	W4-S204_6e14	260	0,5
3910	SiPM-AFP	SiPM-AFP	26,5	53	7_0	W4-S204_6e14	240	0,4	7_2	W4-S204_6e14	240	0,4	7_3	W4-S204_6e14	240	0,4
3911	SiPM-AFP	SiPM-AFP	26,5	53	7_0	W4-S204_6e14	230	0,36	7_2	W4-S204_6e14	230	0,36	7_3	W4-S204_6e14	230	0,36
3912	SiPM-AFP	SiPM-AFP	26,5	53	7_0	W4-S204_6e14	200	0,41	7_2	W4-S204_6e14	200	0,41	7_3	W4-S204_6e14	200	0,41
3913																
3914																
3915																
3916	SiPM-AFP	SiPM-AFP	26,5	54	7_0	W4-S204_6e14	270	0,57	7_2	W4-S204_6e14	270	0,57	7_3	W4-S204_6e14	270	0,57
3917	SiPM-AFP	SiPM-AFP	26,5	54	7_0	W4-S204_6e14	270	0,57	7_2	W4-S204_6e14	270	0,57	7_3	W4-S204_6e14	270	0,57
3918	SiPM-AFP	SiPM-AFP	26,5	54	7_0	W4-S204_6e14	260	0,58	7_2	W4-S204_6e14	270	0,57	7_3	W4-S204_6e14	270	0,57
3919	SiPM-AFP	SiPM-AFP	26,5	55	7_0	W4-S204_6e14	250	0,45	7_2	W4-S204_6e14	250	0,45	7_3	W4-S204_6e14	250	0,45
3920	SiPM-AFP	SiPM-AFP	26,5	55	7_0	W4-S204_6e14	240	0,45	7_2	W4-S204_6e14	240	0,4	7_3	W4-S204_6e14	240	0,4
3921	SiPM-AFP	SiPM-AFP	26,5	55	7_0	W4-S204_6e14	230	0,39	7_2	W4-S204_6e14	230	0,39	7_3	W4-S204_6e14	230	0,39
3922	SiPM-AFP	SiPM-AFP	26,5	55	7_0	W4-S204_6e14	200	0,28	7_2	W4-S204_6e14	200	0,28	7_3	W4-S204_6e14	200	0,28
3924	SiPM-AFP	SiPM-AFP	26,5	55	7_0	W4-S204_6e14	250	0,48	7_2	W4-S204_6e14	250	0,48	7_3	W4-S204_6e14	250	0,48
3925	SiPM-AFP	SiPM-AFP	26,5	55	7_0	W4-S204_6e14	250	0,49	7_2	W4-S204_6e14	250	0,48	7_3	W4-S204_6e14	250	0,48
3928	SiPM-AFP	SiPM-AFP	26,5	56	7_0	W4-S204_6e14	250	0,55	7_2	W4-S204_6e14	250	0,55	7_3	W4-S204_6e14	250	0,55
3929	SiPM-AFP	SiPM-AFP	26,5	56	7_0	W4-S204_6e14	250	0,55	7_2	W4-S204_6e14	250	0,55	7_3	W4-S204_6e14	250	0,55
3930	SiPM-AFP	SiPM-AFP	26,5	56	7_0	W4-S204_6e14	250	0,55	7_2	W4-S204_6e14	250	0,55	7_3	W4-S204_6e14	250	0,55
3978	x	x	x	x	x	x	x	x	x	x			x	x		
3979	x	x	x	x	x	x	x	x	x	x			x	x		
3980	x	x	x	x	x	x	x	x	x	x			x	x		
3981	x	x	x	x	x	x	x	x	x	x			x	x		
3982	x	x	x	x	x	x	x	x	x	x			x	x		
3983	x	x	x	x	x	x	x	x	x	x			x	x		
3999	x	x	x	x	x	x	x	x	x	x			x	x		
4000	x	x	x	x	x	x	x	x	x	x			x	x		
4001	x	x	x	x	x	x	x	x	x	x			x	x		

Figure B.2: Run information for batches 601-903, where 801-804 and 901-903 are not used.

Appendix C

Choice of number of samples

This section presents plots for the dependence of number of events with maximum sample value and number of samples above the threshold U_S discussed in Section 4.1.2. All sensors are shown, except for W4-S203 which is in Figure 4.2c. From these plots, the N_{samples} is chosen which is listed in Table 4.1.

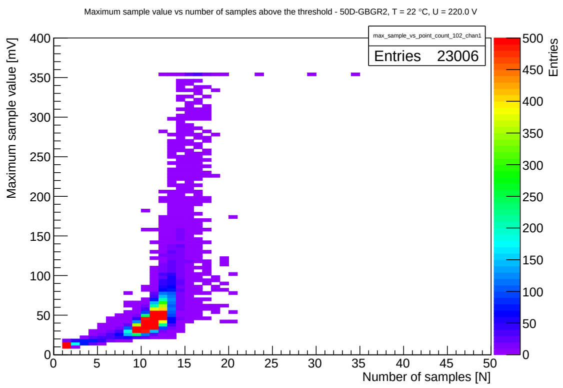

(a) 50D-GBGR2, $N_{\text{samples}} = 5$.

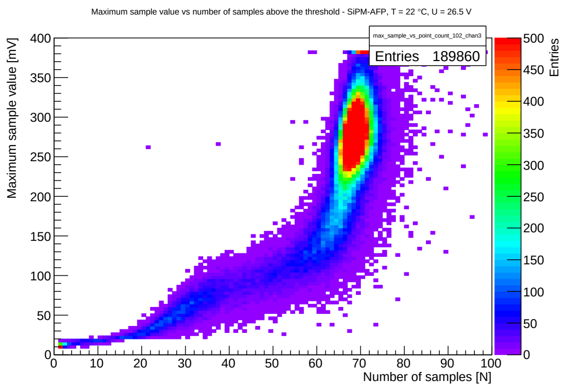

(b) SiPM, $N_{\text{samples}} = 36$.

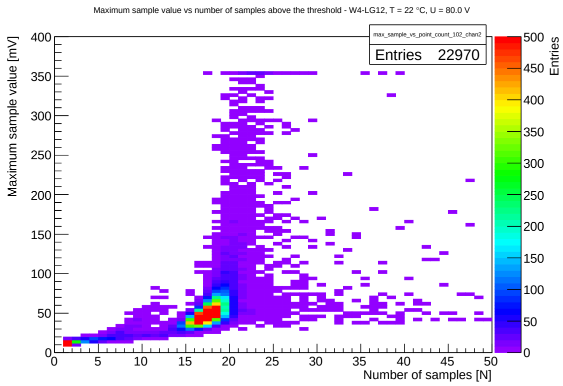

(c) W4-LG12, $N_{\text{samples}} = 8$.

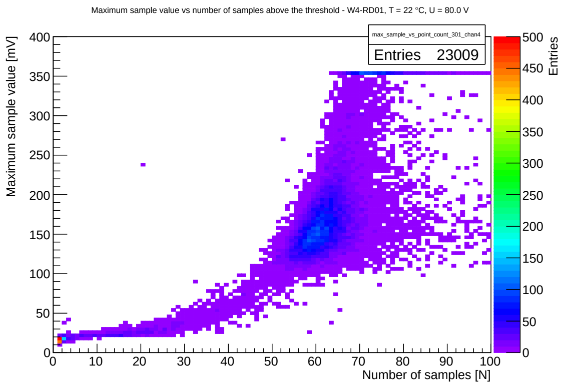

(d) W4-RD01, $N_{\text{samples}} = 32$.

Figure C.1: Maximum sample value versus number of samples above U_S for 50D-GBGR2, SiPM, W4-LG12 and W4-RD01 with selected N_{samples}.

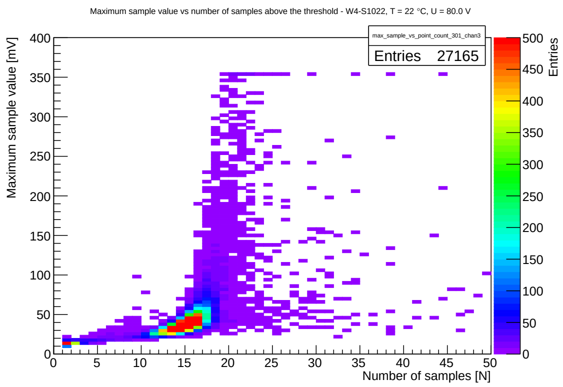

(a) W4-S1022, $N_{\text{samples}} = 7$.

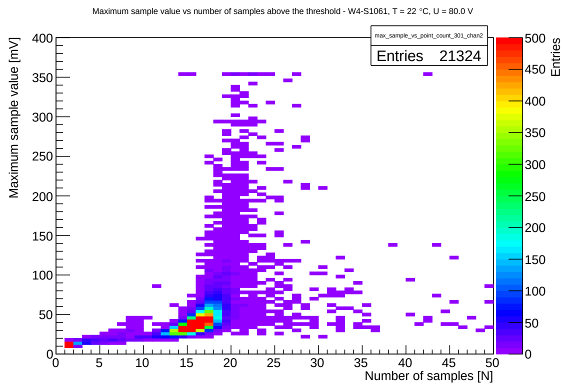

(b) W4-S1061, $N_{\text{samples}} = 8$.

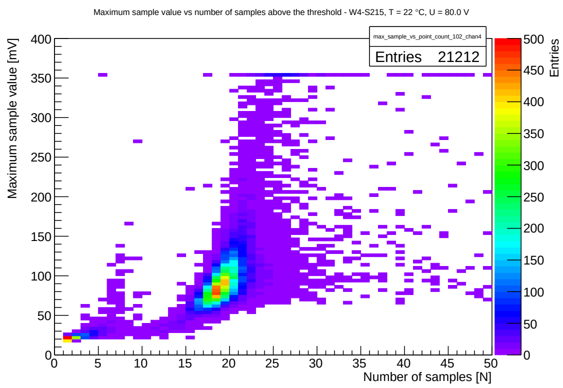

(c) W4-S215, $N_{\text{samples}} = 8$.

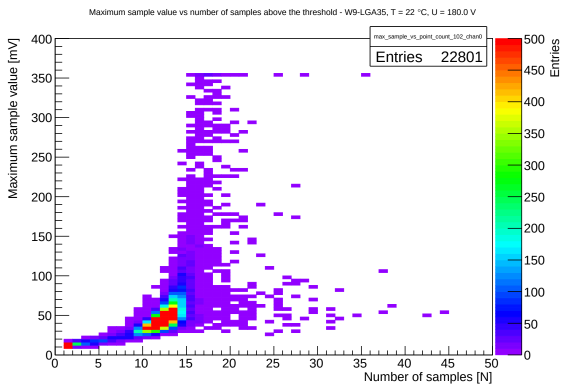

(d) W9-LGA35, $N_{\text{samples}} = 5$.

Figure C.2: Maximum sample value versus number of samples above U_S for W4-S1022, W4-S1061, W4-S215, and W9-LGA35 with selected N_{samples}.

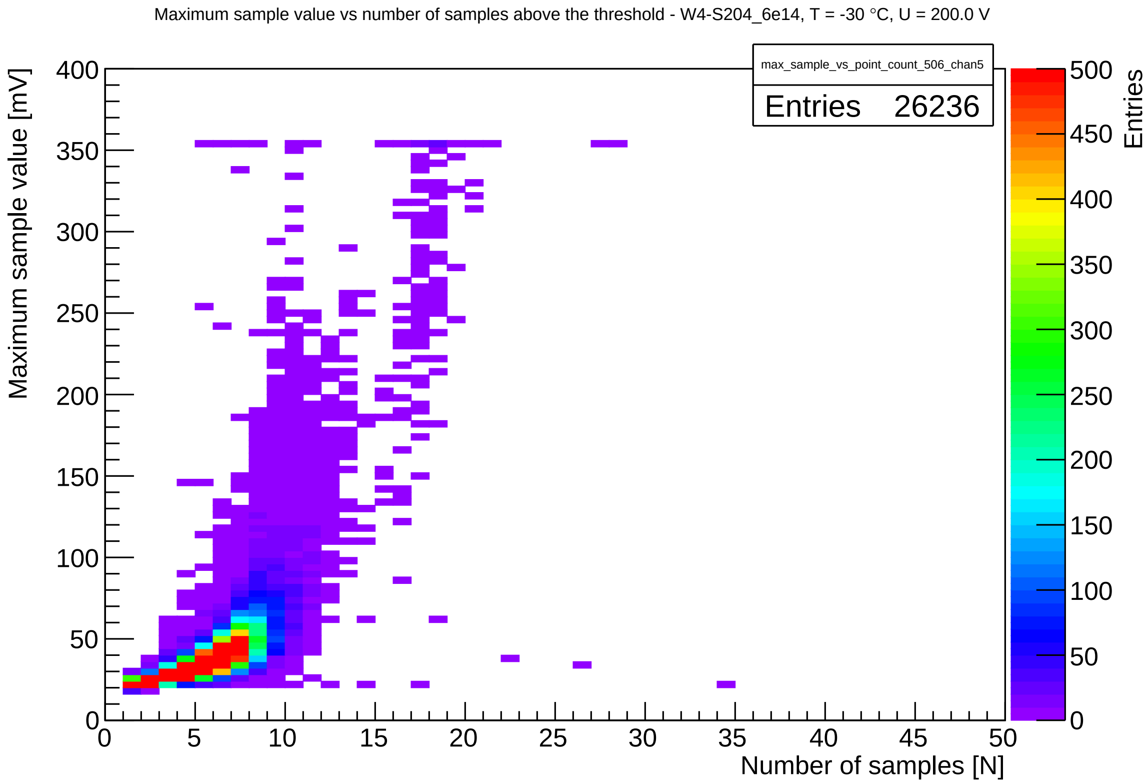

Figure C.3: Maximum sample value versus number of samples above U_S for W4-S204 with selected $N_{\text{samples}} = 3$.

Appendix D

Additional track-based results

This section presents the track-based plots for all sensors. The different characteristics shown are efficiency, gain, pulse amplitude, rise time and timing resolution with CFD method and using the location at the peak of the pulse. Some track-based plots showing the timing resolution are missing because the sensor was connected to a different oscilloscope than the SiPM.

D.1 50D-GBGR2

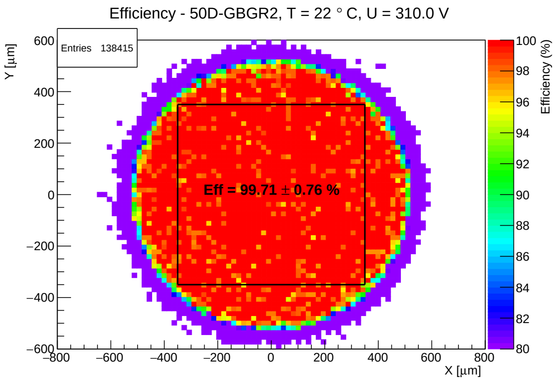

(a) Efficiency.

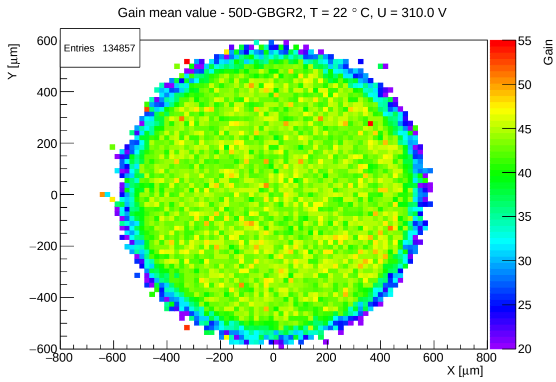

(b) Gain.

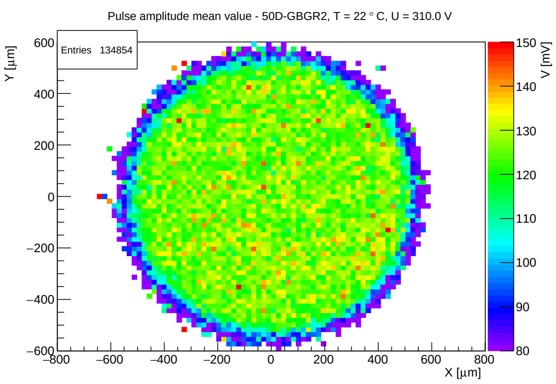

(c) Pulse amplitude.

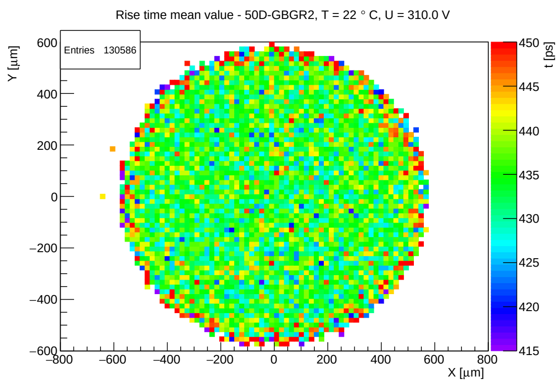

(d) Rise time.

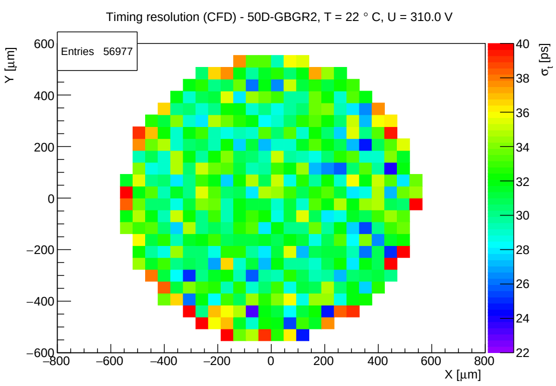

(e) Timing resolution - CFD method.

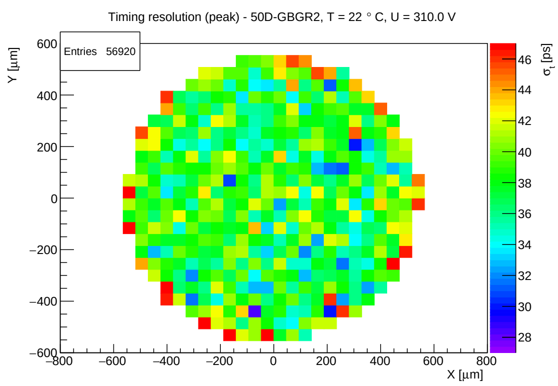

(f) Timing resolution - peak location method.

Figure D.1: Track-based plots for 50D-GBGR2 at $T = 22\,°\mathrm{C}$.

D.2 W4-LG12

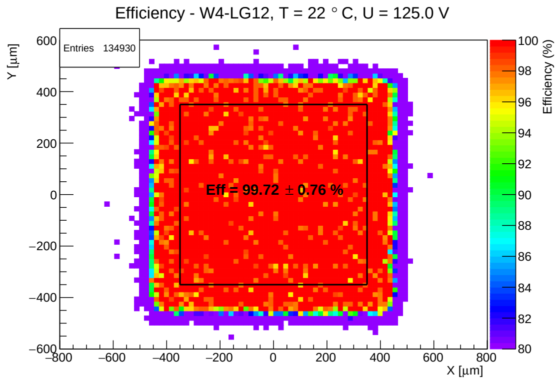

(a) Efficiency.

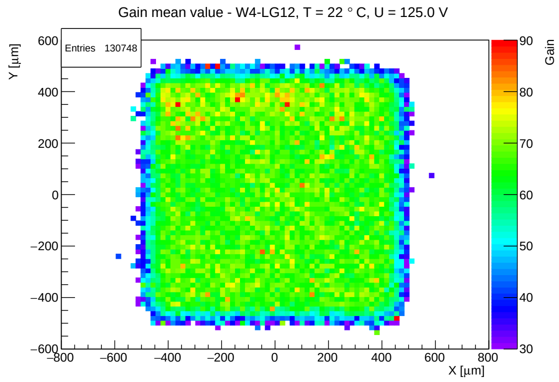

(b) Gain.

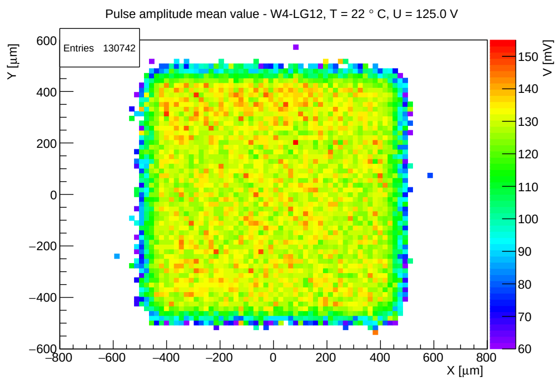

(c) Pulse amplitude.

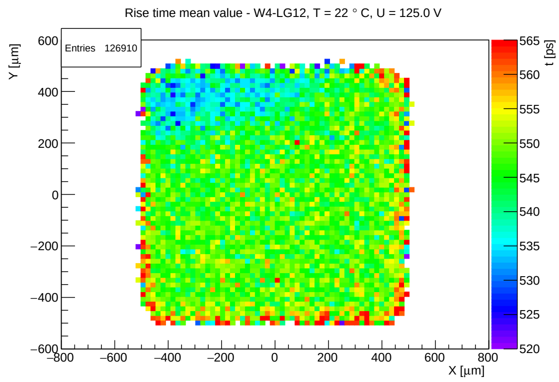

(d) Rise time.

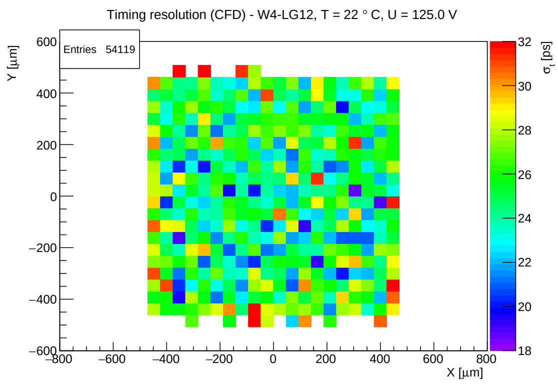

(e) Timing resolution - CFD method.

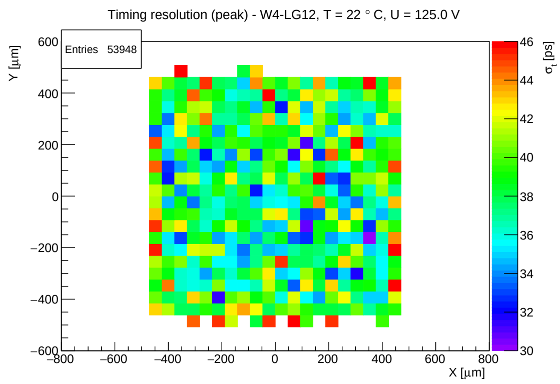

(f) Timing resolution - peak location method.

Figure D.2: Track-based plots for W4-LG12 at $T = 22\,°\mathrm{C}$.

D.3 W4-RD01

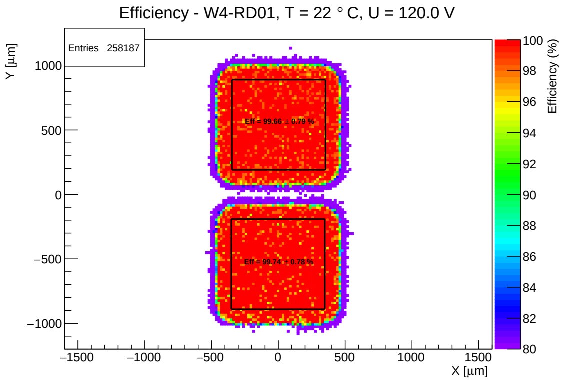

(a) Efficiency.

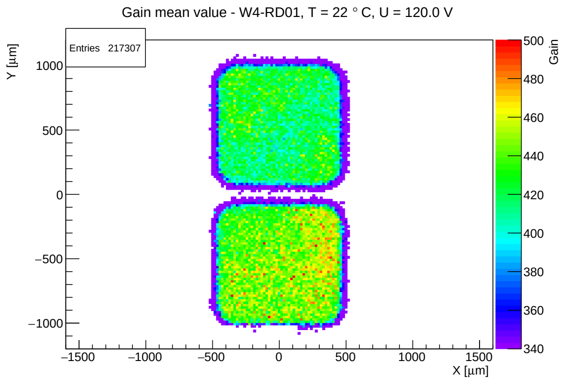

(b) Gain.

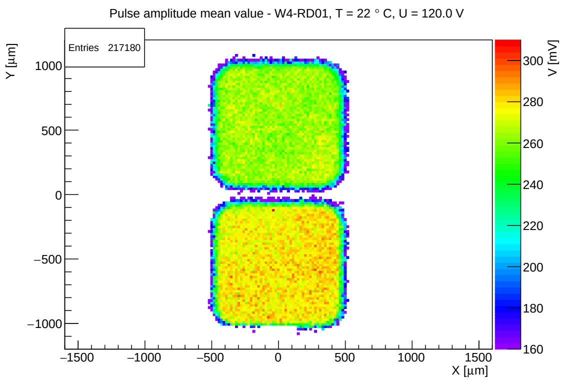

(c) Pulse amplitude.

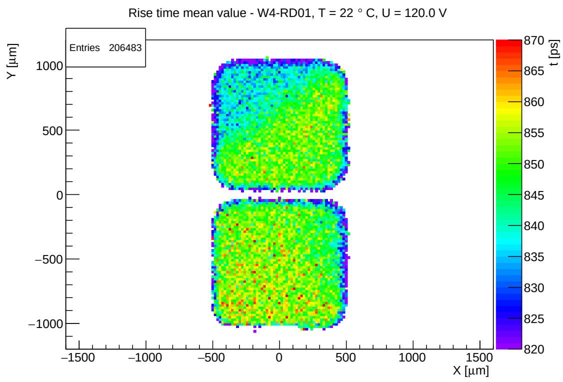

(d) Rise time.

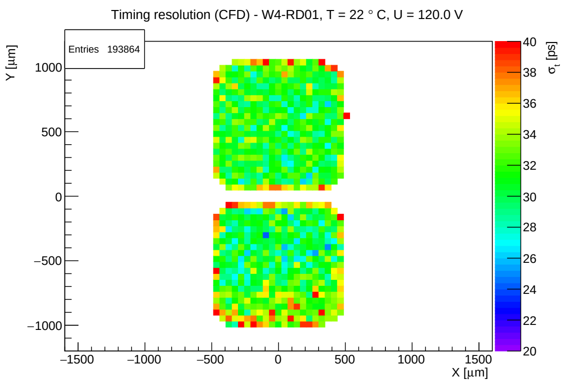

(e) Timing resolution - CFD method.

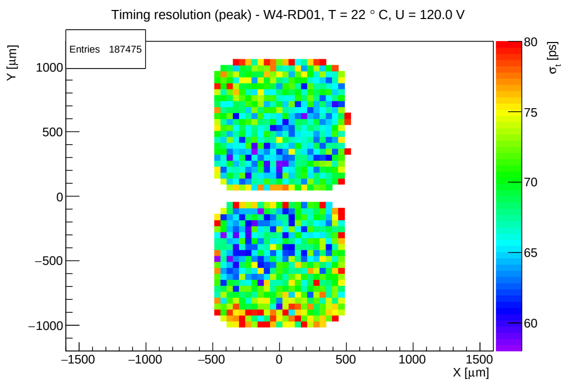

(f) Timing resolution - peak location method.

Figure D.3: Track-based plots for W4-RD01 at $T = 22\,°\mathrm{C}$. The upper pad is selected to show the results.

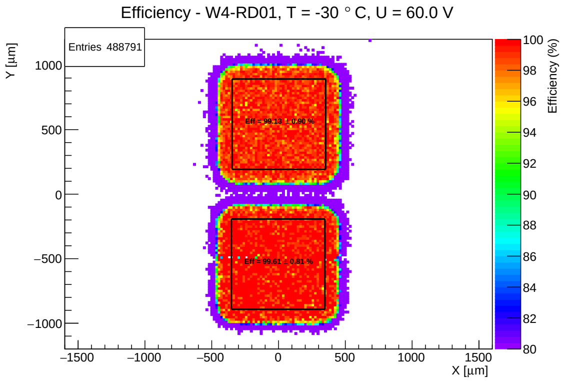

(a) Efficiency.

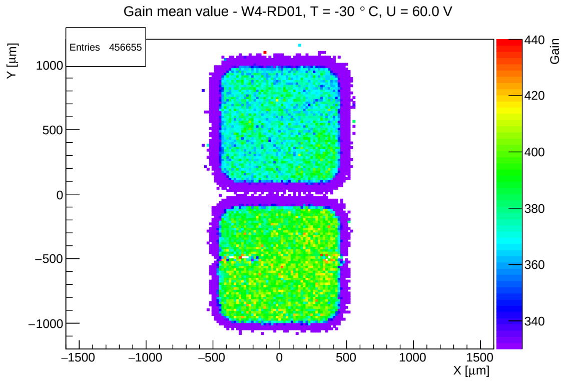

(b) Gain.

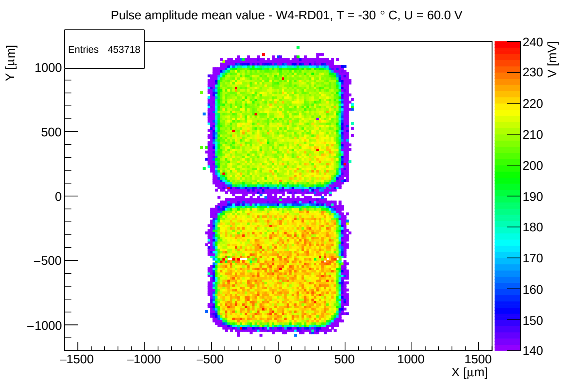

(c) Pulse amplitude.

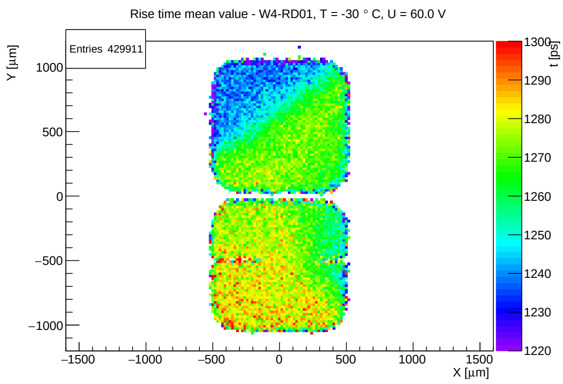

(d) Rise time.

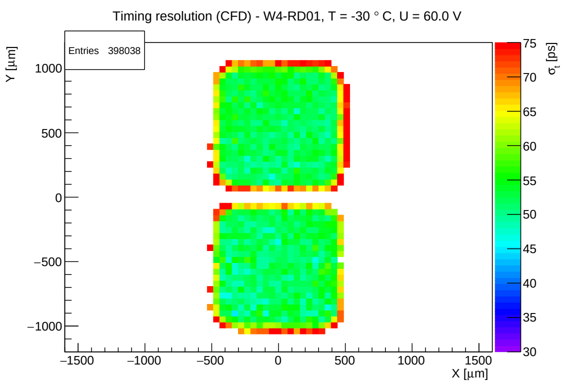

(e) Timing resolution - CFD method.

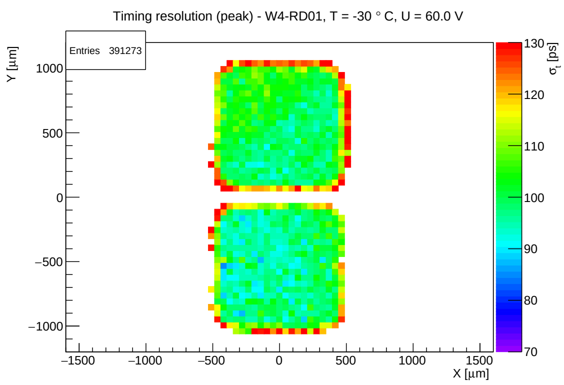

(f) Timing resolution - peak location method.

Figure D.4: Track-based plots for W4-RD01 at $T = -30\,°\mathrm{C}$.

D.4 W4-S1022

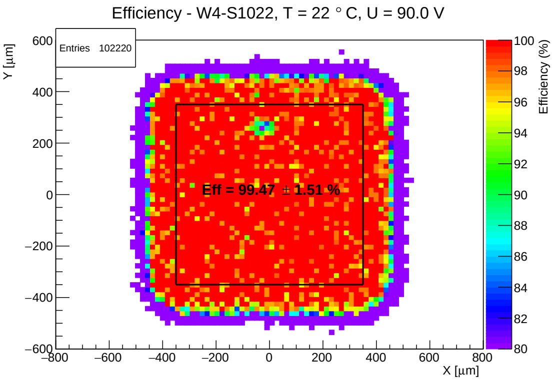

(a) Efficiency.

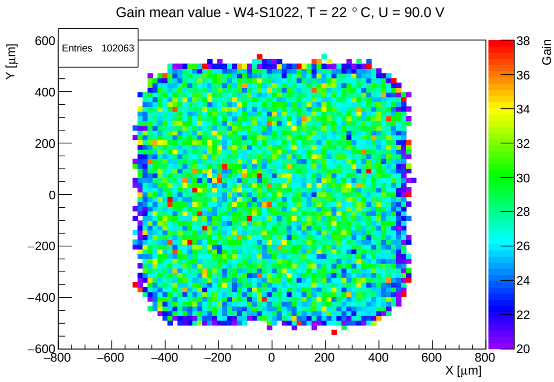

(b) Gain.

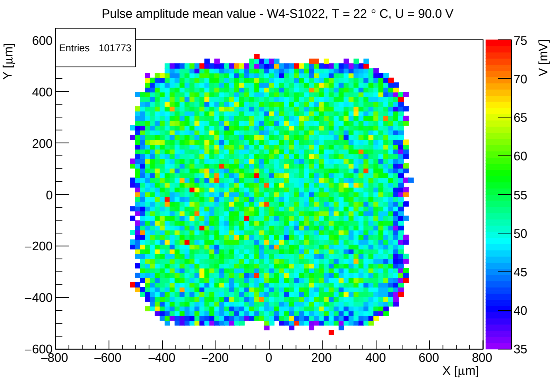

(c) Pulse amplitude.

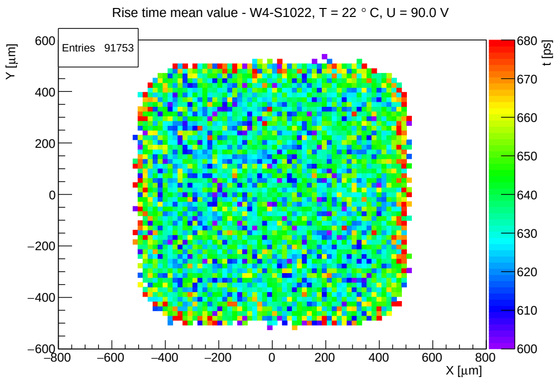

(d) Rise time.

Figure D.5: Track-based plots for W4-S1022 at $T = 22\,°\mathrm{C}$.

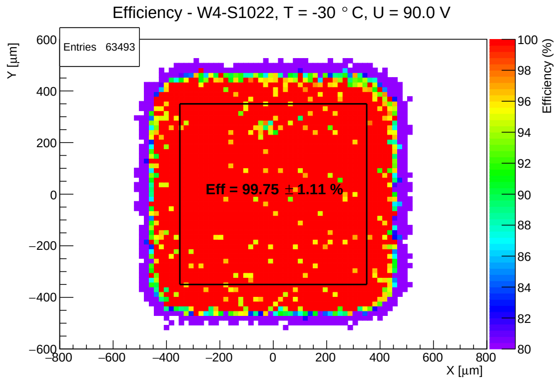

(a) Efficiency.

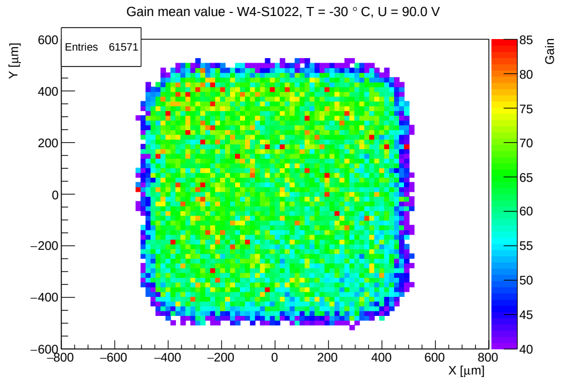

(b) Gain.

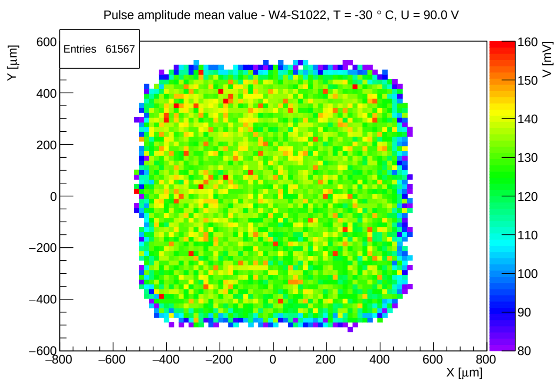

(c) Pulse amplitude.

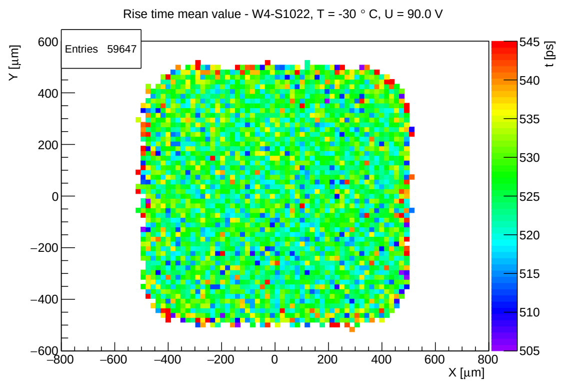

(d) Rise time.

Figure D.6: Track-based plots for W4-S1022 at $T = -30\,°\mathrm{C}$.

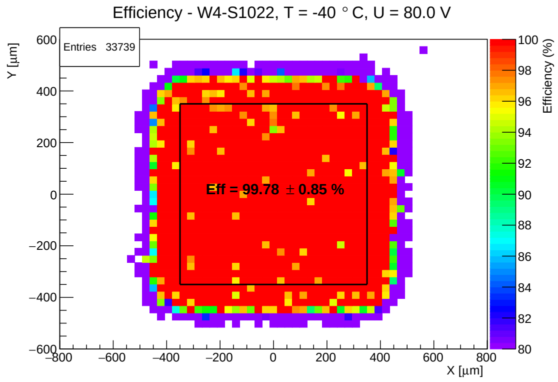

(a) Efficiency.

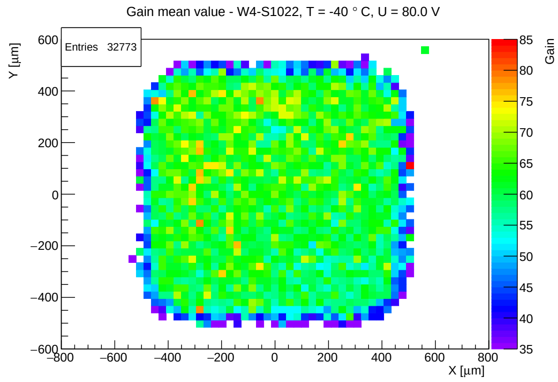

(b) Gain.

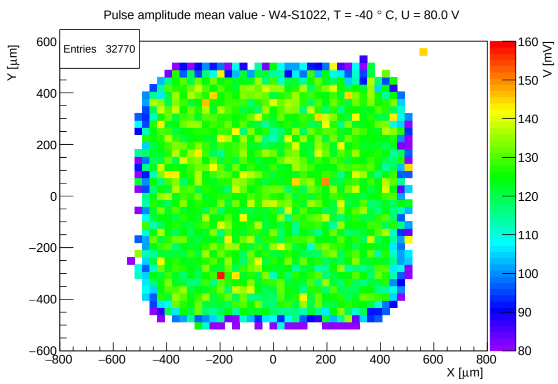

(c) Pulse amplitude.

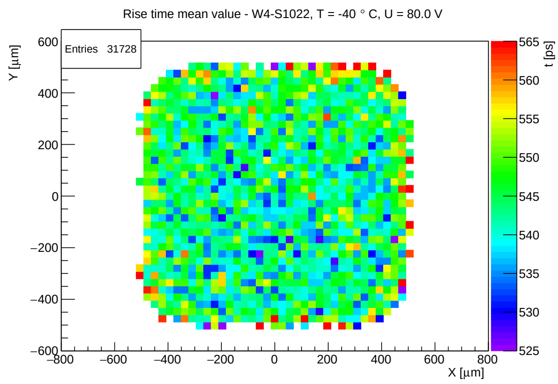

(d) Rise time.

Figure D.7: Track-based plots for W4-S1022 at $T = -40\,°C$. The bin size is increased with 50% due to lower data statistics.

D.5 W4-S1061

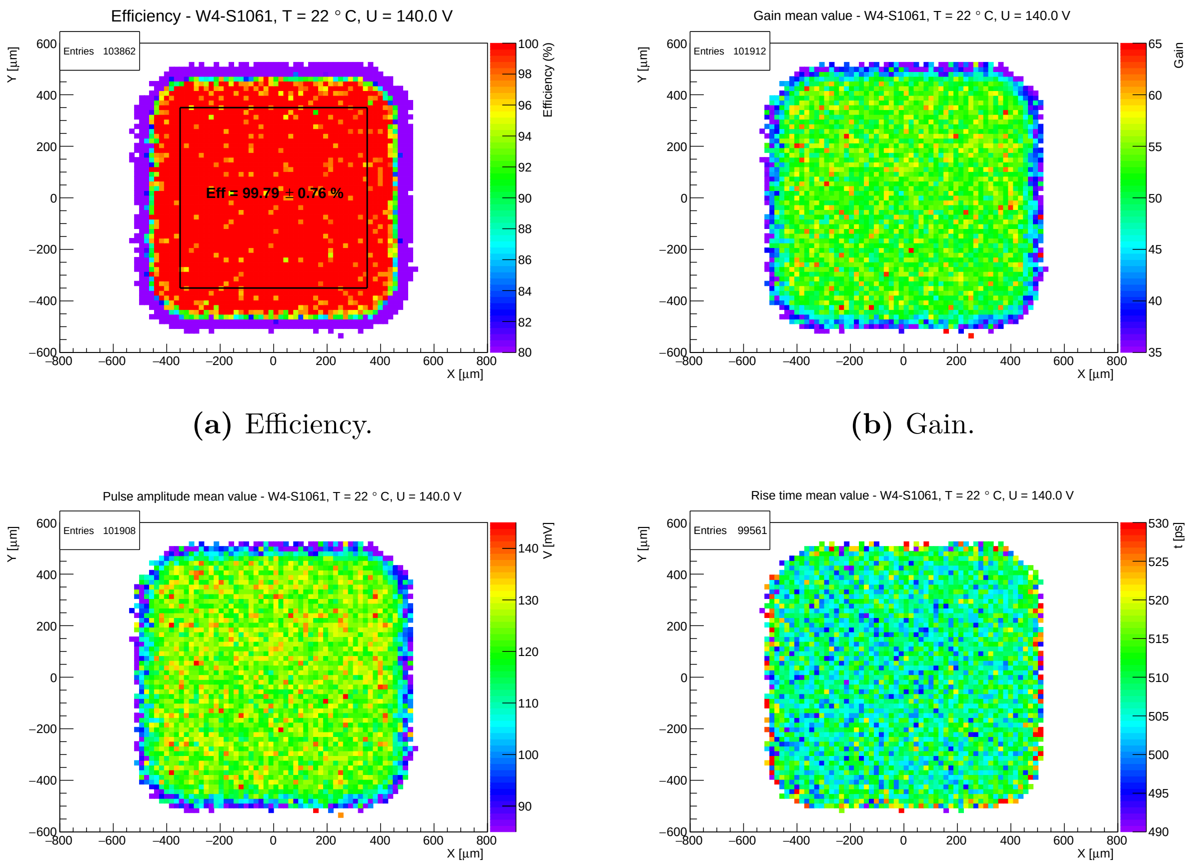

(a) Efficiency. **(b)** Gain. **(c)** Pulse amplitude. **(d)** Rise time.

Figure D.8: Track-based plots for W4-S1061 at $T = 22\,°\text{C}$.

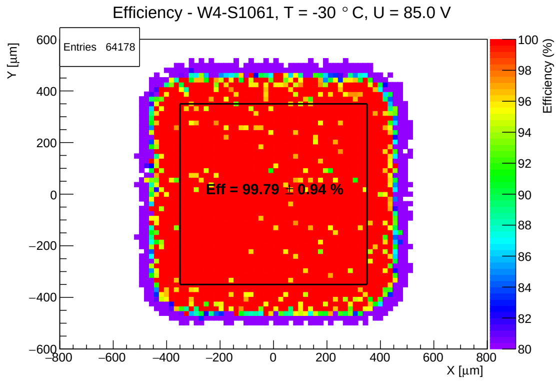

(a) Efficiency.

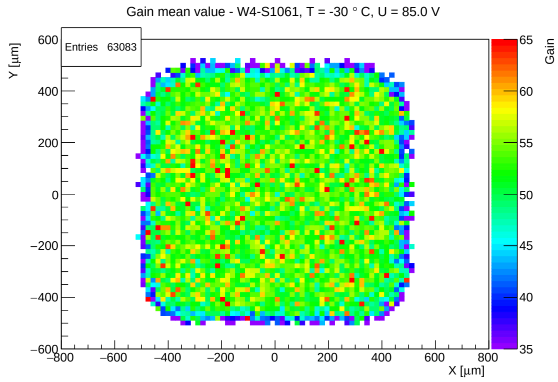

(b) Gain.

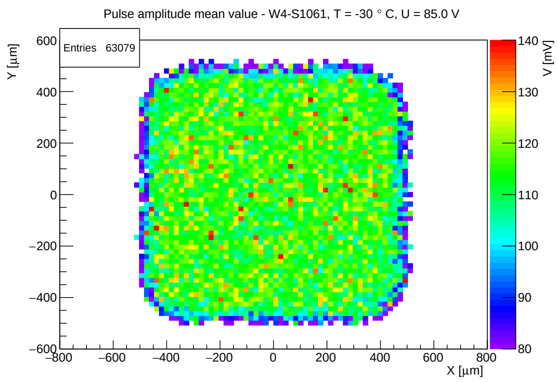

(c) Pulse amplitude.

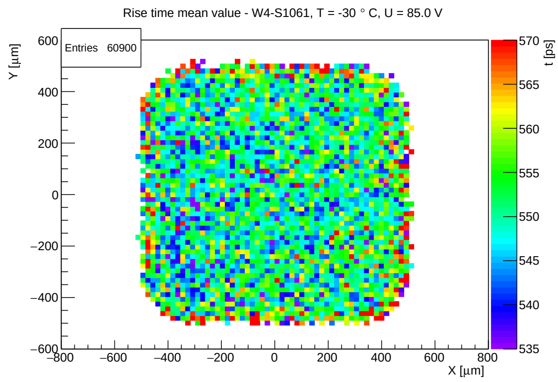

(d) Rise time.

Figure D.9: Track-based plots for W4-S1061 at $T = -30\,°C$.

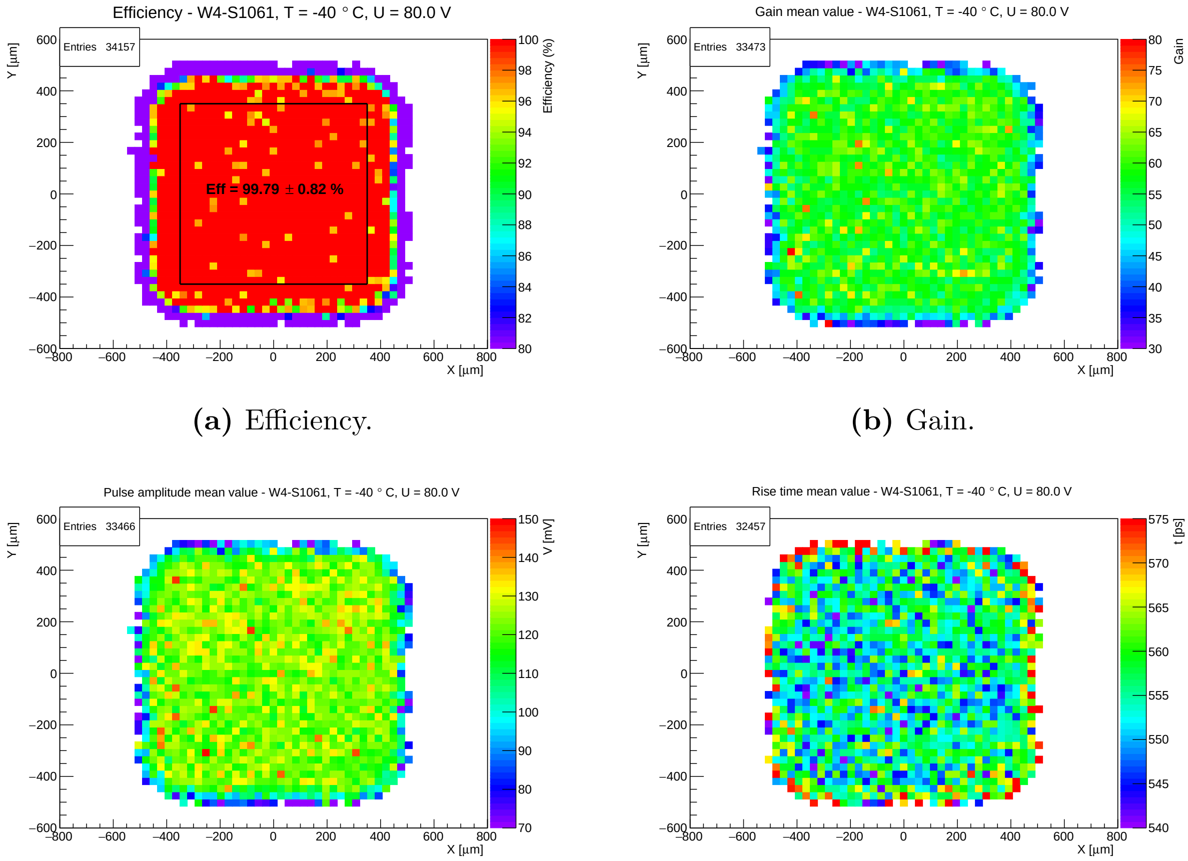

(a) Efficiency. **(b)** Gain.

(c) Pulse amplitude. **(d)** Rise time.

Figure D.10: Track-based plots for W4-S1061 at $T = -40\,°\mathrm{C}$. The bin size is increased with 50% due to lower data statistics.

D.6 W4-S203

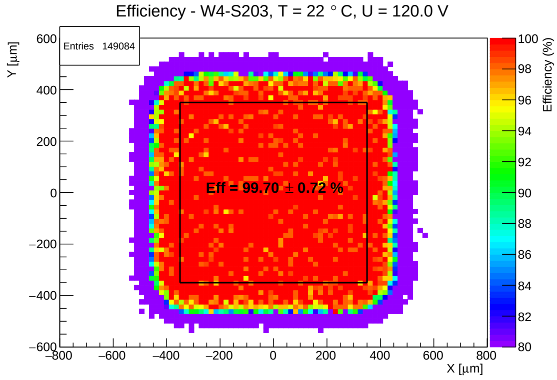

(a) Efficiency.

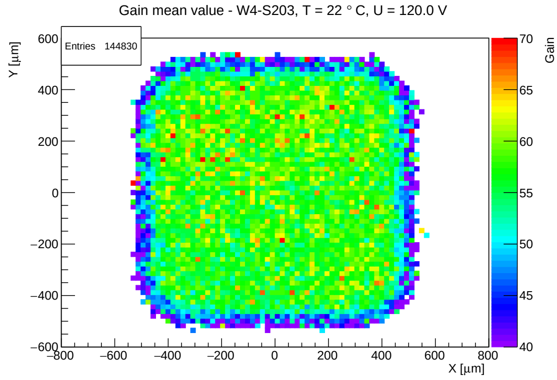

(b) Gain.

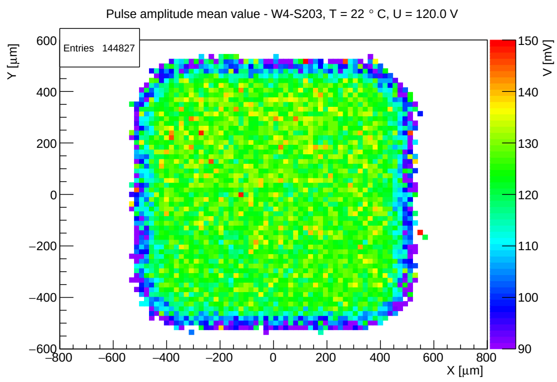

(c) Pulse amplitude.

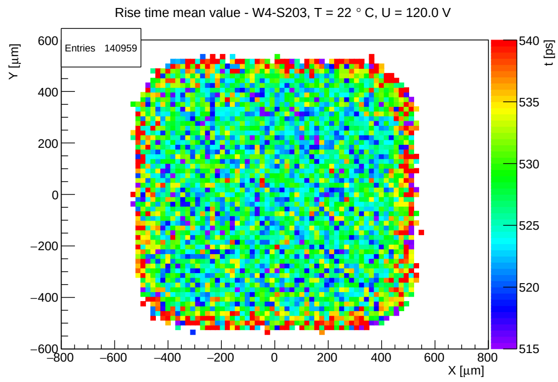

(d) Rise time.

Figure D.11: Track-based plots for W4-S203 at $T = 22\,°\mathrm{C}$.

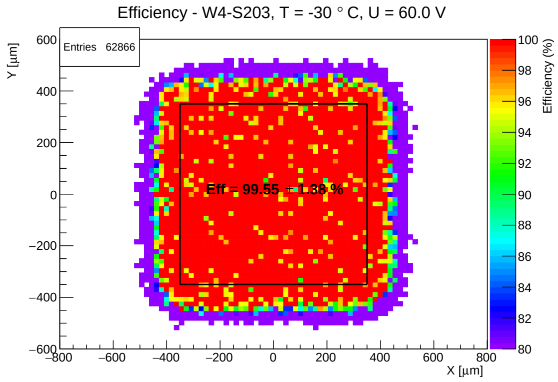

(a) Efficiency.

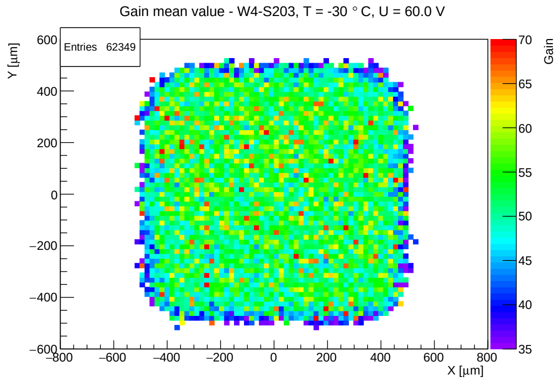

(b) Gain.

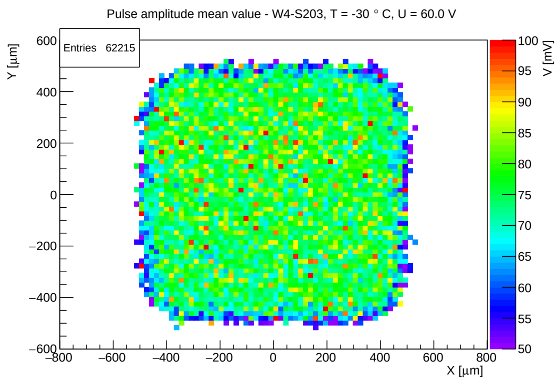

(c) Pulse amplitude.

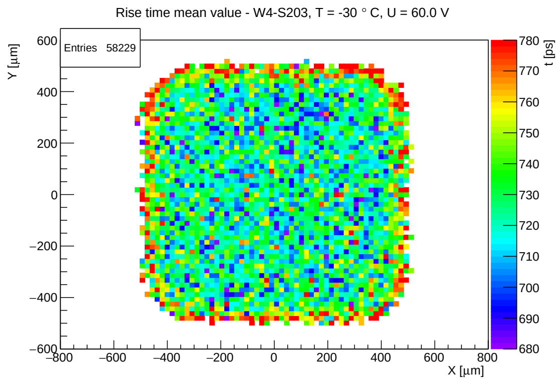

(d) Rise time.

Figure D.12: Track-based plots for W4-S203 at $T = -30\,°\mathrm{C}$.

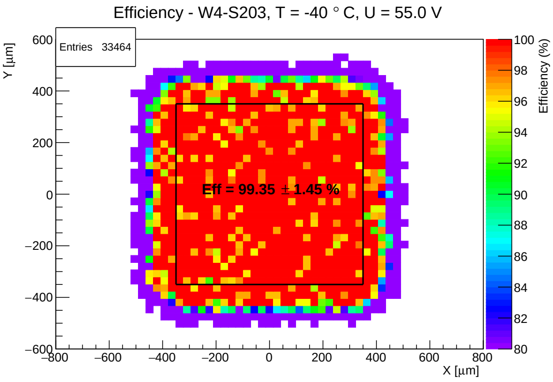

(a) Efficiency.

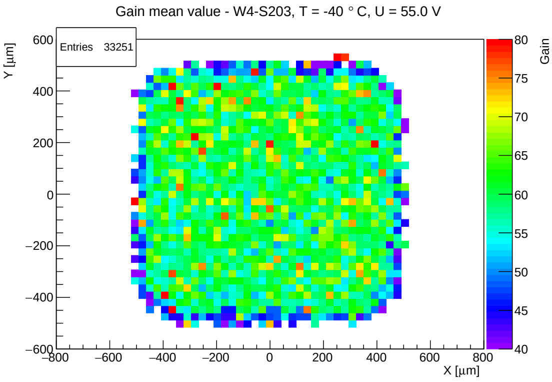

(b) Gain.

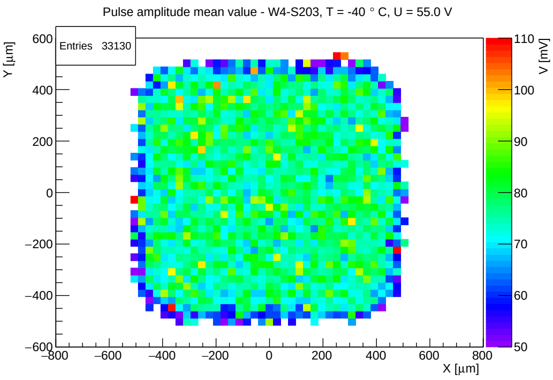

(c) Pulse amplitude.

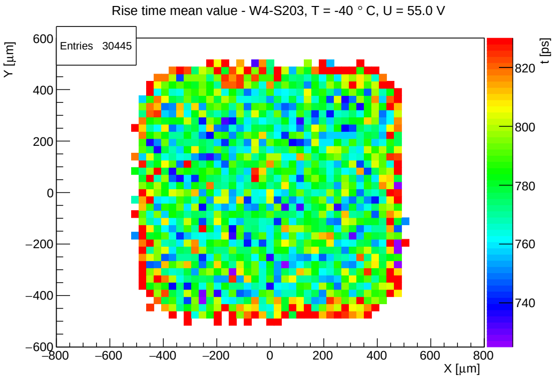

(d) Rise time.

Figure D.13: Track-based plots for W4-S203 at $T = -40\,°\mathrm{C}$. The bin size is increased with 50% due to lower data statistics.

D.7 W4-S204

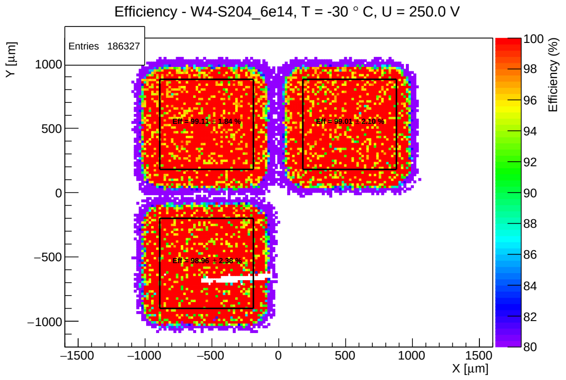

(a) Efficiency.

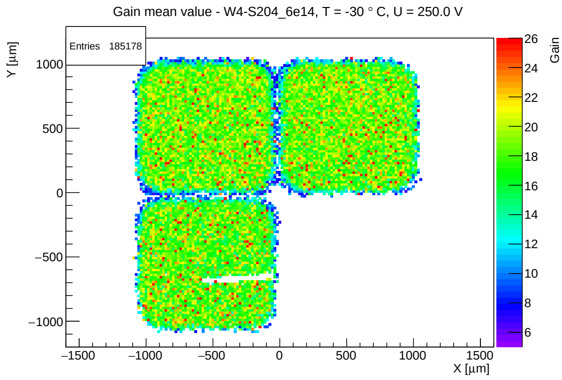

(b) Gain.

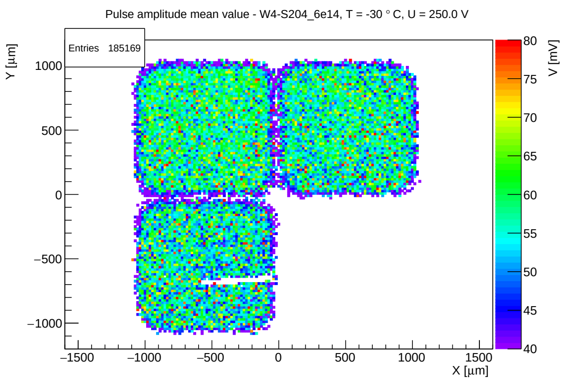

(c) Pulse amplitude.

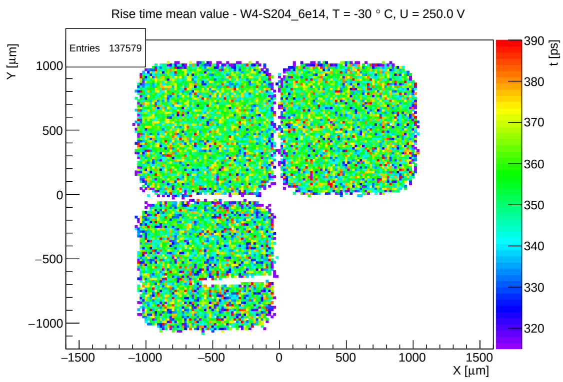

(d) Rise time.

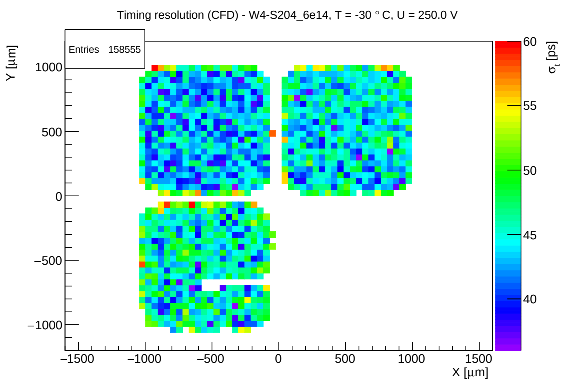

(e) Timing resolution - CFD method.

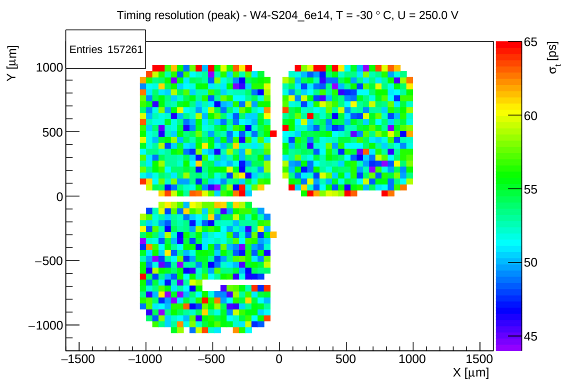

(f) Timing resolution - peak location method.

Figure D.14: Track-based plots for W4-S204 at $T = -30\,°\mathrm{C}$. The upper-left pad is selected to show the results. The line with missing information is because of a broken MIMOSA plane, leading to missing data

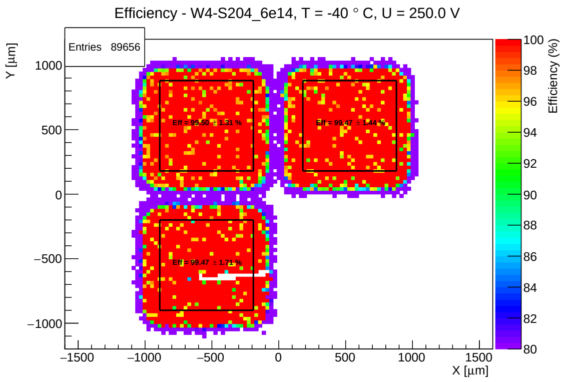

(a) Efficiency.

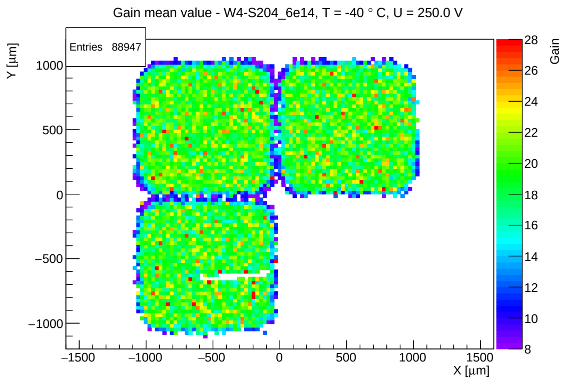

(b) Gain.

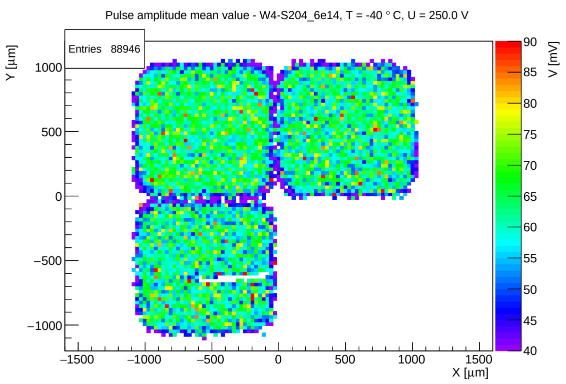

(c) Pulse amplitude.

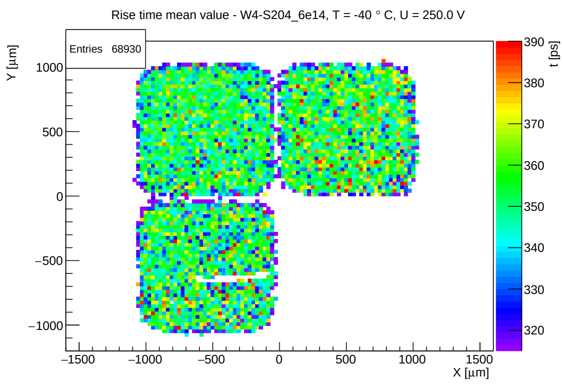

(d) Rise time.

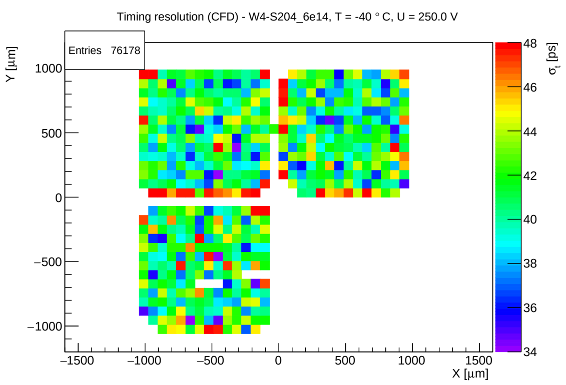

(e) Timing resolution - CFD method.

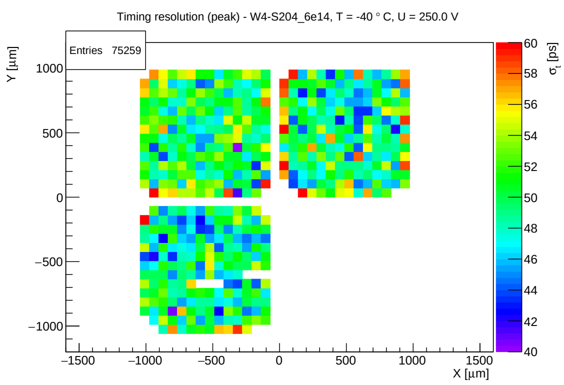

(f) Timing resolution - peak location method.

Figure D.15: Track-based plots for W4-S204 at $T = -40\,°\mathrm{C}$. The bin size is increased with 50% due to lower data statistics. The line with missing information is because of a broken MIMOSA plane, leading to missing data.

D.8 W4-S215

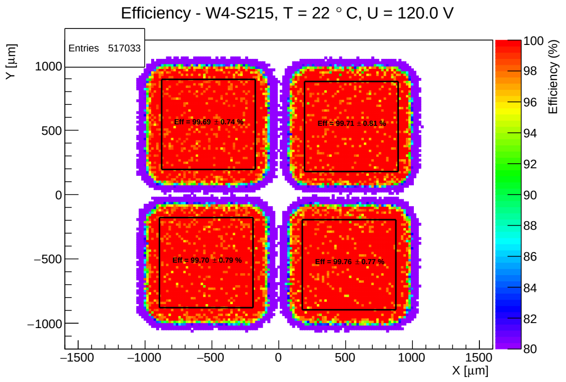

(a) Efficiency.

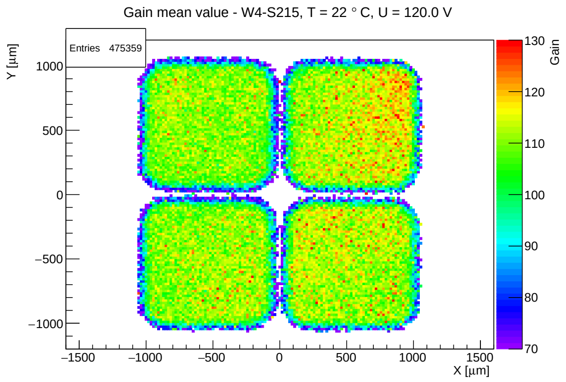

(b) Gain.

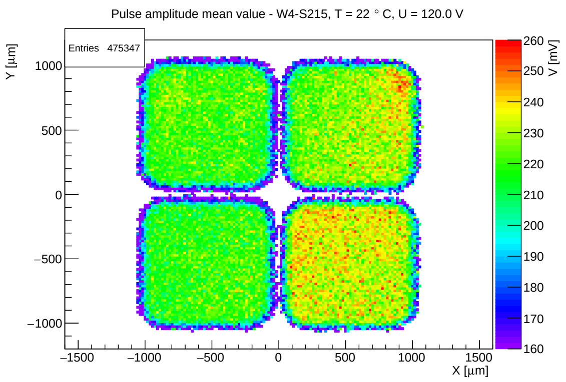

(c) Pulse amplitude.

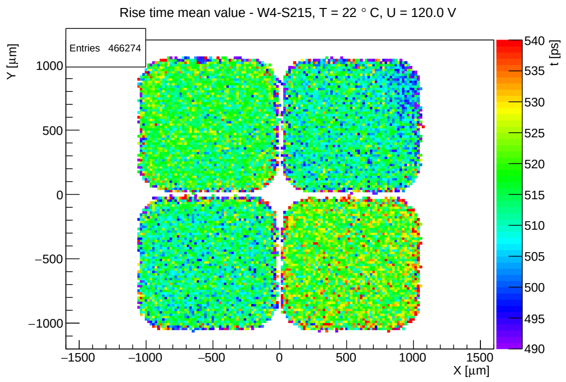

(d) Rise time.

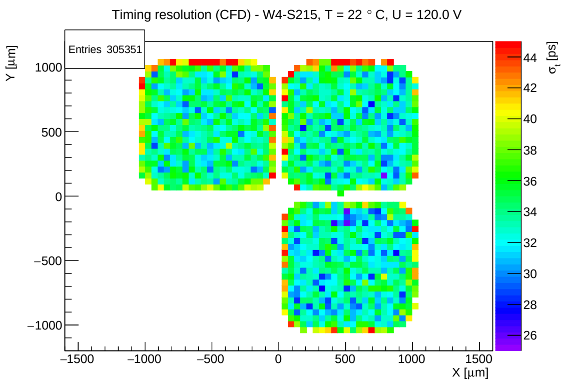

(e) Timing resolution - CFD method.

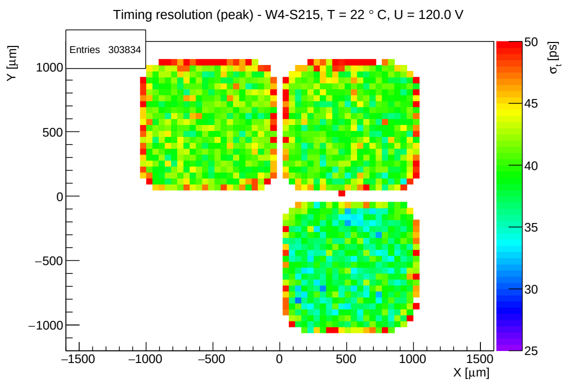

(f) Timing resolution - peak location method.

Figure D.16: Track-based plots for W4-S215 at $T = 22\,°\mathrm{C}$. The upper-right pad is selected to show the results. The lower-left pad is connected to a different oscilloscope than the SiPM.

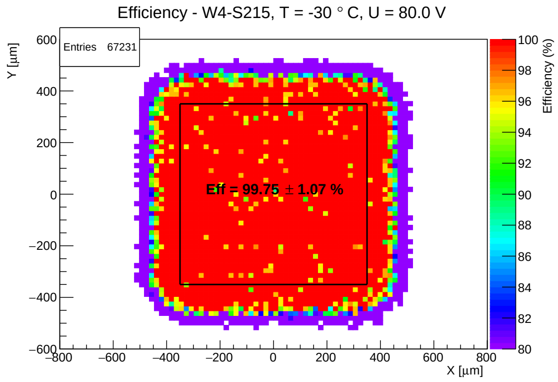

(a) Efficiency.

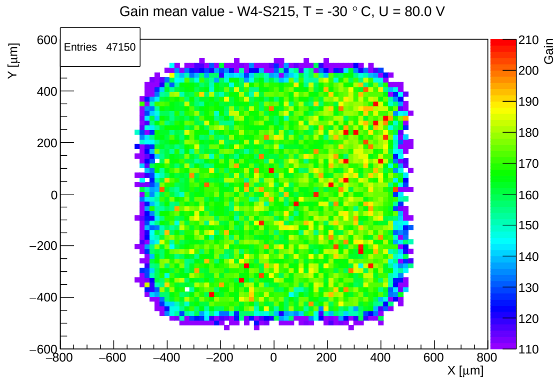

(b) Gain.

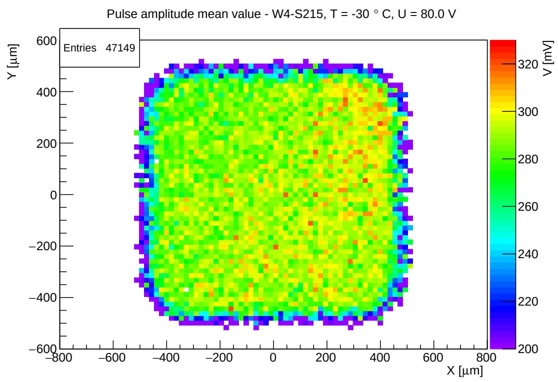

(c) Pulse amplitude.

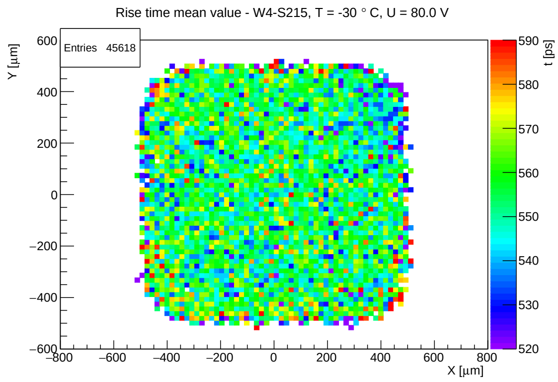

(d) Rise time.

Figure D.17: Track-based plots for W4-S215 at $T = -30\,°C$. This figure shows the upper-right pad in Figure D.16.

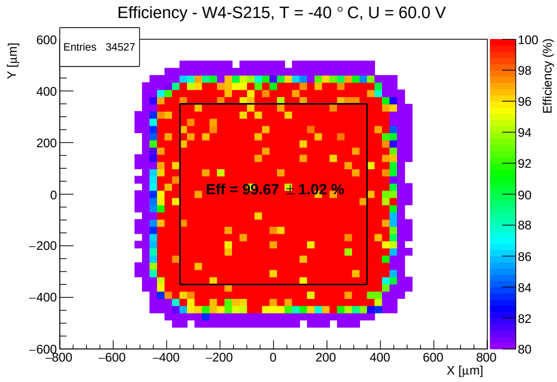

(a) Efficiency.

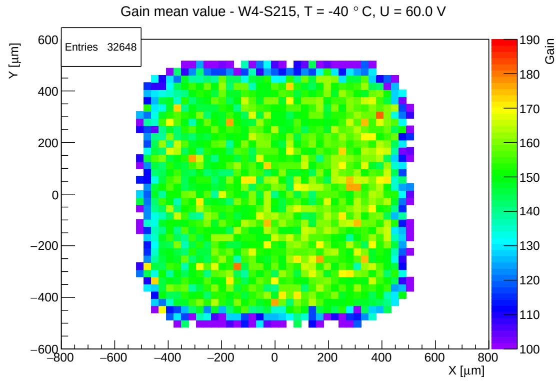

(b) Gain.

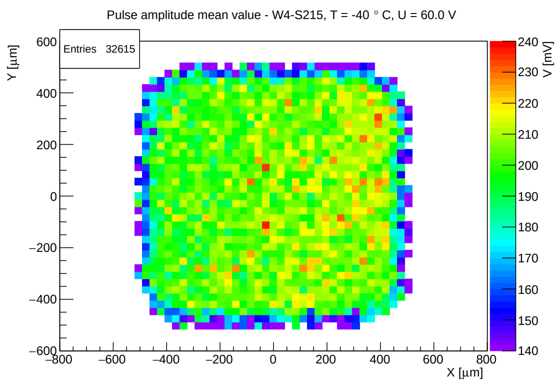

(c) Pulse amplitude.

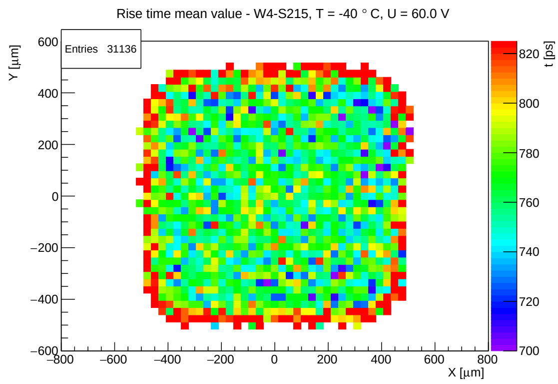

(d) Rise time.

Figure D.18: Track-based plots for W4-S215 at $T = -40\,°C$. This figure shows the upper-right pad in Figure D.16. The bin size is increased with 50% due to lower data statistics.

D.9 W9-LGA35

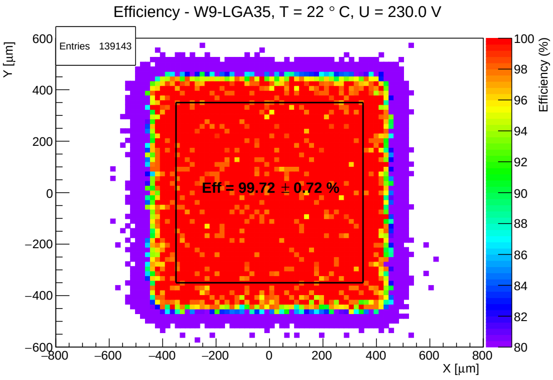

(a) Efficiency.

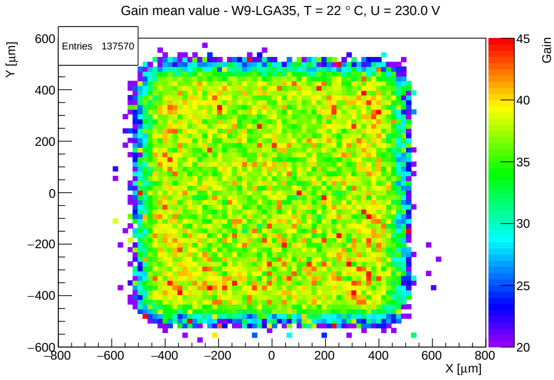

(b) Gain.

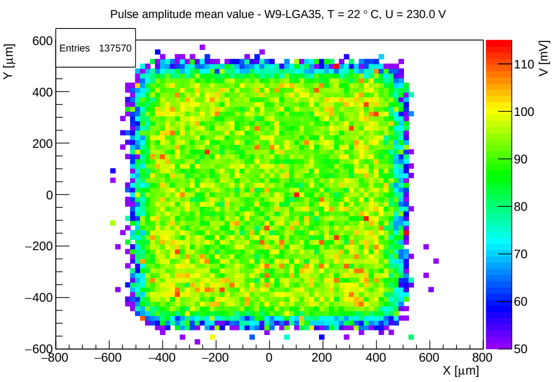

(c) Pulse amplitude.

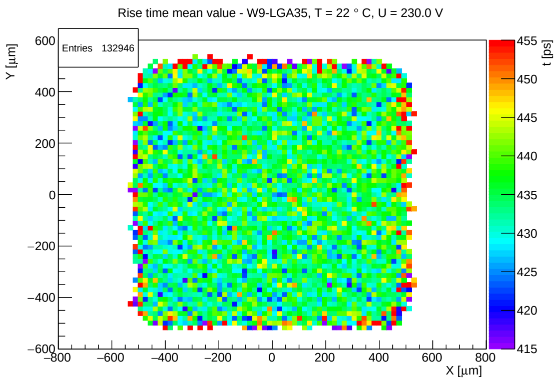

(d) Rise time.

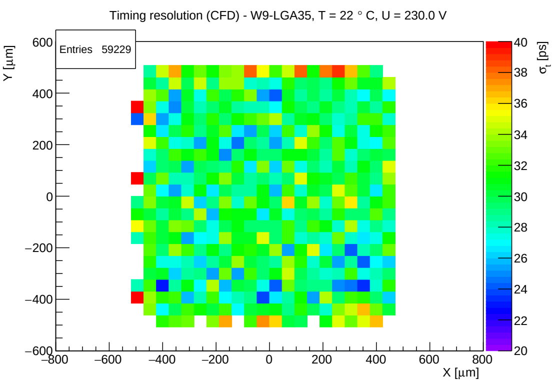

(e) Timing resolution - CFD method.

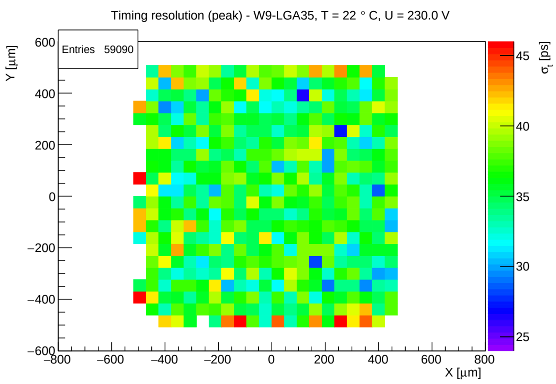

(f) Timing resolution - peak location method.

Figure D.19: Track-based plots for W9-LGA35 at $T = 22\,°\mathrm{C}$.

Bibliography

[1] P.A.R. Ade et al. Planck 2013 results. I. Overview of products and scientific results. *Astronomy and Astrophysics*, 571, 2014.

[2] G. Aad et al. The ATLAS Experiment at the CERN Large Hadron Collider. *JINST*, 3:S08003, 2008.

[3] ATLAS Collaboration. Technical Proposal: A High-Granularity Timing Detector for the ATLAS Phase-II Upgrade. Technical Report CERN-LHCC-2018-023. LHCC-P-012, CERN, Geneva, Jun 2018.

[4] HL-LHC High Luminosity Large Hadron Collider: The HL-LHC project. `http://hilumilhc.web.cern.ch/about/hl-lhc-project`. Accessed: 2018-08-30.

[5] L. Evans and P. Bryant. LHC Machine. *Journal Of Instrumentation*, 3(8), August 2008.

[6] K. Aamodt et al. The ALICE Experiment at the CERN LHC. *Journal of Instrumentation*, 3(08):S08002, 2008.

[7] S. Chatrchyan et al. The CMS Experiment at the CERN LHC. *Journal of Instrumentation*, 3(08):S08004, 2008.

[8] A. Augusto Alves Jr et al. The LHCb Detector at the LHC. *Journal of Instrumentation*, 3(08):S08005, 2008.

[9] Public ATLAS Run 1 Luminosity Information. `https://twiki.cern.ch/twiki/bin/view/AtlasPublic/LuminosityPublicResults`. Accessed: 2018-08-06.

[10] Public ATLAS Run 2 Luminosity Information. `https://twiki.cern.ch/twiki/bin/view/AtlasPublic/LuminosityPublicResultsRun2`. Accessed: 2018-12-03.

[11] CMS Luminosity - Public Results. `https://twiki.cern.ch/twiki/bin/view/AtlasPublic/LuminosityPublicResultsRun2`. Accessed: 2018-12-03.

[12] J. Pequenão. Event Cross Section in a computer generated image of the ATLAS detector. `http://cds.cern.ch/record/1096081`, Mar 2008.

[13] K. Potamianos. The upgraded Pixel detector and the commissioning of the Inner Detector tracking of the ATLAS experiment for Run-2 at the Large Hadron Collider. *PoS*, EPS-HEP2015:261, 2015.

[14] RD50 Collaboration. `https://rd50.web.cern.ch/rd50`.

[15] P. Fernández-Martínez et al. Low Gain Avalanche Detectors for high energy physics. In *2015 10th Spanish Conference on Electron Devices (CDE)*, pages 1–4, Feb 2015.

[16] G. Pellegrini et al. Technology developments and first measurements of Low Gain Avalanche Detectors (LGAD) for high energy physics applications. *Nuclear Instruments and Methods in Physics Research Section A: Accelerators, Spectrometers, Detectors and Associated Equipment*, 765:12 – 16, 2014. HSTD-9 2013 - Proceedings of the 9th International 'Hiroshima' Symposium on Development and Application of Semiconductor Tracking Detectors.

[17] L. Rossi and O. Brüning. High Luminosity Large Hadron Collider: A description for the European Strategy Preparatory Group. Technical Report CERN-ATS-2012-236, CERN, Geneva, Aug 2012.

[18] H. Jansen et al. Performance of the EUDET-type beam telescopes. *EPJ Techniques and Instrumentation*, 3(1):7, Oct 2016.

[19] C. Allaire et al. Beam test measurements of Low Gain Avalanche Detector single pads and arrays for the ATLAS High Granularity Timing Detector. *Journal of Instrumentation*, 13(06):P06017, 2018.

[20] HPK Run ECX840 Sensor information. `https://twiki.cern.ch/twiki/bin/view/Main/HPKRunECX840#Single_pad_Tested_LGAD_Diodes`. Accessed: 2018-10-08.

[21] H. Sadrozinski. HGTD Beam test September 2017. `https://indico.cern.ch/event/661235/contributions/2699651/attachments/1511773/2357803/Beam_Test-MC-HFWS_08_23_2017.pdf`. Internal presentation, only accessible to members of ATLAS collaboration.

[22] G. Pellegrini et al. Status of LGAD production at CNM. 30th RD50 Workshop, Kraków, 2017.

[23] F. Backman. Analysis of Test Beam Data for Sensors in the High Granularity Timing Detector, 2017.

[24] E.L. Gkougkousis. Timing performance and gain analysis of heavily irradiated LGAD diodes. 30th RD50 Workshop, Kraków, 2017.

TRITA SCI-GRU 2018:413